

AD-A129 130

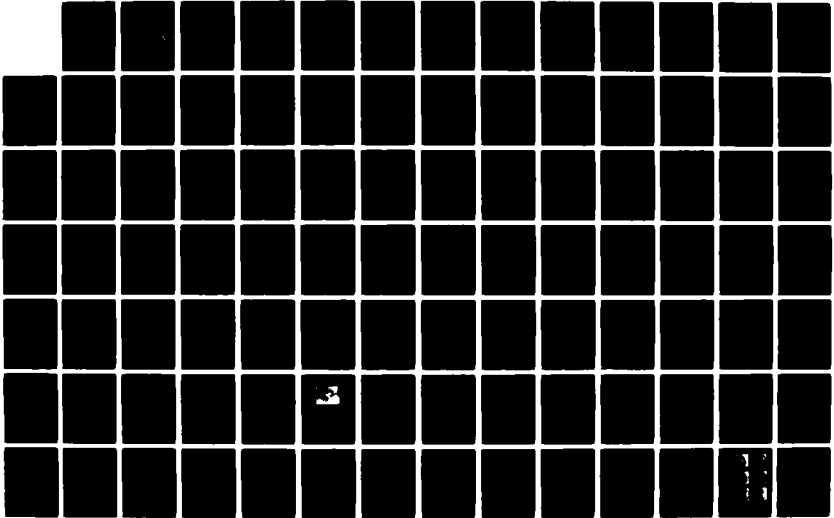
EFFECTS OF FLOW AND NON-NEWTONIAN FLUIDS ON
NONSPHERICAL CAVITATION BUBBLES(U) PRINCETON UNIV NJ
DEPT OF CHEMICAL ENGINEERING W R SCHOWALTER ET AL.
10 APR 83 N00014-79-C-0385

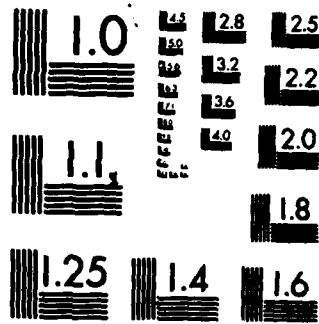
1/2

UNCLASSIFIED

F/G 20/4

NL





MICROCOPY RESOLUTION TEST CHART
NATIONAL BUREAU OF STANDARDS-1963-A

12

SECURITY CLASSIFICATION OF THIS PAGE (When Data Entered)

REPORT DOCUMENTATION PAGE		READ INSTRUCTIONS BEFORE COMPLETING FORM
1. REPORT NUMBER 160-6076-2	2. GOVT ACCESSION NO. AD-A129130	3. RECIPIENT'S CATALOG NUMBER
4. TITLE (and Subtitle) Effects of Flow and Non-Newtonian Fluids on Nonspherical Cavitation Bubbles		5. TYPE OF REPORT & PERIOD COVERED
7. AUTHOR(s) William R. Schowalter and Stuart K. Hara		6. PERFORMING ORG. REPORT NUMBER
9. PERFORMING ORGANIZATION NAME AND ADDRESS Department of Chemical Engineering Princeton University Princeton, NJ 08544		8. CONTRACT OR GRANT NUMBER(s) N00014-79-C-0385
1. CONTROLLING OFFICE NAME AND ADDRESS Office of Naval Research (Code 438) 800 N. Quincy St. Arlington, VA 22217		10. PROGRAM ELEMENT, PROJECT, TASK AREA & WORK UNIT NUMBERS NR 062-637
4. MONITORING AGENCY NAME & ADDRESS (if different from Controlling Office)		12. REPORT DATE 10 April 1983
		13. NUMBER OF PAGES 176 + x
		15. SECURITY CLASS. (of this report) Unclassified
		15a. DECLASSIFICATION/DOWNGRADING SCHEDULE
16. DISTRIBUTION STATEMENT (of this Report) Approved for public release; distribution unlimited.		
17. DISTRIBUTION STATEMENT (of the abstract entered in Block 20, if different from Report)		
18. SUPPLEMENTARY NOTES This is, in essence, the doctoral dissertation of S. K. Hara.		
19. KEY WORDS (Continue on reverse side if necessary and identify by block number) cavitation bubbles rheology viscoelastic liquids non-Newtonian fluid mechanics polymers		
20. ABSTRACT (Continue on reverse side if necessary and identify by block number) Flow cavitation is substantially altered, both at inception and during subsequent dynamics, by the addition of small amounts of water-soluble polymer. Theoretical and experimental single-bubble systems developed here trace the shape of a bubble as it is influenced by a volume change of the cavity, the rheology of the surrounding fluid, the presence of a solid wall, and/or an imposed external flow. (more)		

DTIC ELECTED JUN 10 1983 A

AD A 1 2 9 1 3 0

DTIC FILE COPY

DD FORM 1 JAN 73 1473

EDITION OF 1 NOV 66 IS OBSOLETE S/N 0102-LP-014-6601

SECURITY CLASSIFICATION OF THIS PAGE (When Data Entered)

83 06 10 045

TABLE OF CONTENTS

	<u>Page</u>
LIST OF FIGURES & TABLES	iii
NOMENCLATURE	v
 CHAPTERS	
I. INTRODUCTION	1
II. BACKGROUND	5
III. THE EQUATIONS OF MOTION	19
1. Spherical Dynamics	19
2. Viscous Nonsphericities	24
3. Viscoelastic Nonsphericities	31
IV. INITIATION AND FAR-FIELD CONDITIONS	40
V. EXPERIMENTAL PROGRAM	58
1. Introduction	58
2. Apparatus	60
3. Types of Trials	67
4. Fluids	68
5. Photo Analysis	69
VI. RESULTS	70
1. Theoretical Spherical Profiles	70
2. Model Nonspherical Dynamics without External Flow ..	74
3. Experiments with No External Flow	77
A. Spherical Bubbles	82
B. Spherical Bubbles near Solid Walls	85
C. Nonspherical Bubbles	85
D. Nonspherical Bubbles near Solid Walls	95
4. Model with External Flow	99
VII. CONCLUSIONS AND DISCUSSION	107

	<u>Page</u>
CHAPTERS	
VIII. THE NEXT STEPS	109
IX. BIBLIOGRAPHY	112
APPENDICES	
A. $O(\epsilon)$ Equations	A-1
1. Toroidal Field Equations	A-1
2. Amplitude Equations	A-11
3. Viscous Limit	A-23
B. $O(\epsilon^2)$ Terms	B-1
1. Introduction	B-1
2. Convection and Inertia	B-2
3. Non-Newtonian Nonlinearities	B-10
4. Amplitude Equations	B-17
C. Method of Solution	C-1
1. Programming Considerations	C-1
2. Sample Calculation	C-6
D. Data Analysis	D-1
1. Shape and Size Fit	D-1
2. Radius Profile	D-6
E. Additional Data for Photo Sequences	E-1

LIST OF FIGURES AND TABLES

<u>Figure Number</u>	<u>Title</u>	<u>Page</u>
1	Cavitation Inception Parameter Changes due to Polymer Solutes.	6
2	Thermal Effects on Spherical Bubble Growth.	10
3	Thermal Effects on Collapse.	10
4	Comparison of Experimentally Determined Bubble Shapes on Collapse with Theoretical Curves.	15
5	Bubble Surface Shapes on Collapse.	15
6	External Flows, y_1^∞ , for $Y_2^m(\theta, \phi)$.	50
7	Shapes Created by External Flows.	52
8	Representative Bubble Shape and External Flow for $Y_2^1(\theta, \phi)$.	53
9	Shapes for $r = R + \epsilon a_2 Y_2^0(\theta, \phi)$.	54
10	Alteration of Streamlines by Sphere for $Y_2^0(\theta, \phi)$.	55
11	Major Components of Optical Cavitation.	61
12	Arrangement of Apparatus.	62
13	Laser Focussing Parameters.	66
14	Spherical Radius vs. Time-Theoretical Growth.	72
15	Spherical Radius vs. Time-Theoretical Collapse.	73
16	Nonspherical Amplitude vs. Time-Viscosity.	75
17	Nonspherical Amplitude vs. Time-Viscoelasticity.	76
18	Normalized Amplitude vs. Time-Growth.	78
19,20	Nonspherical Amplitude vs. Time-Collapse I, II.	79,80
21	Bubble Sequence in Water.	83
22	Experimental Spherical Radius vs. Time Data.	84
23	Initially Spherical Bubble Collapsing Near a Solid Wall.	86

<u>Figure Number</u>	<u>Title</u>	<u>Page</u>
24,25	Comparison of Experimentally Determined Nonspherical	88,89
26,27	Amplitudes to Theoretically Generated Curves I, II, III, IV.	90,91
28	Nonspherical Sequence in Water.	94
29	Bubble-Wall Orientation.	97
30	Sequence - $B \perp N$.	97
31	Sequence - B and N at 45° .	98
32	Comparison of Flow and No Flow Condition.	100
33	Effect of External Flow Frequency.	104
34,35	External Flow, Flow Decay and Collapse I, II.	105,106

<u>Table Number</u>		
1	Features of Present Study.	3
2	Order of Magnitude of Terms in Radius Equation.	16
3	Parameter Values for Initial Calculations.	23
4	Equipment Specifications.	64
5	Dimensionless Parameters.	70
6	Dimensionless Groups for External Flow.	102
D1	Results of Fitting Procedures.	D-5

NOMENCLATURE

<u>Symbol</u>	<u>Definition</u>	
.	total first derivative wrt time	
..	total second derivative wrt time	
d/dx	total derivative wrt x	
$\partial/\partial x$	partial derivative wrt x	
D/Dt	convected derivative wrt time	III.14
$\frac{D}{Dt}$	Jaumann derivative wrt time	B
Re(z)	real part of complex number z	III.13
Im(z)	imaginary part of complex number z	
$\alpha_n = \alpha_n(t)$	1. scaled amplitude 2. integral function of toroidal field	II.6 III.29
β	reciprocal fluid relaxation time	IV.29
γ	polytropic gas constant	II.5
$\dot{\gamma}$	strain rate tensor	III.36
$\delta(x)$	Dirac delta function	III.9
$\Delta(x)$	change in x	III.2
ϵ	"small" expansion parameter	III.12
$\tau_{n,j} = \tau_j$	external flow time constant ($t < 0$)	IV.18
θ	spherical coordinate cone angle	
θ_f	laser focal angle	Figure 13
$\theta_j = \theta_{n,j}(t)$	time dependent external flow function	IV.13
λ	fluid relaxation time	III.9
μ	viscosity	Table 2
ν	kinematic viscosity	III.22
π	dimensionless ambient pressure change	Table 5

<u>Symbol</u>	<u>Definition</u>	
ρ	density	II.1
ρ^2	sum of square residues	D
$\rho_j = \rho_{n,j}(r)$	r-dependent external flow function	IV.13
$\rho_e^v(T)$	temperature-dependent equilibrium	II.2
σ	surface tension	II.3
σ_1	cavitation inception parameter	II.1
\underline{g}	total stress tensor	III.14
$\int (r, \theta, \phi, t)$	surface function	III.12
\sum_n	summation symbol	
τ	Lagrangian time coordinate	III.38
τ_0	time scale of oscillations	VI.1
τ_{flow}	dimensionless external flow frequency	Table 6
τ_{decay}	dimensionless external flow decay ($\tau > 0$)	Table 6
$\tau_{f.t.} =$ $\tau_{flow\ transient}$	dimensionless flow time scale ($\tau < 0$)	Table 6
$\underline{\tau}$	extra stress tensor	III.2
ϕ	spherical coordinate polar angle	
$\phi_p = \phi_{p,n}(r, \theta, \phi, t)$	asymmetric flow potential	III.19
$\phi_n = \phi_n(r, \theta, \phi, t)$	continuity integral	III.29
$\chi_j = \chi_{n,j}$	external flow toroidal field constant	IV.13
$\psi_j = \psi_{n,j}(t)$	external flow function	IV.27
$\omega = \omega_j = \omega_{n,j}$	external flow frequency	IV.18
$\underline{\omega}$	vorticity vector	III.21
$a = a_n = a_n(t)$	amplitude of n^{th} harmonic ($n=2$)	II.5 III.12
$\Lambda = \Lambda_n = \Lambda_{n,j}$	complex external flow number	III.41
$\Lambda(t) = \Lambda_n(t) = \Lambda_{n,j}(t)$	complex external flow function	II.23

<u>Symbol</u>	<u>Definition</u>	
$B = B_n = B_n(r, t)$	continuity function	A.2
\underline{b}	bubble axis vector	
C	heat capacity	II.2
C_j	fit parameter	D
$C_n = C_n(r, t)$	potential field factor	A.4
D	diffusion coefficient	II.2
$D_j = D_{n,j}$	external flow variable	IV.22
D_{beam}	effective laser beam diameter	V.1
De	Deborah number	Table 5
$e, e_e, e_v, e_{\text{max}}$	strain rates	IV.8-9
$\underline{e}_r, \underline{e}_\theta, \underline{e}_\phi$	unit vectors	III.29
$\underline{\underline{e}}$	strain rate tensor	III.6
El	elastic number	Table 5
f_1, f_2	focal lengths	V.2
$f_j = f_{j,n}(H, \tau)$	stress integrands ($j = 1, 2, 3, 4$)	A.11
$f(R, H)$	"geometric" function	IV.8
$F_1(x) = F_2(x)$	modified Bessel functions	IV.20
G_0	elastic modulus	III.9
G(t)	stability function	II.6
H	Lagrangian spatial coordinate	III.38
H(x)	Heaviside step function	
$I_1 = I_2 = I_3$	invariants of strain tensor	III.5
$I_j = I_{j,n}(H, \tau)$	terms in T-equation ($j = 1, 2, 3$)	III.41
$K_{n,j} = K_j$	external flow constant of separation	IV.14
K_j	fit parameter	D

<u>Symbol</u>	<u>Definition</u>	
$l_0, l_v/2$	fit measurements	D
L	latent heat of vaporization	II.2
$L = L(H, \tau)$	Lagrangian spatial coordinate	III.41
L_f	focal length	Figure 13
LHS	left-hand side	A.5
n	integral superscript on spherical harmonics	III.12
Ma	Mach number	III.3
n	integral subscript denoting nonspherical mode	
\mathbf{n}	outward unit normal to bubble surface	A.25
$N' = N(t-t')$	relaxation modulus (memory function)	III.9
\mathbf{N}	normal vector to solid wall	
$P, (p)$	(super or subscript) potential contribution	
$P_a = P_a(t)$	ambient pressure	III.18
$P_0 = P_0(r, t)$	$O(\epsilon^0)$ pressure field	III.17
$P_p = P_p(r, \theta, \phi, t)$	potential flow pressure field at $O(\epsilon^1)$	III.17
$P_v = P_v(v, \theta, \phi, t)$	vorticity pressure field at $O(\epsilon^1)$	III.17
P_v	vapor pressure	II.3
P_a	ambient pressure	II.3
$P = P(r, \theta, \phi, t)$	total pressure field	III.17
P_s	static pressure	II.1
$P_a = P_a(t)$	ambient pressure	III.2
$P_g = P_g(t)$	internal gas pressure	III.4
$P_v = P_v(t)$	internal vapor pressure	II.1
$P_v = P_v(r, t)$	(r, t) dependence of vorticity pressure	III.44
P^*	pressure step change	Table 3
$P_n^{(m)}$	Legendre polynomial	III.15
P_l	liquid pressure at $r = R$	III.2

<u>Symbol</u>	<u>Definition</u>	
r	spherical coordinate radius	
$R = R(t)$	surface equivalent radius	II.2
Re	Reynolds number	Table 5
RHS	right-hand side	
S	dummy spatial variable	III.30
$S = S_n = S_n(r, t)$	poloidal scalar function	III.24
$\underline{S} = \underline{S}(r, \theta, \phi, t)$	poloidal vector field	III.23
t	Eulerian time coordinate	II.2
t_0	1. collapse time 2. initial time	II.4 D
t_p	time period	D
$T = T_n = T_n(r, t)$	scalar toroidal function	III.25
$\underline{T} = \underline{T}(r, \theta, \phi, t)$	toroidal vector field	III.23
$v, (v)$	(super or subscript) vorticity contribution	
\underline{v}_0	$O(\epsilon^0)$ velocity field	III.16
\underline{v}_1	$O(\epsilon^1)$ velocity field	
\underline{v}_p	$O(\epsilon^1)$ vorticity velocity field	III.16
\underline{v}_v	$O(\epsilon^1)$ vorticity velocity field	III.16
\underline{v}_1^∞	$O(\epsilon^1)$ external flow field	IV.24
V_0	free stream velocity	II.1
$V_0 = V_{0,n}$	dimensionless initial nonspherical velocity	Table 5
$\underline{V}_{\text{spherical}}$	symmetric velocity field	III.1
\underline{V}	total velocity field	III.14
$X_n = X_n(H, \tau)$	integral function of T_n	III.41

<u>Symbol</u>	<u>Definition</u>	
$y_C, y_B, y_C,$ y_D, y_{BT}, y_s	} external flow functions	IV.29
$Y_n^0(\theta)$ $Y = Y_n^m(\theta, \phi)$	} spherical harmonics	II.5 III.12
$Z_n = Z_n(H, \tau)$	integral function of T_n	IV.29

I. INTRODUCTION

Bubble dynamics is commonly regarded as a harmless diversion. It elicits images of soap bubbles floating on air currents and perhaps of bubble baths or the gaseous volumes which arise in carbonated beverages. However, bubbles have a myriad of beneficial practical applications as well as potentially catastrophic consequences in many processes involving liquid flow. Of particular relevance here is the flow cavitation which can occur in pumping or aquatic propulsion devices. Uncontrolled formation of voids under these circumstances can result in large drops in efficiency and can eventually cause structural damage to the apparatus. Research activity has been carried out in this area for most of this century. Great strides have been made in reducing cavitation damage, e.g. the design and use of super-cavitating propellers which induce void formation in a controlled and predictable manner, but understanding of these phenomena is far from complete.

A new complication was introduced by the relatively recent availability of synthetic high molecular weight polymer molecules and the subsequent investigation of their properties. The presence of "drag reducing" polymers as solutes at very low concentrations (~ 500 ppm levels) in aqueous liquids dramatically changes the initiation and subsequent behavior of cavitation in "water" tunnel flows past blunt bodies. Attempts to extract the essential features which determine "cavitation inhibition" to allow some predictive capability for bubble dynamics and to provide more fundamental knowledge about the behavior

of polymer solutions in nonviscometric flows have achieved only limited success. A new model and experimental program is offered here which includes elements present in actual flow cavitation, but have not received much previous attention. For the first time, dilute polymer solution non-Newtonian effects cause non-negligible changes in bubble dynamics which can, in turn, alter the gross behavior of the void.

The features considered explicitly in this study are presented in Table 1. Surface tension at the gas-liquid interface is retained, but heat and mass transfer effects are not explicitly included. Although incorporation of the influence of each of these factors is not original with this work, the analysis of the interaction between them is unique. The simplest case of interest involves the behavior of a nonspherical bubble in a fluid of infinite extent upon which no external flow is imposed. The results show that the oscillations in shape, which occur because of the presence of surface tension, are strongly coupled to the overall volume change of the bubble. A change in shape due to fluid rheology is predicted which is larger than any alteration of the overall bubble size due to the same differences in fluid properties. The addition of an externally imposed flow around the body, which is the only source of asymmetries in the system, couples with fluid rheology to create differences between model bubbles which are much larger than those changes without flow. The experimental investigation of the behavior of an initially *nonspherical* bubble near a solid wall suggests that the well-established solid wall effect -- the induction of a liquid jet during the collapse of an initially spherical bubble -- is reduced by the initial asymmetry.

TABLE 1
Features of Present Study

	Theory	Exp't
FLOW AND RHEOLOGY OF FLUID	X	
AND	X	
NONSPHERICAL BUBBLE OF CHANGING SIZE	X	X
AND	X	X
SOLID BOUNDARY	X	X

These results, in conjunction with one another, suggest a mechanism by which dilute solution rheology may strongly influence flow cavitation behavior. The shape and subsequent action upon collapse of a bubble subject to the velocity gradients encountered during flow cavitation are significantly changed by fluid rheology. This shape is also important to the interactions between the bubble and the solid boundaries which are present. Thus, flow and rheology can change gross bubble dynamics. This working hypothesis is consistent with all of the present work and also with the puzzling lack of data showing rheological effects in previous single bubble experiments and theories since they usually treated the factors individually.

In order to demonstrate the importance of flow, asymmetries, and rheology in bubble dynamics, the groundwork laid by past researchers is very useful. From that basis, the present model can be developed with special consideration of initiation, rheological models and the methods employed to solve the resulting equations. Then, the means by which experimental tests were conducted are described. Results are subsequently presented. Initially, they appear with some comment as to their individual meaning, then they are discussed from a broader perspective. The conclusions so drawn are complete in the context of the present work, but also provoke speculation and suggest future work. Appendices have been included to clarify theoretical, numerical and experimental details. As a result, little development of equations is presented in the primary text.

II. BACKGROUND

The addition of small quantities of macromolecules to water (e.g. 500 ppm polyacrylamide) affects relatively large changes in the formation and subsequent behavior of flow-induced cavitation bubbles. This phenomenon has been quantified through measurement of the cavitation inception parameter, σ_i , which represents the conditions at which cavitation initially occurs as

$$\sigma_i = \frac{P_s - P_v}{\frac{1}{2} \rho V_o^2} \quad (1)$$

where P_s is the static fluid pressure, P_v is the vapor pressure, ρ is the density and V_o is the free stream velocity. Figure 1 shows typical "cavitation inhibition" data for water tunnel flow past a blunt body. The cavitation parameter has been reduced by as much as 70% for polymers such as guar gum (Ellis and Hoyt, 1968, Ellis and Ting, 1974, Oba, *et. al.*, 1978, Hoyt, 1976). Thus, higher velocities or "more severe" conditions are necessary to form voids. Other experiments show that differences persist even after inception.

In water, the appearance of the cavitation bubbles is very violent and chaotic, consisting of many very small bubbles... However, as the polymer is added, the cavity looks more transparent, and shows a regular, smooth, wavy pattern at the vapor-liquid interface. (Ting, 1978)

Gross differences appear in both the nucleation and subsequent behavior of cavitation bubbles. In this work, attention is focussed on the latter stage, where continuum descriptions are applied.

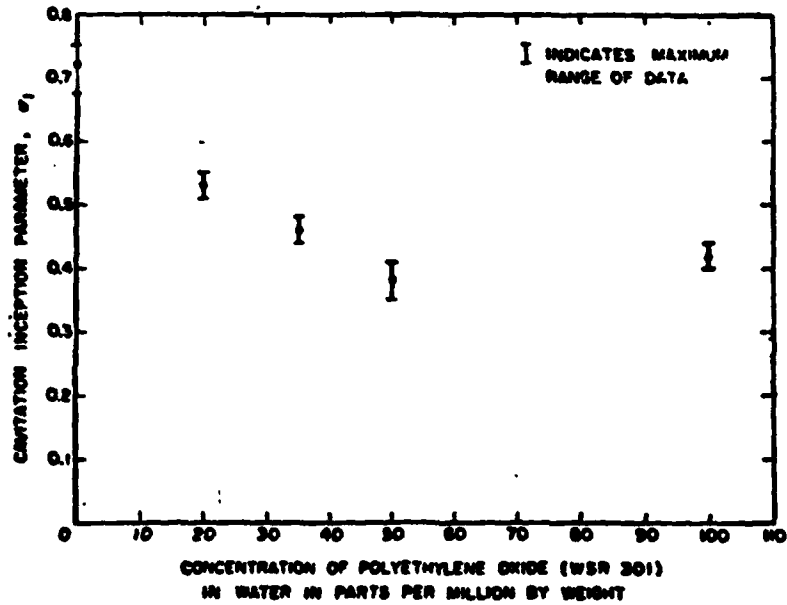
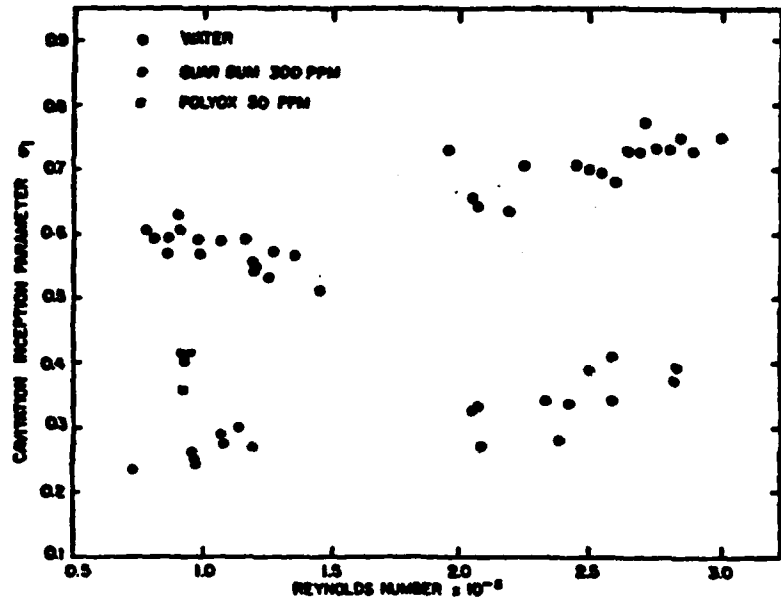


Figure 1. Cavitation Inception Parameter Changes due to Polymer Solute (ellis, et. al., 1970)

Many excellent sources of general information on bubbles are available including volumes by Hammit and his co-workers (1980, Knapp, *et. al.*, 1970), as well as review articles by Plesset and Prosperetti (1977), Acosta and Parkin (1975), Plesset alone (1977), and Prosperetti alone (1981). All theoretical work is seen to begin with Lord Rayleigh in 1917. He began by assuming a spherical void to be present in an infinite medium and neglecting all fluid properties except a constant density. A large amount of the bubble literature since that time has been devoted to the analysis of more detailed descriptions of fluid behavior, including viscosity and surface tension and other physical processes, e.g. heat and mass transfer, compressibility and the transport of contaminants. A form of these results is employed in the present work (Equation III.2) and like most treatments neglects processes within the bubble. By retaining an assumption of spherical symmetry, only one spatial coordinate, the radius r in spherical coordinates, has bearing on these analyses, greatly simplifying the equations of motion.

Results for spherical bubbles are divided into categories. For pure water, surface tension σ and viscosity μ are weak functions of other physical parameters such as temperature. This has allowed successful modelling under the assumption of constant values for those two coefficients. However, the composition and behavior of the pressure in the interior of the bubble with the evolution of the bubble is not so simple. Plesset (1977) has delineated two categories of bubble dynamics which he has labelled *gas* bubbles and *vapor* bubbles. Gas bubbles are those cavities for which the medium in the interior is largely or completely a permanent, noncondensable gas. For vapor bubbles the gaseous

phase consists almost entirely of the vapor of the surrounding fluid.

Gas bubbles have been extensively investigated, particularly in the areas of surface oscillations and mass diffusion effects. However, for the field of cavitation they are not relevant.

The category of vapor bubbles is subdivided into two other topics based upon the extent to which thermal effects alter the internal pressure, p_i , and thus, bubble behavior. The strong pressure dependences of equilibrium bubble pressure and vapor density act to significantly reduce p_i for a growing bubble as evaporation at the bubble surface cools the interior. Using an energy balance, and assuming that heat is supplied by a liquid layer which has thickness comparable to the diffusion length $(Dt)^{1/2}$, the "thin thermal boundary layer" assumption, this temperature difference can be estimated as

$$\Delta T = \frac{R \rho_v^e(T) L}{3(Dt)^{1/2} \rho c} \quad (2)$$

where L is the latent heat of vaporization, $\rho_v^e(T)$ is the equilibrium vapor density at temperature T , D is the thermal diffusivity, c is the heat capacity and t is the time required to grow to radius R . For water at 15°C , with $R = 0.1$ cm and $t = 10^{-3}$ sec, $\Delta T = 0.2^\circ\text{C}$, while at 100°C , $\Delta T = 13^\circ\text{C}$. For the former case, in which the thermal effect is not expected to be important, the proper term is *cavitation* bubble. In the latter, and all cases where thermal effects dominate inertial effects, the result is *boiling* or *vapor* bubbles.

The cavitation bubble is more relevant to this work and fortunately, is the simpler case. For constant p_i , and neglecting viscous effects

$$\dot{R}^2 = \left(\frac{R_0}{R}\right)^3 \dot{R}_0^2 + \frac{2}{3} \frac{p_v - p_\infty}{\rho} \left[1 - \left(\frac{R_0}{R}\right)^3\right] - \frac{2\sigma}{\rho R} \left[1 - \left(\frac{R_0}{R}\right)^2\right] \quad (3)$$

where $p_v = p_1$ is the vapor pressure, p_∞ is ambient pressure and initial values are denoted by the subscript zero. For $\dot{R}_0 = 0$ and neglecting the surface tension term, the Rayleigh result for time to complete collapse is

$$t_0 = \frac{\Gamma \left(\frac{5}{6}\right)}{\Gamma \left(\frac{1}{3}\right)} \left[\frac{3\pi\rho}{2(p_v - p_\infty)} \right]^{\frac{1}{2}} R_0 = 0.915 \left(\frac{\rho}{p_v - p_\infty} \right)^{\frac{1}{2}} R_0 \quad (4)$$

Quantitative experimental confirmation of this value was given by Lauterborn (1972). He was able to generate "empty" cavities by focusing a pulse from a Q-switched ruby laser on a point on the interior of a liquid mass. Agreement between experiment and equation (4) was excellent, despite the compressibility of the real liquid. Note that this compressibility is expected to become significant in the final stages of collapse, when the Mach number of the bubble becomes large.

The large magnitude of the thermal effect on boiling bubbles is illustrated in Figure 2. Here the theoretically predicted radius vs. time profiles for the Plesset analysis is shown along with the Rayleigh result for water at 103°C. Excellent experimental agreement with the Plesset prediction was found by Dergarebedian (1953). He observed

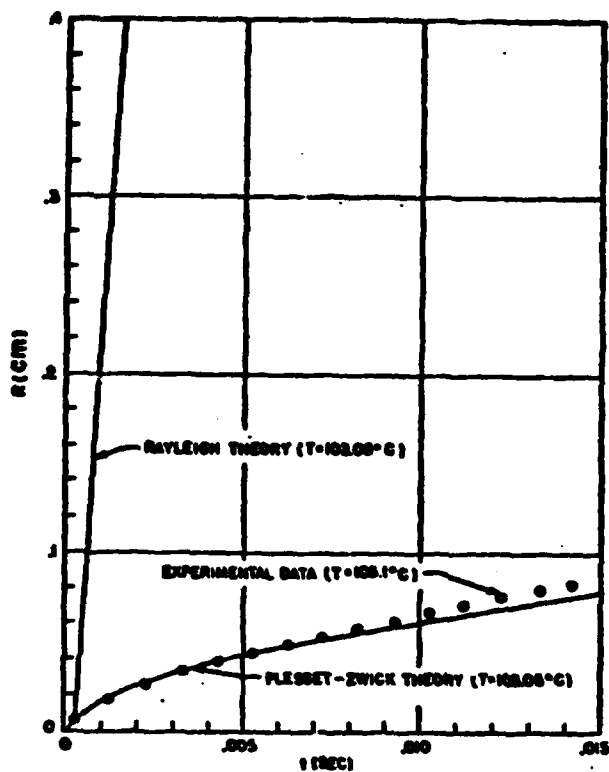
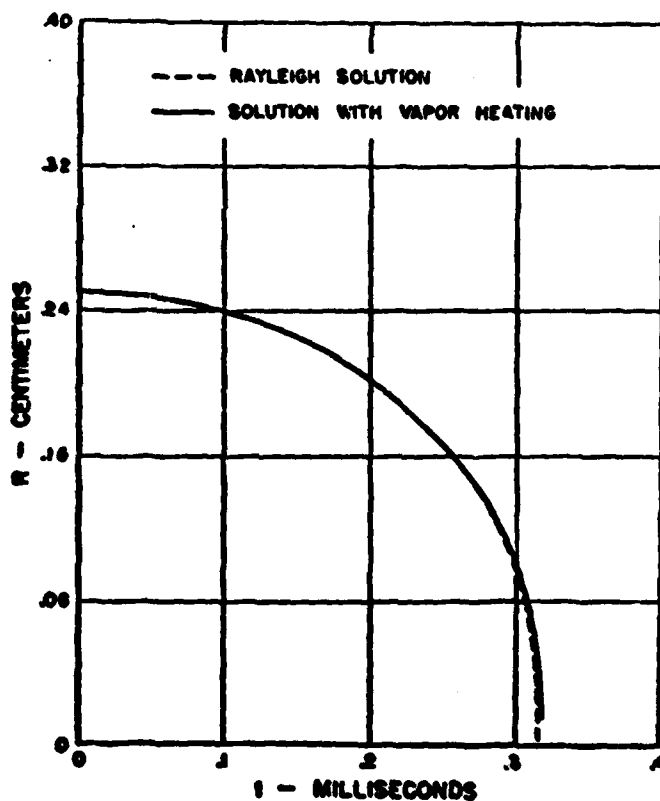


Figure 2.
Thermal Effects
on Spherical Bubble
Growth
(Dergarabedian, 1953,
Plesset & Zwick,
1954)

Figure 3.
Thermal Effects on
Collapse
(Zwick & Plesset,
1955)



spontaneous nucleation in superheated water.

Zwick and Plesset (1955) have also analyzed the collapse of a bubble. The distinction between cavitation and boiling bubbles is unimportant here. Despite the heating which occurs with vapor condensation, Figure 3 shows little deviation from the Rayleigh result.

Flynn (1975, 1976) has developed a more complicated model including compressibility and motions within the cavity as well as heat conduction and viscosity. His results cannot be summarized easily, but result in predictions of numerous regimes of bubble dynamics which have yet to be experimentally verified.

The results most relevant to the present study suggest that the growth and collapse of a spherical cavity in water are usually dominated by inertia and/or surface tension, not by viscosity. The small amount of viscoelasticity expected for dilute polymer solutions falls in the same category as viscosity. Both viscosity and viscoelasticity become more important for small radial oscillations (Tanasawa and Yang, 1970, Zana and Leal, 1975, Yang and Yeh, 1983), but are still minor.

Experimental testing of these results has been conducted almost exclusively on aqueous systems. Spark gap and laser techniques have been used to concentrate the energy necessary for cavitation inception. In general, good agreement with theory has been found (see Figure 2). More detail can be found in the section entitled "Experimental Program".

These analyses have all been carried out under the assumption that spherical symmetry of the bubble is maintained. Plesset (1954) performed a linear stability analysis on the nearly spherical interface between two immiscible, incompressible, inviscid fluids. He assumed a

drop shape given by

$$r_{\text{surface}}(\theta, t) = R(t) + \sum_n a_n(t) Y_n(\theta) \quad (5)$$

where Y_n is a spherical harmonic of degree n (MacRobert, 1948; Hobson, 1955), and a_n is initially small compared to the equivalent radius $R(t)$. The analysis proceeded conventionally in order to determine the conditions for which $a_n(t)$ will grow, suggesting the shape is unstable, and those for which it will not, implying stability. The stability condition which results can be expressed in terms of the function $\alpha_n(t)$, defined by

$$a_n(t) = \left(\frac{R_0}{R}\right)^{3/2} \alpha_n(t) \quad (6)$$

which was shown to be governed by

$$\ddot{\alpha}_n R - G(t) \alpha_n = 0 \quad (7A)$$

where

$$G(t) = \frac{3}{2} \left(\frac{\dot{R}}{R}\right)^2 + \frac{\ddot{R}}{R} \left[\frac{3}{2} + \frac{n(n-1)\rho_2 - (n+1)(n+2)\rho_1}{n\rho_2 + (n+1)\rho_1} \right] \quad (7B)$$

$$- \frac{(n-1)n(n+1)(n+2)\sigma}{[n\rho_2 + (n+2)\rho_1]R^2}$$

and σ is the surface tension, and ρ_1 and ρ_2 are the fluid densities of the interior and exterior fluids, respectively. The details of the amplitude profile depend on the particular initiation, but a general statement can be made

$G(t) < 0$ promotes stability

$G(t) > 0$ allows instability

this means that surface tension always has a stabilizing effect, and from Equation (6), increasing R or bubble growth is seen to have a stabilizing effect, while bubble collapse promotes instability.

Plesset and Mitchell (1956) then performed a more involved analysis for a vapor cavity, neglecting the density of the vapor and the viscosity of the vapor and the liquid. Their results showed that an *expanding* vapor cavity is stable, i.e. if $|a_n(0)|/R_0 \ll 1$, then $|a_n(t)|/R(t) \ll 1$. For a *collapsing* cavity, distortion amplitudes remained small as long as $1.0 \geq R/R_0 \geq 0.2$, but as $R \rightarrow 0$, $a_n(t)$ increased in magnitude as $R^{-3/4}$. Thus, the spherical shape is unstable for the later stages of bubble collapse. These trends are valid even when a small viscous effect is included in the treatment (Prosperetti & Seminara, 1978). Viscosity does tend to damp the growth in amplitude of the higher order harmonics.

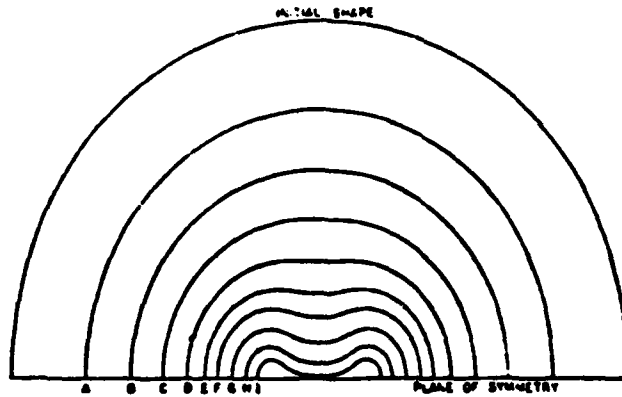
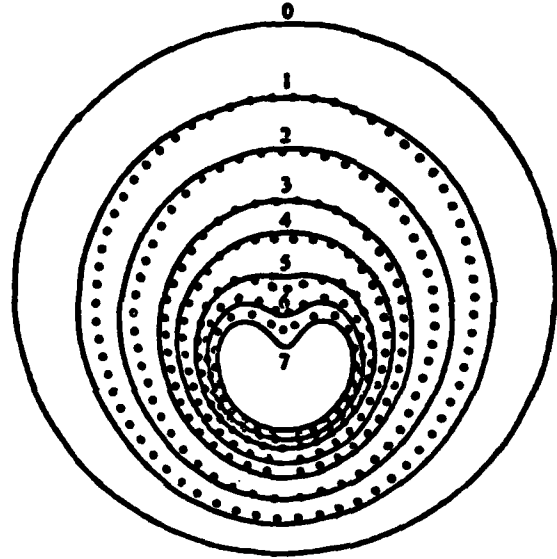
To determine the linear stability of the bubble shape only the long time behavior of the distortion is necessary. The bubbles were assumed to exist in an infinite fluid, quiescent apart from the effects of the dynamics of the cavity; this is a spherically symmetric geometry giving an equilibrium shape of similar character. Of course, this is not the only environment in which a bubble may arise. There may be conditions imposed on the fluid away from the bubble, such as an elongational flow or a solid boundary, or the bubble may be initialized as nonspherical and a detailed description of its evolution desired. Bubbles have provoked some study in this regard, but more

often liquid drops and solid bodies have been examined, giving rise to general techniques for nonspherical shapes.

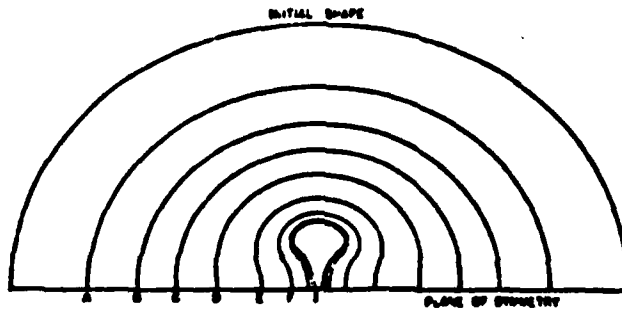
With bubbles and any other initially spherical bodies in an imposed flow, the primary method of study has been expansion of the velocity profile in terms of spherical harmonics (Cox, 1969, Shima & Nakajima, 1977). Use of this technique is usually predicated upon an assumption of creeping flow, at least in the immediate vicinity of the bubble. Under this restriction, Happel and Brenner (1965, section 3.2) offer a practical presentation of the use of spherical harmonics in Lamb's general solution (Lamb, 1945).

The presence of any interface in the vicinity of a bubble alters the flow induced by the cavity dynamics from a spherically symmetric velocity field. For a solid wall the collapse process results in a jet impinging on the wall which may be one of the major causes of the destructive action of cavitation. Experimentally the jet has been observed in laser-induced bubbles (Lauterborn & Bolle, 1975) in qualitative agreement with numerical simulations (Plesset & Chapman, 1971). (See Figure 4.) This type of behavior can be predicted using either integral methods, employing the Bernoulli equation while neglecting viscous stresses (Voinov & Voinov, 1975, 1976), or marker-and-cell simulations (Mitchell & Hammit, 1973), which can include viscosity. The viscous effects for water are negligible, dominated by surface tension and inertia. (See Table 2 for representative values.) The most important parameter appears to be the distance of the bubble from the wall.

Figure 4.
 Comparison of
 Experimentally
 Determined Bubble
 Shapes on Collapse
 with Theoretical
 Curves
 (Plesset &
 Chapman, 1971)



Bubble surfaces from case A



Bubble surfaces from case B

Figure 5.
 Bubble Surface
 Shapes on Collapse:
 initially
 nonspherical
 bubble
 (Chapman & Plesset)

TABLE 2

Order of Magnitude of Terms in Radius Equation

Inertial, Surface Tension and Viscous

$$R \sim 3 \times 10^{-1} \text{ cm}$$

$$\rho \sim 1 \text{ gm/cm}^3$$

$$\mu \sim 10^{-2} \text{ gm/(cm-sec)}$$

$$\sigma \sim 60 \text{ gm/sec}^2$$

$$\Delta t \sim 10^{-3} \text{ sec}$$

$$\Rightarrow \dot{R} \sim R/\Delta t \sim 3 \times 10^2 \text{ cm/sec}$$

$$\text{Inertial: } \rho \dot{R}^2 \sim 10^5$$

$$\text{Surface Tension: } \frac{2\sigma}{R} \sim 400$$

$$\text{Viscous: } \mu \frac{\dot{R}}{R} \sim 10$$

When the interface is not a solid wall, but is deformable like a free surface, an "entirely new form" (Gibson & Blake, 1981) of collapse can be observed experimentally. Depending on the physical properties of the boundary — 'inertia' and 'stiffness' — the bubble may migrate to or from the interface as the bubble collapses or pulsates. A jet forms and moves in the same direction as the overall migration.

An initial nonsphericity is important even in the absence of an imposed flow or solid boundary. The requisite mathematics has been put forth by Hsieh (1965, 1974), who includes equations for heat and mass transfer effects, compressibility and also variational methods. Simplified numerical results by other authors (Chapman & Plesset, 1971) show that an initially prolate spheroid (Figure 5A) may form two jets upon collapse, while an oblate spheroid (Figure 5B) leads to a dumbbell form. The most relevant feature of these nonlinear results is that the linear theory of Plesset and Mitchell (1956) agrees well until the final stages of collapse.

Very little has been offered here so far about non-Newtonian or viscoelastic effects, either generally or in relation to bubbles. In the general view it is best to refer to the numerous treatises on the subject (Bird, Armstrong & Hassager, 1977, Schowalter, 1978). The most important general consideration is that fluids which exhibit viscoelastic effects may behave in a manner which runs counter to an observer's "Newtonian" intuition (Schowalter, 1978), e.g. the Weissenberg rod-climbing effect. Furthermore, the history or pre-treatment of such a material can be vitally important to its performance. In modelling there are innumerable complications which almost invariably force a

compromise between rigorously formulated constitutive equations of fluid behavior and simpler forms which result in tractable mathematics. The applicable models and quantitative results are also highly dependent on the particular flow present, although qualitative trends are usually similar. These difficulties must be considered in the quasi-linear model employed in the present work; careful attention is given to possible nonlinear effects. (See Appendix B)

Dilute solution non-Newtonian effects on bubbles brings attention back to cavitation inhibition. Spherical bubbles show little effect (Ting, 1975, 1977, Ting & Ellis, 1974), experimentally or theoretically. Experiments involving nonspherical bubbles, by Chahine (1981) and others (Chahine & Fruman, 1977, Gibson & Blake, 1981) with collapsing bubbles near interfaces, show a "significant" delay in the creation of the microjet when 250 ppm of polyox are added to the solution and the interface is solid. Observations near a free surface also show an effect from dilute additives. However, these results are not definitive and the relationship between them and cavitation effects is still a matter of speculation. Observations by different workers may even appear contradictory. Chahine suggests that the level of nonsphericity in bubbles is reduced upon addition of polymer solute, while Oba (1978) reports the opposite effect in his flow experiments.

III. THE EQUATIONS OF MOTION

1. Spherical Dynamics

For the cavitation model developed here the nonspherical shape will be coupled with the overall growth or collapse of the bubble. This volume change is treated through an analysis of the equivalent spherical bubble. Continuity requires that the velocity field in an incompressible fluid in this symmetrical situation have the form

$$[v_{\text{spherical}}(r,t)]_r = \frac{R^2(t) \dot{R}(t)}{r^2} \quad (1)$$

in spherical coordinates with origin at the bubble center. $R(t)$ and $\dot{R}(t)$ are the instantaneous radius and its time derivative, respectively. The fluid is assumed to be quiescent at infinity so the angular velocity components are identically zero.

The r-component equation of motion integrated from the surface $r = R$ to infinity then gives

$$\rho [R\ddot{R} + \frac{3}{2} \dot{R}^2] = P_l - P_a + \int_R^\infty (\underline{v} \cdot \underline{\tau})_r dr \quad (2)$$

where ρ , the liquid density, $\underline{\tau}$, the extra stress tensor, P_l , the liquid pressure at $r = R$, and P_a , the ambient pressure, must now be specified. By neglecting the viscosity and density of the internal gas the bubble is assumed to have a uniform internal pressure. This should be accurate as long as the ratio between internal and liquid viscosities is

small and the internal Mach number

$$Ma_{\text{internal}} \sim \dot{R}/(3 \times 10^4 \text{ cm/sec}) \ll 1 \quad (3)$$

since the speed of sound in air is approximately equal to this denominator. Surface tension can be included so that Equation (2) can be expressed as a normal force balance across the surface

$$\rho[R\ddot{R} + \frac{3}{2}\dot{R}^2] = P_g(t) + P_v(t) - P_a(t) - \frac{2\sigma}{R} + 3 \int_R^{\infty} \frac{\tau_{rr}}{r} dr \quad (4)$$

where P_g is the internal pressure of non-condensable gas, P_v is the vapor pressure of the liquid at the surface temperature and σ is surface tension. This form of the equation is sufficiently general to be capable of including:

A) The nature of the non-condensable gas

$$\text{e.g. } P_g(t) = P_g(R) = R_g^0 \left(\frac{R}{R_0}\right)^{3\gamma} \quad (5A)$$

for a polytropic gas

B) Thermal effects

$$P_v(t) = P_v(T), \quad \sigma(t) = \sigma(T) \quad (5B)$$

$$\text{and } \nu(t) = \nu(T)$$

C) Different constitutive stress expressions

$$\text{e.g. } \tau_{rr} = f(I_1, I_2, I_3) \text{ for} \quad (5C)$$

strain invariants I

The simplest, useful, non-zero, stress expression is that for a purely

Newtonian fluid with constant viscosity μ . For this velocity field the radial deformation rate is

$$e_{rr}(r,t) = \frac{2R^2(t) \dot{R}(t)}{r^3} \quad (6)$$

so that

$$\int_R^{\infty} \frac{\tau_{rr}}{r} dr = \frac{2}{3} \mu \frac{\dot{R}(t)}{R(t)} \quad (7)$$

Non-Newtonian expressions may be complicated by higher time derivatives or integration over past times combined with material objectivity constraints. When the time integration is performed in a Lagrangian frame, following each fluid element, objectivity is satisfied for this simple, symmetrical flow situation. The Lagrangian coordinates can easily be related to the Eulerian, laboratory-fixed, coordinates by

$$(r')^3 = r^3 + R^3(t') - R^3(t) \quad (8)$$

where r' denotes the position, at the past time t' , of a particle which, at present time t , resides at radius r . Time integration must be performed at constant r' .

A mathematically simple model which includes stress accumulation with fading memory was employed by Fogler and Goddard (1970, 1971), who specified a relaxation modulus (memory function) $N(t)$ such that

$$\tau_{rr}(t) = \int_{-\infty}^t N(t-t') e_{rr}(t') dt' \quad (9)$$

$$N(t) = \mu \delta(t) + G_0 \exp(-t/\lambda)$$

when $\delta(t)$ is the Dirac delta function. The elastic contribution is characterized by two parameters: λ , a relaxation time, and G_0 , an elastic modulus. In the limit of zero elasticity a Newtonian fluid with viscosity μ is described. In the Lagrangian frame, the stress term becomes

$$\int_R^{\infty} \frac{\tau_{rr}}{r} dr \quad (10)$$

$$= -4 \int_{-\infty}^t N(t-t') \frac{\dot{R}(t') R^2(t') \ln\left(\frac{R(t')}{R(t)}\right) dt'}{R^3(t') - R^3(t)}$$

A similar result obtains for an Oldroyd three-constant model. Ting (1977) shows that the equivalent elastic modulus is expected to be directly proportional to polymer concentration. To generate a radius profile initial conditions need to be specified. Ting chose to impose equilibrium before time $t = 0$, then postulated a step change in ambient pressure of magnitude P^* at time $t = 0$ to initiate motion. By his convention, when $P^* < 0$ the bubble grows. The numerical solution predicts changes in $R(t)$ values of less than 2% between pure water and a slightly viscoelastic medium.

Fogler and Goddard present large elastic effects, i.e. changes in the $R(t)$ profiles, but for parameter values which minimize surface

tension and correspond to G_0 much beyond the small values expected by Ting. Since the present work was motivated by dilute solution phenomena, values closer to Ting's were investigated. This meant little alteration of the steady shear viscosity was allowed. One manner by which to impose this requirement was to restrict the relative values of G_0 and λ by

$$G_0 \lambda = \mu$$

where

(11)

$$\mu \sim 0 \text{ (} 10^{-3} \text{ Pa-s)}$$

which gives an elastic contribution to the steady shear stress equal to the viscous component. In calculations the initial physical parameter values were chosen to correspond to superheated water at 103°C, since experimental data on spherical bubble dynamics were available (Dergarabedian, 1953).

TABLE 3

Parameter Values for Initial Calculations

$$P_v = 845 \text{ mm Hg}$$

$$P_a = 760 \text{ mm Hg}$$

$$\sigma = 58.9 \text{ dyne cm}$$

$$\rho = 0.961 \text{ gm/cm}^3$$

$$-10^5 \text{ dyne/cm}^2 \leq P^* \leq 10^5 \text{ dyne/cm}^2$$

$$10^{-5} \text{ sec} \leq \lambda \leq 1.0 \text{ sec}$$

For all P^* and λ values the radius profiles changed by about 1% or less between a purely viscous and viscoelastic fluid subject to condition (11). As the magnitude of P^* increased, inertia became more important since velocities and accelerations became larger. For more detailed results, see Section VI.

2. Viscous Nonsphericities

The relaxation of the assumption of spherical symmetry greatly complicates the analysis, even for the purely viscous case, since θ and ϕ components and dependencies now exist. A general analysis might begin with the full equations of motion in spherical coordinates. However, the Navier-Stokes equations include nonlinearities from the convected inertial terms. These introduce computational difficulties which are compounded for viscoelastic fluids by nonlinear co-deformational or co-rotational constitutive models.

Prosperetti (1977, 1980) neglected the non-linearities in the purely viscous case by imposing the condition that all departures from spherical symmetry be small. The shape of the bubble surface $\Sigma(r, \theta, \phi, t)$ can then be expanded in spherical harmonics.

$$\Sigma(r, \theta, \phi, t): \quad (12)$$

$$r - R(r) - \epsilon \sum_n a_n(t) Y_n^m(\theta, \phi) = 0$$

for some small parameter ϵ which must be determined to allow the desired mathematical, and physical, simplifications. Here, $a_n(t)$ is the

magnitude of the spherical harmonic $Y_n^m(\theta, \phi)$. The spherical harmonics determine a particular angular dependence and are defined as the solutions to

$$[n(n+1) + \frac{1}{\sin\theta} \frac{\partial}{\partial\theta} \sin\theta \frac{\partial}{\partial\theta} + \frac{1}{\sin^2\theta} \frac{\partial^2}{\partial\phi^2}] Y_n^m = 0$$

or, equivalently

$$Y_n^m(\theta, \phi) = e^{i|m|\phi} P_n^{|m|}(\cos\theta) \quad (13)$$

for the Legendre polynomials $P_n^{|m|}(x)$.

Of course, the full velocity field $\underline{v}(r, \theta, \phi, t)$ must satisfy:

$$\frac{D\underline{v}}{Dt} = \frac{\partial \underline{v}}{\partial t} + (\underline{v} \cdot \nabla) \underline{v} = \frac{1}{\rho} \text{div. } \underline{\sigma} \quad (14)$$

where the stress tensor $\underline{\sigma}$ for a Newtonian fluid in Cartesian coordinates is

$$\sigma_{ij} = -p \delta_{ij} + \mu \left(\frac{\partial v_i}{\partial x_j} + \frac{\partial v_j}{\partial x_i} \right) \quad (15)$$

The surface shape Σ , above, is consistent with a perturbation expansion of \underline{v} and the pressure field P as

$$\underline{v}(r, \theta, \phi, t) = \underline{v}_0 + \epsilon \underline{v}_p + \epsilon \underline{v}_v + O(\epsilon^2) \quad (16)$$

$$P(r, \theta, \phi, t) = p_0 + \epsilon p_p + \epsilon p_v + O(\epsilon^2) \quad (17)$$

when \underline{v}_0 and p_0 obtain for the unperturbed spherically symmetric case

previously presented.

$$p_0 = p_a(t) + \rho[(R^2\ddot{R} + 2R\dot{R}^2)/r - \frac{1}{2} \frac{\dot{R}^2 R^4}{r^5}] \quad (18)$$

The first order asymmetries can be divided into two parts; the first arises in an inviscid potential analysis. Plesset (1954) shows

$$\underline{v}_p = \underline{\nabla} \phi_p \quad (19)$$

$$\text{where } \phi_p = -\frac{1}{n+1} \frac{R^{n+2}}{r^{n+1}} [\dot{a}(t) + 2a(t) \frac{\dot{R}(t)}{R(t)}] Y_n^m(\theta, \phi)$$

and

$$p_p \Big|_{r=R} = \frac{\rho}{n+1} [R(t)\ddot{a}(t) + 3\dot{R}(t)\dot{a}(t) + 2\ddot{R}(t)a(t)] Y_n^m(\theta, \phi) \quad (20)$$

The second type of $O(\epsilon)$ term is necessitated by the introduction of viscous dissipation and/or elastic energy storage. Since potential functions such as the inviscid velocity profile have zero curl, this second velocity can be treated through the vorticity $\underline{\omega}$

$$\epsilon \underline{\omega} = \underline{\nabla} \times \underline{v} = \epsilon \underline{\nabla} \times \underline{v}_v \quad (21)$$

which is governed by the usual vorticity equation for the purely viscous case. At first order in ϵ

$$\frac{\partial \underline{\omega}}{\partial t} + \underline{\nabla} \times (\underline{\omega} \times \underline{v}_0) = -\nu \underline{\nabla} \times (\underline{\nabla} \times \underline{\omega}) \quad (22)$$

for kinematic viscosity ν .

The usefulness of this analysis in terms of vorticity is not only the elimination of the need to explicitly determine the pressure field, but also a decomposition of ψ is possible since it is solenoidal ($\nabla \cdot \psi = 0$). The vorticity can be expressed as the sum of two other vector fields, one poloidal and the other toroidal, which can, by definition, be expressed through two series of *scalar* functions.

$$\psi = \mathcal{S} + \mathcal{T} \quad (23)$$

$$\mathcal{S}(r, \theta, \phi, t) = \sum_n \sum_m \nabla_x \nabla_x [S_n(r, t) Y_n^m(\theta, \phi) \underline{e}_r] \quad (24)$$

$$\mathcal{T}(r, \theta, \phi, t) = \sum_n \sum_m \nabla_x [T_n(r, t) Y_n^m(\theta, \phi) \underline{e}_r] \quad (25)$$

Since these two vector fields are orthogonal, the linearized equation can now be written as two series of independent scalar equations. For each index n :

$$\frac{\partial \mathcal{S}}{\partial t} + \dot{R} \left(\frac{R}{r} \right) \frac{\partial \mathcal{S}}{\partial r} = \nu \left[\frac{\partial^2 \mathcal{S}}{\partial r^2} - n(n+1) \frac{\mathcal{S}}{r^2} \right] \quad (26)$$

$$\frac{\partial \mathcal{T}}{\partial t} + \frac{\partial}{\partial r} \left[\dot{R} \left(\frac{R}{r} \right)^2 \mathcal{T} \right] = \nu \left[\frac{\partial^2 \mathcal{T}}{\partial r^2} - n(n+1) \frac{\mathcal{T}}{r^2} \right] \quad (27)$$

The properties of poloidal and toroidal fields (Chandrasekhar, App. III) can next be employed to show that:

$$v_v = \sum_{n,m} \left\{ T_n(r,t) Y_n^m e_r + \nabla \times [S_n(r,t) Y_n^m e_r] - \nabla \phi_n \right\} \quad (28)$$

Continuity considerations require the presence of the final term which must satisfy

$$\nabla^2 \phi_n = \nabla \cdot T_n Y_n^m e_r \quad (29A)$$

Integrating this equation

$$\begin{aligned} \phi_n = Y_n^m \left\{ [\alpha_n(t) + \frac{n+1}{2n+1} \int_R^r S^{-n} T_n(S,t) dS] r^n \right. \\ \left. + \left[\frac{n}{n+1} R^{2n+1} \alpha_n(t) + \frac{n}{2n+1} \int_R^r S^{n+1} T_n(S,t) dS \right] r^{-(n+1)} \right\} \quad (29B) \end{aligned}$$

where the "constant" of integration $\alpha_n(t)$ is determined by the ambient flow conditions. When the flow decays at infinity,

$$\alpha_n(t) = - \frac{n+1}{2n+1} \int_R^\infty S^{-n} T_n(S,t) dS . \quad (30)$$

These defining equations for S and T and their relationship to the perturbation velocity v_v allows an *a posteriori* evaluation of ϵ . The simplification of these equations is only valid when the nonlinear terms, corresponding to convective terms in the substantial time derivative, which are $\theta(\epsilon^2)$, are much smaller than the $\theta(\epsilon)$ terms. These restrictions are considered in Appendix B.

Boundary conditions on ξ and Γ are now required to specify the solution (Cox, 1969, Scriven, 1960). For an inviscid and massless internal gas the velocity profile must satisfy the zero tangential stress condition and the balance of normal stresses at the interface. The former condition becomes:

$$\frac{\partial}{\partial x} \{r^{-2} [\mu S(r,t)]\}_{r=R} = 0 \quad (31)$$

$$\begin{aligned} 2(2n+1)R^{n-2} [-\mu \alpha(t)] + \frac{(n+1)}{R} [\mu T(R,t)] \\ = 2(n+2)\mu \frac{\dot{a}}{a} - (n-1)\mu a \frac{\dot{R}}{R^2} \end{aligned} \quad (32)$$

where the amplitude $a(t)$ and its first derivative enter the equation through considerations of surface curvature. The viscous contribution to pressure in the external fluid at $r = R$ is

$$P_v \Big|_{r=R} = n\rho Y_n^m \left\{ v \frac{T(R,t)}{R} + \left(\frac{\dot{R}}{R}\right) \int_R^\infty \left[\left(\frac{R}{S}\right)^3 - 1\right] \left(\frac{R}{S}\right)^n T(S,t) dS \right\} \quad (33)$$

and it can be used to express the normal stress boundary condition at $r = R$.

$$\begin{aligned} 0 = & \frac{1}{n+1} \ddot{a}(t) \\ & + \left[\frac{3}{n+1} \dot{R} - \frac{2}{R} (n+2)(n-1)v \right] \dot{a}(t) \\ & + \left[-\frac{n-1}{n+1} \ddot{R} + 2(n-1)(n+2)v \frac{\dot{R}}{R^2} + (n-1)(n+2) \frac{\sigma/\rho}{R^2} \right] a(t) \end{aligned}$$

$$+ n(n+2)v \frac{T(R,t)}{R} - n \left(\frac{\dot{R}}{R} \right) \int_R^\infty \left[1 - \left(\frac{R}{S} \right)^3 \right] \left(\frac{R}{S} \right)^n T(S,t) dS \quad (34)$$

Since the bubble shape determined by the $a_n(t)$ is of primary interest this last equation may be viewed as the principal expression of interest. It is an equation of motion for bubble shape, while the other two are boundary and consistency conditions.

Prosperetti solved only for the case of constant bubble radius. Since the coefficients of $a(t)$ and its derivatives are then constants and only the inhomogeneous, forcing function is time-dependent, solution of the system is considerably simplified. Laplace transform techniques can be applied to determine the asymptotic behavior of $a_n(t)$ analytically. However, to generate a complete $a_n(t)$ profile numerical techniques are necessary to invert the solution in the Laplace domain. Of course, initial conditions such as the initial amplitude $a_n(0)$ and non-spherical velocity $\dot{a}_n(0)$ are also necessary.

Results for this particular case, where there is no motion previous to time $t = 0$, show nonspherical amplitudes undergoing damped oscillations. Initially, the frequency is determined by surface tension and damping factor by viscosity, but no such simple statements can be made about the behavior at long times.

These Laplace techniques are not applicable when the equivalent radius R is not constant, but the results for this case will probably be more interesting in view of the stability analyses summarized in Section II and

"Indeed, it is expected that in a flow with so strongly converging (or diverging) streamlines as the spherical one the accompanying concentration (or dilatation) of vorticity would play an important role in the process of energy dissipation and hence in the equation of motion for $a(t)$ ". (Prosperetti, 1977, pp. 345,346)

Prosperetti (1980) has also approximated the solution of some cases of variable R by making a series of approximations. He concludes that small viscosity will not substantially inhibit the instability of the spherical shape for moderate n . However, it may change the mode of breakup if the bubble collapses into many fragments.

Before proceeding, the neglect of the poloidal field ξ should be justified. All equations governing this function (Equations 26 & 31) are homogeneous, so it is never present unless initiation requires its existence. Physically, a zero poloidal field corresponds to an absence of circulation or bulk rotation (Batchelor, 1970 p. 93) in the fluid. Mathematically, poloidal fields are necessary when the velocity contains components with angular dependences given by

$$\nabla \times [Y_n^m(\theta, \phi) \mathbf{e}_r].$$

3. Viscoelastic Nonsphericities

Extension of this perturbation technique to include viscoelasticity is straightforward in principle, however the level of complexity of the resulting equations is much higher and there are additional ramifications of the linearization. An integral model (Equations 9 & 11) of fluid behavior has been chosen in part because explicit expressions

for the stresses are then available. This introduces an integro-differential form to the system. Material objectivity requirements, e.g. co-deformational or co-rotational integrations, will, in general, introduce nonlinearities which must be evaluated (See Appendix B.2).

The extra stress expressions in the purely viscous, Newtonian, case have the relatively simple form of the terms in equations (27), (32) and (34) which include a viscosity constant μ or ν . Any further complications are removed by the instantaneous nature of the process of viscous dissipation and its characterization here by a single, time- and position-independent physical constant. Any spatial variation in the viscosity would disallow the amplifications which result from the manipulation

$$\nabla \cdot \mu [(\nabla \underline{v}) + (\nabla \underline{v})^T] = 2\mu \nabla^2 \underline{v} \quad (35)$$

and others like it. To include viscoelasticity, all these extra stress terms must be altered with careful consideration of the order of operation and reference frame or coordinate system in which they are performed.

The fundamental difference when viscoelastic stresses are calculated is the need to operate not merely on the instantaneous strain rate, but also on its appropriate time derivative in a differential model or on the pertinent past values for an integral equation. Following Fogler and Goddard, a Maxwell-type integral model is employed here since it is tenable with superposition of simple viscous and fading elastic effects and is the small-deformation limit of many other, more general expressions. Beginning with velocity field (28) and boundary

conditions (32) and (34), terms of the form

$$v \dot{\gamma} (R; r, t) \quad (36)$$

and replaced in the linear theory by

$$\int_{-\infty}^t N(t-t') \dot{\gamma} (R'; r', t') dt' \quad (37)$$

This is not a simple Eulerian integral over past times. Rigorous material objectivity constraints would require a Lagrangian frame with corotational or co-deformational contributions to take convective and orientational changes in inter-fluid element spatial configurations into account.

Radial convection is incorporated to $O(\epsilon^0)$ just as it was in the spherical case. A new radial position coordinate H is defined here which is equivalent to the Lagrangian coordinate (8) for symmetric dynamics. The variable transformations are defined by

$$H = \frac{r^3 - R^3}{3} \quad (38)$$

$$\tau = t$$

so that

$$\bar{T}(H, \tau) = T(r, t) \quad (39)$$

Since the T -equation results directly from the momentum or vorticity equations the right hand side (RHS) of this equation must be

derived from

$$(\nabla_{\mathbf{x}}) \nabla \cdot \int_{-\infty}^{\tau} \mathbf{N}(t-\tau') \dot{\underline{\underline{\gamma}}}(H, \tau') d\tau' \quad (40)$$

for the strain rate tensor $\dot{\underline{\underline{\gamma}}}$. The new T equation becomes:

$$\begin{aligned} \frac{\partial T}{\partial \tau} - 2R^2 \dot{R} \frac{T}{L^3} = \nu L \{ 2 \frac{\partial T}{\partial H} + L^3 \frac{\partial^2 T}{\partial H^2} - n(n+1) \frac{T}{L^3} \} \\ + G_0 \left\{ \frac{1}{L} \int_{-\infty}^{\tau} \exp\left(\frac{\tau'-\tau}{\lambda}\right) I_1(H, \tau') d\tau' \right. \\ + 2L^2 \int_{-\infty}^{\tau} \exp\left(\frac{\tau'-\tau}{\lambda}\right) I_2(H, \tau') d\tau' \\ \left. + L^5 \int_{-\infty}^{\tau} \exp\left(\frac{\tau'-\tau}{\lambda}\right) I_3(H, \tau') d\tau' \right\} \quad (41) \end{aligned}$$

where

$$\begin{aligned} I_1 = 2n(n-1)(n-2) X_n(H, \tau) L^{(n-2)} \\ - 2(n+1)(n+2)(n+3) Z_n(H, \tau) L^{-(n+3)} \\ + n(n+1) \frac{T_n(H, \tau)}{L} \end{aligned}$$

$$\begin{aligned} I_2 = -2(n^2+n+4) \frac{T_n(H, \tau)}{L^5} \\ - (2n-5)(n-1)(n-2) X_n(H, \tau) L^{(n-5)} \\ + (n+2)(n+3)(2n+7) Z_n(H, \tau) L^{-(n+6)} \end{aligned}$$

$$\begin{aligned}
I_3 &= 2(n^2+n+8) \frac{T_n(H,\tau)}{L^7} \\
&+ 2(n-1)(n-2)(n-5)X_n(H,\tau)L^{(n-8)} \\
&- 2(n+2)(n+3)(n+6)Z_n(H,\tau)L^{-(n+9)} \\
&- \frac{1}{L} \frac{\partial^2 T_n}{\partial^2} + \frac{4}{L^4} \frac{\partial T_n}{\partial H}
\end{aligned}$$

$$L(H) = (3H + R^3)^{1/3}$$

and

$$X_n(H,\tau) = \alpha_n(\tau) - A_n(\tau) + \frac{n+1}{2n+1} \int_R^L S^{-n} T_n(H,\tau) dS$$

$$\begin{aligned}
Z_n(H,\tau) &= \frac{n}{n+1} R^{2n+1} [\alpha_n(\tau) - A_n(\tau)] \\
&+ \frac{n+1}{2n+1} \int_R^L S^{n+1} T_n(H,\tau) dS
\end{aligned}$$

and the function $A(\tau)$ is zero for an externally quiescent fluid and is introduced in the far-field conditions (Section IV). See Appendix A for a derivation of this expression.

There are also new complications in the formulation of the boundary conditions at the bubble surface. A distinction emerges between terms which arise from the stress expression and those in the unit normal

vector. In the viscoelastic case, terms obtain such as

$$\int_{-\infty}^{\tau} N(\tau-\tau') \frac{a(\tau') \dot{R}(\tau')}{R^2(\tau')} d\tau' \quad (42)$$

and

$$\frac{a(\tau)}{R(\tau)} \int_{-\infty}^{\tau} N(\tau-\tau') \frac{\dot{R}(\tau')}{R(\tau')} d\tau' \quad (43)$$

which are equal in the viscous limit, but must be distinguished in this application. The normal stress boundary condition is altered both in this regard and by changes in the T-equation. The $O(\epsilon)$ v-pressure is calculated by the spatial integration of the equation of motion (see Appendix A)

$$\begin{aligned} P_v(H=0, \tau) & \quad (44) \\ &= R^3 \int_{-\infty}^{\tau} N(\tau-\tau') \\ & \quad \left\{ -\frac{1}{R} \frac{\partial T}{\partial H} + 3 \frac{T}{R^4} - 2[(n-1)(n-2) + (n+2)(n+3) \left(\frac{n}{n+1}\right)] \right. \\ & \quad \left. R^{(n-5)} (\alpha-A) \right\} d\tau' \\ &+ \int_{-\infty}^{\tau} N(\tau-\tau') \left\{ -3 \left(\frac{T}{R}\right) \right. \\ & \quad \left. + 2[(n-1)(n-2) + (n+2)(n+3) \left(\frac{n}{n+1}\right)] R^{(n-2)} (\alpha-A) \right\} d\tau' \\ &+ \frac{2(2n+1)}{n+1} R^n \left(\frac{\dot{R}}{R}\right) (\alpha-A) \end{aligned}$$

$$\begin{aligned}
& + \dot{R} T(H=0, \tau) \\
& - R^n \int_R^\infty s^{-n} \left(\frac{\partial T}{\partial \tau} \right) ds \\
& - R^n \left(\frac{2n+1}{n+1} \right) \frac{\partial A}{\partial \tau}
\end{aligned}$$

The new normal stress boundary condition becomes (see Appendix A)

$$\begin{aligned}
& \frac{\ddot{R}a}{n+1} + \frac{3}{n+1} \dot{R}\dot{a} - 2(n-1)(n+2) \int_{-\infty}^{\tau} N' \frac{\dot{a}}{R} d\tau' \\
& + \left(-\frac{n-1}{n+1} \right) \ddot{R}a - 4(n-1)(n+2) \int_{-\infty}^{\tau} N' \frac{a\dot{R}}{R^2} d\tau' \\
& + 6n(n+1) \frac{a}{R} \int_{-\infty}^{\tau} N' \left(\frac{\dot{R}}{R} \right) d\tau' \\
& - 12 aR^2 \int_{-\infty}^{\tau} N' \left(\frac{\dot{R}}{R^4} \right) d\tau' + (n-1)(n+2) \frac{\sigma/\rho}{R^2} a \\
& + n(n+1) \int_{-\infty}^{\tau} N' \left(\frac{T}{R} \right) d\tau' + P_v(H=0, \tau) = 0 \tag{45}
\end{aligned}$$

where σ is the surface tension constant and $N' = N(\tau - \tau')$, which is viewed as an equation of motion for $a(t)$. This must be solved

consistent with the T-equation and the tangential stress boundary condition. (See Appendix A.)

$$\int_{-\infty}^{\tau} N' \left\{ 2(n+2) \left(\frac{\dot{a}}{R} + \frac{2a\dot{R}}{R^2} \right) - (n+1) \frac{T}{R} + 2(2n+1)R^{(n-2)}(a-A) \right\} d\tau'$$

$$- 6(n+1) \frac{a}{R} \int_{-\infty}^{\tau} N' \frac{\dot{R}}{R} d\tau' = 0 \quad (46)$$

It is useful to note that these equations do reduce to their viscous counterparts when the elastic contribution is zero. In particular, the spatial integrals of the T field are seen to cancel identically in the instantaneous dissipation limit. (See Appendix A.3.)

Viscoelastic calculations for the considerably simpler special case when $R = R_0$, have been performed by Inge and Bark (1981) using Laplace transform techniques while including a linearized 3-constant Oldroyd model. Their results supply a useful check on techniques which allow time-dependent $R(t)$ values.

The system of equations governing the asymmetric dynamics developed here is linear in all of the $O(\epsilon)$ quantities, i.e. $a_n(\tau)$, $T_n(H, \tau)$, $A_n(\tau)$ and their integrals and derivatives. This linearity emerges from the assumption that terms which are second order in ϵ , representing convected momentum fluxes and also convected and co-rotational and/or co-deformational contributions to the non-Newtonian

stress, are small enough to be neglected. However, the constitutive model employed does not neglect all nonlinear contributions to the stress, the Lagrangian coordinate transformation incorporates convection by terms of zero order in ϵ . Thus, this is not merely a linear viscoelastic model. Furthermore, at this first order in ϵ , the integral model of Equation (III.9) is equivalent to many others in integral form including the linear Jeffreys model (Bird, Armstrong & Hassager, p. 279), the co-rotational Jeffreys model (p. 328) and the Oldroyd 8-constant model (p. 371).

The neglect of terms of second order in ϵ , restricts the conditions for which the equations are valid to motions exhibiting small deformations from the purely radial, $O(\epsilon^0)$ motion. The prescription for "small" values, which determines ϵ , can also be viewed in terms of the harmonic expansion which is the basis for the separation of angular and radius-temporal dependences in equation (25). By treating each set of equations (41), (44), (45) and (46) for each value of the index n , independent of other n values, the linear independence of the modes (spherical harmonic angular dependences) is invoked. This implicitly means that any asymmetric field, nonsphericity, velocity, pressure or stress with specific angular dependence $Y_n^m(\theta, \phi)$ will "excite" and be "excited" by only quantities with that same angular dependence. In reality this can be violated by inertial terms or by convected elastic contributions from angular or radial strains and the resulting stresses. In the viscoelastic stress term the possible contributions can be evaluated mathematically and this is done in Appendix B.2.

IV. INITIATION AND FAR-FIELD CONDITIONS

In order to solve for a_n and thus, the shape of the cavity, the viscous equations (III.27), (III.32) and (III.34) or the viscoelastic system (III.41), (III.44), (III.45) and III.46) must be solved simultaneously subject to an $\theta(\epsilon^0)$ $R(t)$ profile such as one generated through equation (III.4). Specification can also be made of ambient flow conditions in conjunction with (III.29) and (III.30). The Newtonian system is mathematically simpler than the equations containing the Maxwell-type model and complete problem specification can be achieved by two physical parameters μ/ρ and σ/ρ and two shape values per mode, $a_n(0)$ and $\dot{a}_n(0)$ at $\theta(\epsilon)$. For a bubble in a fluid with no externally imposed flow the system is well-posed.

Viscoelastic fluids add a non-instantaneous component, caused by fluid memory and represented here by time integrals, which give elastic stress accumulation. Behavior prior to some initial time, e.g. $t = \tau = 0$, is relevant to the determination of subsequent dynamics. It is no longer sufficient to specify $a_n(0)$ and $\dot{a}_n(0)$ only; the memory integrals must also be initialized.

Time zero is chosen to be that instant at which $\theta(\epsilon^0)$ spherical dynamics are initiated i.e.

$$\left. \begin{aligned} \dot{R}(t) = \ddot{R}(t) = 0 \\ R(t) = R_0 \end{aligned} \right\} t < 0 \quad (1)$$

so from equation (III.3)

$$R_0 = \frac{p^0 - p_v^0 - p_a^0}{2\sigma} \quad (2)$$

This also initiates the value of the elastic contribution up to time zero as zero at $O(\epsilon^0)$. For this vapor cavity ($P_g^0 = P_g(t) = 0$), motion is begun by a step change in ambient pressure

$$P_a(t) = P_a^0 - P^* H(t) \quad (3)$$

where $H(t)$ is the Heaviside step function. The sign of P^* determines the type of spherical dynamics

$P^* < 0$	$\dot{R} < 0$	Collapse	
$P^* = 0$	$\dot{R} = 0$	Static	(4)
$P^* > 0$	$\dot{R} > 0$	Growth	

For a particular value of P^* , and the physical parameters of Table 3 (in Section II), $R(t)$ vs. t profiles can be generated from equations (III.3) and (III.9) with (III.11) and one final condition

$$\dot{R}(0^+) = 0 \quad (5)$$

The initial conditions on the nonspherical terms which are analogous to those on the symmetric values given in equation (1) are

$$\left. \begin{aligned} \frac{\partial}{\partial t} T(r,t) &= 0 \\ \dot{a}(t) = \ddot{a}(t) &= 0 \end{aligned} \right\} t < 0 \quad (6)$$

The resulting equation and boundary conditions cannot be satisfied for arbitrary $a(t) = a_0$ since the surface tension term acts as an inhomogeneity for non-zero a_0 and finite R_0 , and it cannot be balanced by a toroidal field satisfying all three constraints. Thus, to conform to (6) the degenerate case is required

$$\left. \begin{aligned} T(r,t) &= 0 \\ a(r,t) &= 0 \end{aligned} \right\} t < 0 \quad (7)$$

However, without some additional disturbance only the trivial case of zero nonsphericities is invoked. The necessary inhomogeneity may be introduced by simply specifying $a_n(0)$ and $\dot{a}_n(0)$. Physically, this seems troublesome since a discontinuity in shape and/or nonspherical velocity is necessary. In the viscous case this objection is not relevant since both mathematically and physically the manner by which these initial values arise do not influence subsequent behavior. Thus, even if a discontinuity in $\dot{a}_n(t)$ at t_0 is specified which requires a physically unreasonable singularity in the acceleration $\ddot{a}_n(t_0)$, the problem is well-posed after t_0 . These same arguments cannot be forwarded for a viscoelastic medium, although conditions (6) do allow values to be assigned to the elastic integrals. For the viscoelastic fluid the manner by which the condition at time $t = 0$ arise is relevant to

subsequent ($t > 0$) behavior.

Results of simulations which incorporate the pre-zero static conditions (7) show only a small difference between a viscous fluid and one exhibiting viscoelasticity modelled by equation (III.9) with $\lambda > 10^{-5}$ seconds. (See Results, Section VI.) This is consistent with the expectation that viscoelasticity, modelled in this manner, will be cumulative and the observation that in the present case the duration of the nonspherical bubble dynamics is insufficient to allow stress accumulation.

The difference between viscous and viscoelastic responses in this analysis results from a difference in stresses symbolized by

$$\begin{aligned} \Delta(\text{stresses}) &= \\ &= \text{viscoelastic stresses} - \text{viscous stresses} \quad (8) \\ &= f(R,H) \int_{-\infty}^{\tau} N(\tau-\tau') \frac{e_e(H',\tau')}{f(R',H')} d\tau' - \nu f(R,H) \frac{e_v(H,\tau)}{f(R,H)} \end{aligned}$$

where

e_e = strain rate in viscoelastic medium

e_v = strain rate in viscous fluid

Thus, the difference in stresses can be viewed as resulting from three highly inter-related and interdependent components: the difference between the corresponding instantaneous strain rates e_e and e_v , a contribution caused by the $O(\epsilon^0)$ convection represented by $f(R,H)$ which might be called "geometric" and finally, the existence of a fundamental constitutive distinction between the "memory functions" $N(\tau)$ and $\nu \delta(\tau)$.

Initially neglecting the first two contributions so that

$$e_e \approx e_v = e \leq e_{\max}$$

and

$$f(R,H) \int_{-\infty}^{\tau} N(\tau-\tau') \frac{e_e(H',\tau')}{f(R',H')} d\tau' \quad (9)$$

$$\approx \int_{-\infty}^{\tau} N(\tau-\tau') e_e(H',\tau') d\tau' ,$$

a first estimate of the overall stress difference can be derived

$$\Delta(\text{stress}) = \int_{-\infty}^{\tau} \left(\frac{\nu}{\lambda}\right) \exp\left(\frac{\tau-\tau'}{\lambda}\right) e(\tau') d\tau'$$

$$\leq \nu e_{\max} [1 - \exp\left(\frac{\tau}{\lambda}\right)] \quad (10)$$

$$\approx \left(\frac{\tau}{\lambda}\right) \nu e_{\max} \quad \text{for small } (\tau/\lambda)$$

In evaluating the integral no contribution for all time previous to $\tau = 0$ is allowed since the set of initial conditions, Equations (6) & (7), specify no stress field for that period of time, which means

$$\int_{-\infty}^{\tau} \left(\frac{\nu}{\lambda}\right) \exp\left(\frac{\tau-\tau'}{\lambda}\right) e(\tau') d\tau'$$

$$= \int_0^{\tau} \left(\frac{\nu}{\lambda}\right) \exp\left(\frac{\tau-\tau'}{\lambda}\right) e(\tau') d\tau' \quad (11)$$

This approximation is useful for preliminary attempts to evaluate parameter sensitivity. One circumstance in which this result would be inaccurate is that of a large temporal variation in the geometric factor $f(R,H)$, rendering equation (9) invalid. However, while the resulting stress difference may be large, the variation in $f(R,H)$ obtains for large changes in $R(\tau)$ which also corresponds to an increase in inertial effects likely to decrease the net effect of stress on the amplitudes $a_n(\tau)$. Another situation which must be investigated since it would increase viscoelastic effects is any set of conditions which would make Equation (11) inaccurate. The time period before $t = 0$ represents the history of the fluid which can be important for fluids with memory, and a self-consistent scheme to describe this domain should be found.

A first attempt to initiate the stress integral might be to specify a non-zero constant amplitude a_0 in addition to the conditions stated in (6). However, a static inhomogeneous solution to the system does not exist. Apparently the transient problem must be treated to introduce nonsphericities and an asymmetric stress field prior to the initiation of spherical dynamics. The analysis will now divide the problem solution into two time intervals. One of these intervals, the second, corresponds to the full problem; after time $t = \tau = 0$, the system is solved for $a_n(\tau)$, while the spherical radius, $R(\tau)$, is allowed to vary in time. Before time zero, in the first time zone, $R(t) = R_0$, a constant, and a transient scheme to introduce and describe asymmetries in the system must be devised. This proposed theoretical scheme should be mathematically tractable and also allow a reasonable physical interpretation. If possible, this physical significance should be directly translatable to experimentally achievable conditions.

Since $R(t) = R_0$ and $\dot{R}(t) = \ddot{R}(t) = 0$ for all time $t = \tau < 0$ the complications introduced by a Lagrangian framework are not present and their (r, t) coordinate system can be chosen. The toroidal field equation then becomes

$$\frac{\partial T_n}{\partial t} = \int_{-\infty}^t N(t-t') \left[\frac{\partial^2 T_n}{\partial r^2} - \frac{n(n+1)}{r^2} T_n \right] dt' \quad (12)$$

If a separable solution is assumed to exist

$$T_n(r, t) = R \left\{ \sum_j \chi_{n,j} \theta_{n,j}(t) \rho_{n,j}(r) \right\} \quad (13)$$

where $\theta_{n,j}(t)$ are functions only of time, $\rho_{n,j}$ only of r and $\chi_{n,j}$ are constants, then

$$\rho_{n,j}(r) = K_{n,j} \left(\frac{d^2 \rho_{n,j}}{dr^2} - \frac{n(n+1)}{r^2} \rho_{n,j} \right) \quad (14)$$

$$\text{and } K_{n,j} \frac{d\theta_{n,j}}{dt} = \int_{-\infty}^t N(t-t') \theta_{n,j}(t') dt' \quad (15)$$

where $K_{n,j}$ is a particular constant of separation. A steady state contribution to the solution is

$$\theta_0(t) = 1$$

$$T_n^{SS}(r) = \chi_n^{SS+} \left(\frac{r}{R_0} \right)^{n+1} + \chi_n^{SS-} \left(\frac{R_0}{r} \right)^n \quad (16)$$

since this part of the velocity field is bounded as $r \rightarrow \infty$ $\chi_n^{SS+} = 0$. From equation (III.30)

$$\chi_n^{SS-} = - \frac{\chi_r^{SS}}{(2n+1)R_0} \quad (17)$$

The temporal equation has solutions of the form

$$\theta_j(t) = \exp \left[\left(\frac{1}{\zeta_j} \pm i\omega_j \right) t \right] \quad (18)$$

which means that the separation constant is complex

$$K_j = \frac{v + \left(\frac{G}{\rho} \right) / \left[\frac{1}{\lambda} + \frac{1}{\zeta_j} + i\omega_j \right]}{\frac{1}{\zeta_j} + i\omega_j} \quad (19)$$

for the relaxation function $N(t)$. By requiring the solution to be bounded as $t \rightarrow -\infty$, the decay time ζ_j is restricted to nonnegative values.

The spatial equation (14) can be transformed into a version of Bessel's equation. For $n = 2$, the two independent modified spherical Bessel functions relevant to the solution are

$$F_1(x) = \left(\frac{3}{x^3} - \frac{3}{x^2} + \frac{1}{x} \right) e^x \quad (20)$$

$$F_2(x) = \left(\frac{3}{x^2} + \frac{3}{x^2} + \frac{1}{x} \right) e^{-x}$$

for the transformations

$$x = \frac{r}{\sqrt{k_j}}$$

$$\rho(r) = r F(r)$$

$F_1(x)$ is not bounded as $r \rightarrow \infty$, so only $F_2(x)$ contributes to the solution. The spatial integral $\alpha_2(t)$ consist of terms of the form

$$a_{2,j}(t) = \theta_j(t) \chi_{2,j} \left(-\frac{3}{5}\right) \quad (21)$$

$$\int_{R_0}^{\infty} \sqrt{K_j} \exp\left(-\frac{3S}{\sqrt{K_j}}\right) \left[\frac{K_j}{S^2} + \frac{3\sqrt{K_j}}{S}\right] \frac{dS}{S^2}$$

or

$$a_2(t) = \int_j \left(-\frac{3}{5}\right) \chi_j \theta_j(t) (D_j^3 + D_j^2) \exp\left(\frac{-1}{D_j}\right) \quad (22)$$

when $D_j = \sqrt{K_j} / R_0$.

The time dependent portion of this toroidal function is an exponentially growing oscillation of frequency ω_j which occurs between $t = -\infty$ and $t = 0$. The time constant and frequency of $\theta_j(t)$ can be specified independent of any variables or parameters of the physical system as currently described. This will fix the separation constant K_j which, in turn, determines the spatial function $\phi_j(r)$. When an individual transient mode is excited, it is the form of the time dependence of all the dynamics. Thus, if a physical mechanism or apparatus could be visualized to drive some event with form $\theta_j(t)$, all asymmetries would be similarly driven. In $O(\epsilon^0)$ dynamics, initiation was accomplished by changing the far-field conditions through the ambient pressure. An initiation of $O(\epsilon^1)$ dynamics through far-field conditions would be ideal.

The oscillatory time-dependence is reminiscent of rheological testing which employs oscillatory motions. In this analysis, far field flow conditions are governed by $a_n(t)$ in $\phi_n(r, \theta, \phi, t)$ (see equations III.29 and III.30). The value of $a_n(t)$ in equation (III.30) results when the

velocity field v_1 is required to decay as r increases. A way to alter that requirement is to add a time dependent term to the old $\alpha_n(t)$ expression

$$\alpha_n^{\text{flow}}(t) = \alpha_n(t) - \sum_j A_j \theta_j(t) = \alpha_n(t) - \sum_j A_j(t) \quad (23)$$

which is formed with the "appropriate" time dependence $\theta_j(t)$. The velocity field as $r \rightarrow \infty$ is

$$v_1^\infty = \sum_n \nabla [A_j \theta_j(t) r^n Y_n^m(\theta, \phi)] \quad (24)$$

For the particular case $n = 2$

$$\begin{aligned} (v_1)_r &\rightarrow 2A_j \theta_j(t) r Y_2^m \\ (v_1)_\theta &\rightarrow A_j \theta_j(t) r \frac{\partial Y_2^m}{\partial \theta} \\ (v_1)_\phi &\rightarrow A_j \theta_j(t) \frac{r}{\sin \theta} \frac{\partial Y_2^m}{\partial \phi} \end{aligned} \quad (25)$$

When $m = 0$, this represents a three-dimensional elongational flow with extension along the Z - or $\theta = 0$ - axis, and time-dependent elongation rate $A_j \theta_j(t)$ (see Figure 6a). The $m = 1$ and $m = 2$ cases, with $n = 2$, are two-dimensional elongational flows with rates $A_j \theta_j(t)/6$ in the y - z and x - y planes, respectively. (See Figures 6b and 6c.) These latter two flows are particularly convenient since they can very nearly be achieved experimentally in the Taylor four-roller apparatus.

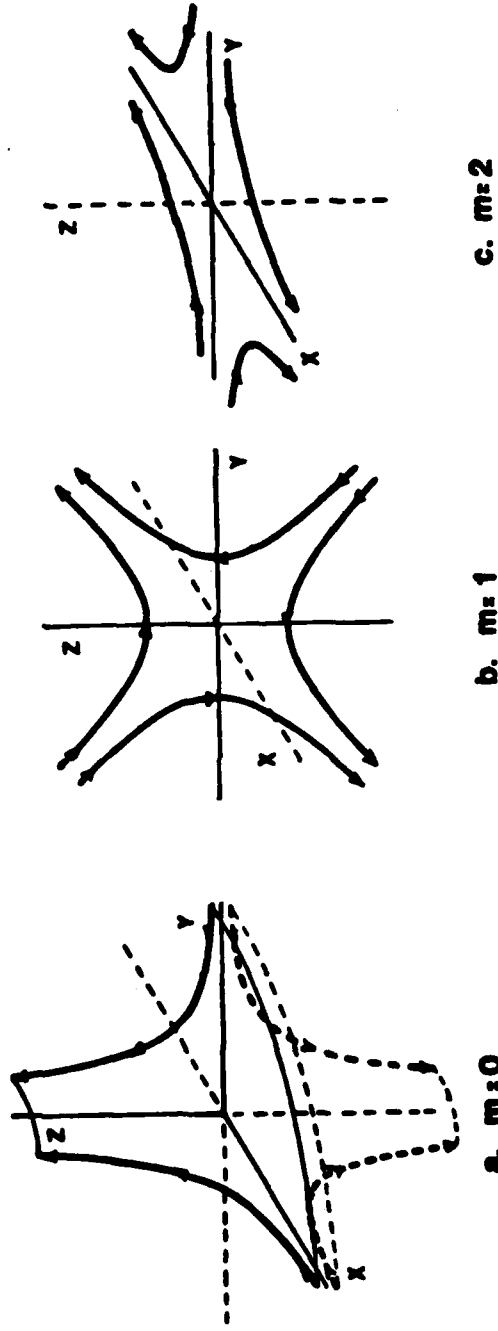


Figure 6. External Flows, \vec{v}_1^E , for $Y_2^E(\theta, \phi)$

The shapes of the bubbles created by these flows are given by (III.12), i.e. the deviation from the sphere is given by $Y_2^m(\theta, \phi)$ with amplitude $a(t)$. Representative shapes are shown in Figures 7(a) and 7(b), 8 and 9. Figure 10 shows the streamlines of the actual external flow around a spherical body.

The new far field condition must be applied to the boundary conditions. All $\alpha_n(t)$ must be replaced by $\alpha_n^{\text{flow}}(t)$. The flow term will also appear in the pressure term $P_v(r, t)$, Equation (III.44) since it arises from the equation of motion which employs the velocity, not vorticity and the velocity field includes the influence of the flow. The tangential stress condition for time $t < 0$ requires the value of toroidal function to be

$$T_2(R, t) = \chi_j \theta_j(t) R_0 D_j (3D_j^2 + 3D_j + 1) \exp\left(-\frac{1}{D_j}\right) \quad (26)$$

and with a new intermediate function $\psi_j(t)$

$$\psi_j(t) = \theta_j(t) [10 A_j + 3 \chi_j \exp\left(-\frac{1}{D_j}\right) D_j (5D_j^2 + 5D_j + 1)], \quad (27)$$

that

$$a_2(t) = a_{\infty} + \frac{R_0}{8} \sum_j \frac{\psi_j(t)}{\frac{1}{\tau_j} + i\omega_j} \quad (28)$$

Again the constant displacement a_{∞} must be zero as in Equation (7). The normal stress balance then completely determines the solution for all times $t < 0$. The final result is expressed through a cascade of new

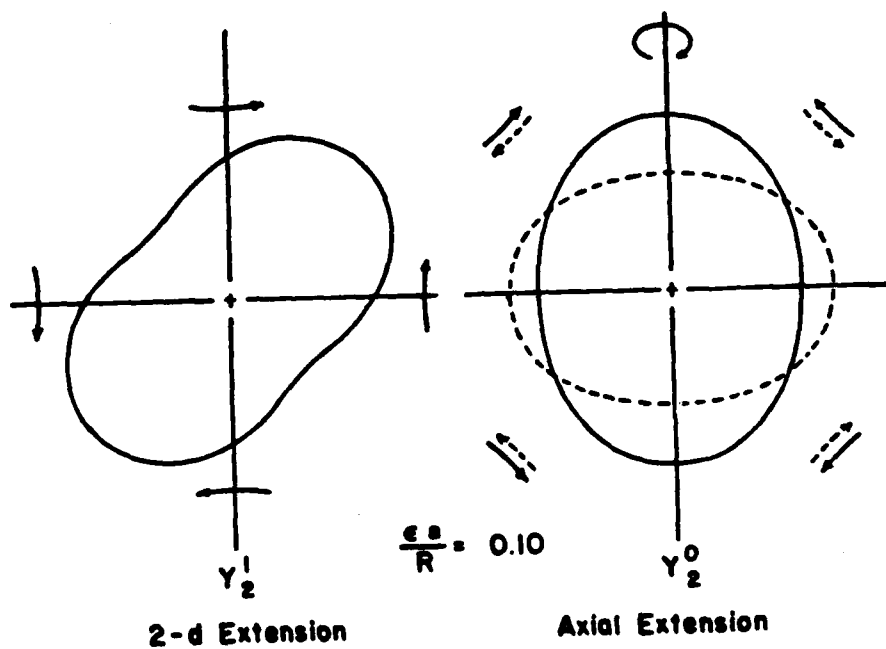


Figure 7. Shapes Created by External Flows

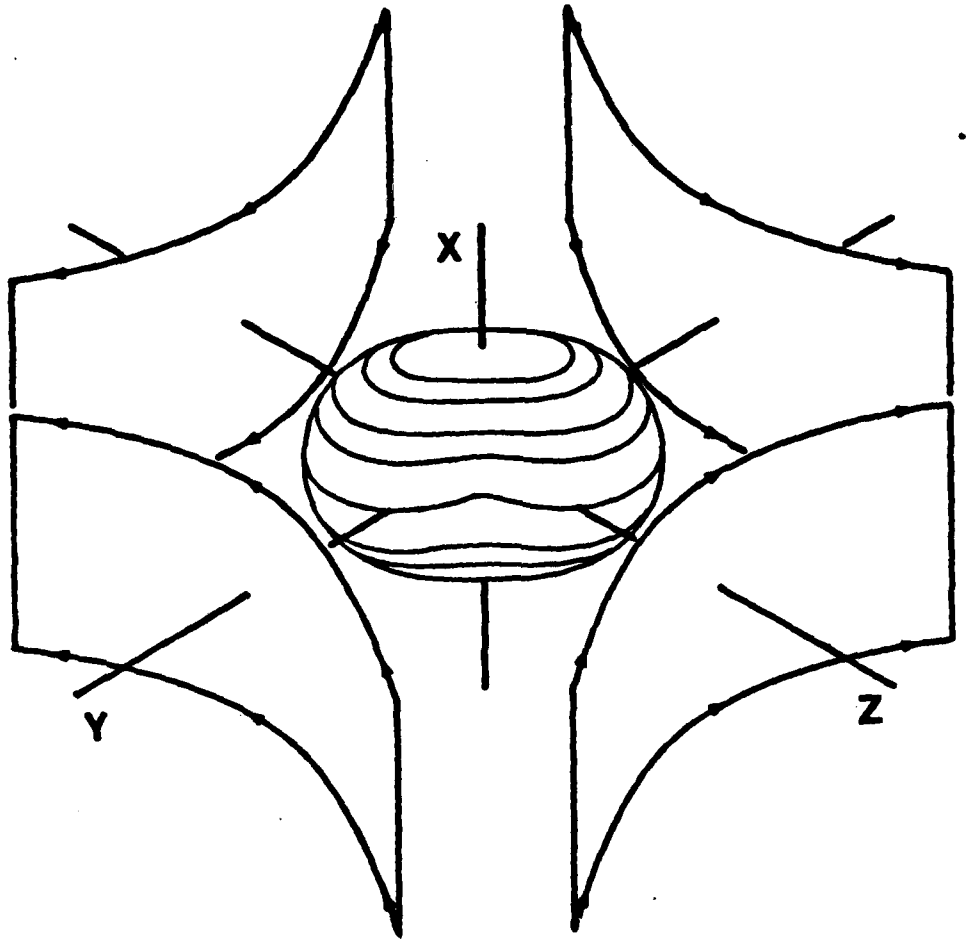


Figure 8. Representative Bubble Shape
and External Flow for $Y_2^1(\theta, \phi)$
Stream surfaces are shown along with
bubble shape.

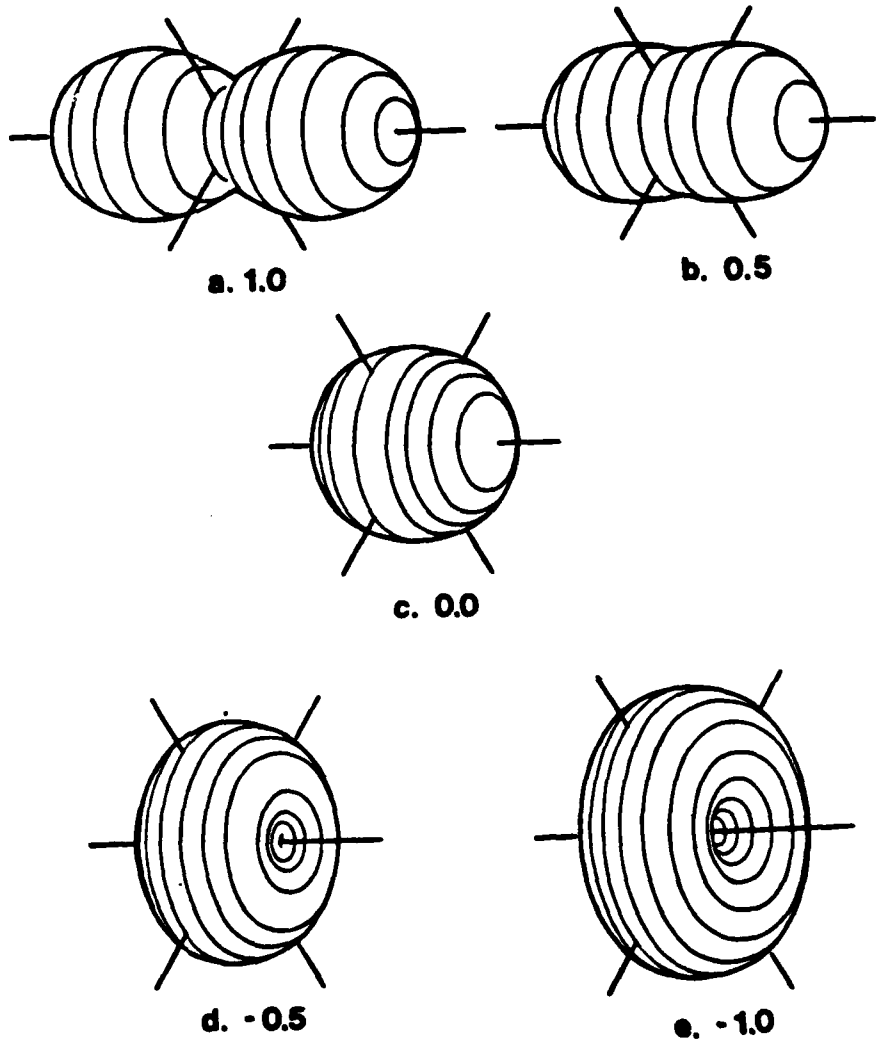


Figure 9. Shapes for $r = R + \epsilon a_2 Y_2^0(\theta, \phi)$
 Labels give values of $\frac{\epsilon a_2}{R}$

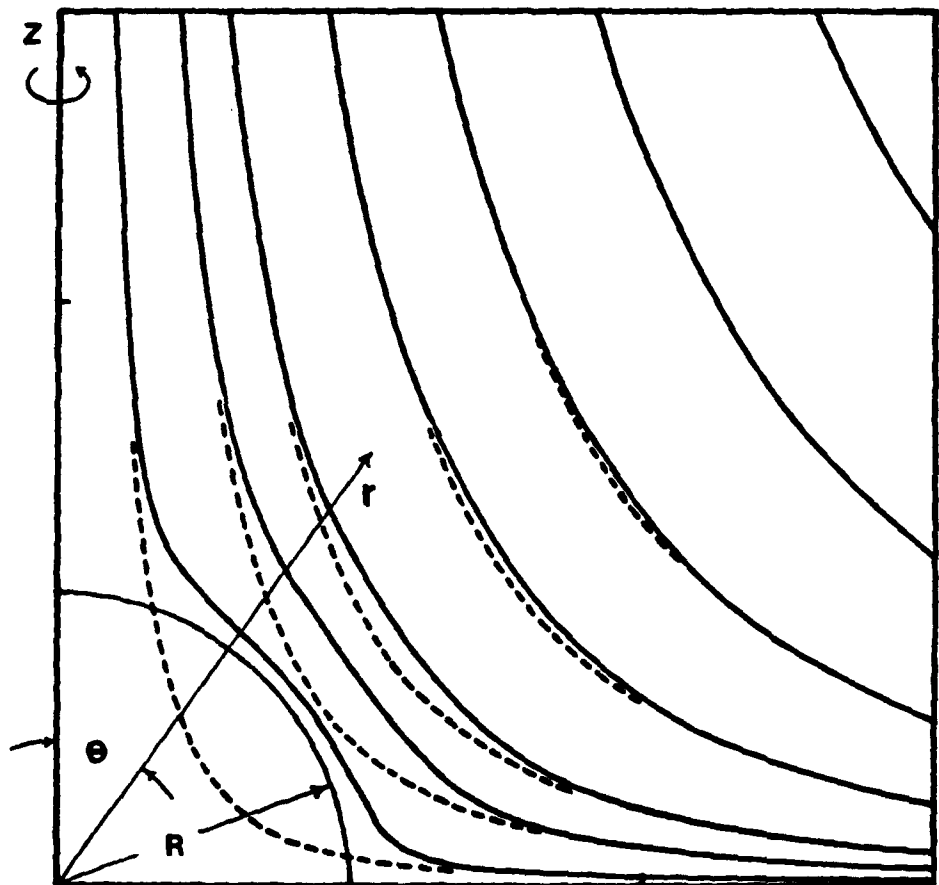


Figure 10. Alteration of Streamlines by Sphere
 for $Y_2^0(\theta, \phi)$
 without sphere \leftrightarrow pure extension
 with sphere \leftrightarrow v_1^{∞}

complex variables

$$\begin{aligned}
 \beta &= \frac{1}{\lambda} \quad , \text{ for fluid relaxation time } \lambda \\
 y_{\xi} &= \frac{1}{\zeta_j} \pm i\omega j \\
 y_B &= v + \frac{G_o/\rho}{\beta + y_{\zeta}} \\
 y_C &= \left(\frac{R_o}{3}\right)y_{\zeta} - \left(\frac{8}{R_o}\right)y_B + \frac{4\sigma}{R_o y_{\zeta}} \\
 y_D &= \exp\left(-\frac{R_o}{\sqrt{K_j}}\right) \left(\frac{\sqrt{K_j}}{R_o}\right) \\
 y_{BT} &= (\beta + y_{\zeta}) \frac{y_{\zeta}}{G_o/\rho + v(\beta + y_{\zeta})} \\
 y_S &= y_D \left[3y_{BT} + \left(\frac{64}{R_o}\right)y_B y_{\zeta} / y_a \right]
 \end{aligned} \tag{29}$$

with the final result

$$\chi_j = \left[-110 + \left(\frac{40R_o}{3}\right) \frac{y_{\zeta}}{y_C} \right] \frac{A_j}{y_S} \tag{30}$$

Evaluation of the velocity and stress fields, as well as the bubble shape is now possible.

Notice that χ_j is complex and varies linearly with the complex strain rate A_j . Large stresses and nonsphericities can be generated by specifying a large $|A_j|$, but are subject to restraints on the validity of the viscoelastic model, as discussed earlier, and by experimental practicability.

The behavior of the external flow after spherical dynamics are initiated at time $t = 0$ is a new consideration. If ζ_j is not large compared to the positive time period of interest, then the elongational rate will grow to large values. Therefore, at time $t = 0$, a new damping factor might be assigned to the flow and since the full equations will be solved numerically, without the separation of variables in equation (13), this is mathematically allowable.

The introduction of the external flow terms allows the problem to be physically and mathematically well-posed at time $t = \tau = 0$. All quantities now have physically meaningful, unambiguous values. Looking toward the expected behavior for subsequent times ($t > 0$), the same intuitive arguments presented as expressions (8), (9) and (10) suggest the kind of parameter sensitivity to be expected; any combination of parameters which correspond to small instantaneous strain rates, but allow accumulation over long times, e.g. small ω_j and $\zeta_j \gg \lambda$, would show the largest elastic changes.

V. EXPERIMENTAL PROGRAM

1. Introduction

In conjunction with the theoretical analysis of nonspherical bubbles in viscous and viscoelastic fluids, an experimental program was begun to test the model and attempt to isolate the most important factors in real cavitation inhibition. The use of dilute polymer solutions was natural in view of the initial motivation for this work, yet added complications due to the lack of rheological measurements available on such fluids. Results confirm the prediction that inertia would dominate spherical bubble dynamics and also demonstrated the viability of our technique in creating nonspherical cavities.

The criteria for the experimental system were very straightforward; it must have the capability to

- 1) create spherical bubbles which remain spherical
- 2) create nonspherical bubbles reproducibly
- 3) allow introduction of various flows
- 4) record these bubble sizes and shapes.

Of course all of this must be possible in various fluids with some flexibility with regard to bubble size.

Previous workers had used numerous techniques to study single bubble dynamics. The simplest is probably the introduction of a cavity by inflation using a device such as a syringe, then withdrawing the instrument and utilizing surface tension to seal the bubble. A variation on the same method depends upon buoyancy to pull the gas

volume off the "inflating needle".

The technique has been employed with success by Pearson and Middleman (1974, 1977, 1978) to generate elongational flows as a tool in fluid characterization. However, their elongation rates of order 1 second^{-1} are much smaller than those relevant to cavitation bubble collapse, where the time scales are much smaller and dissipative mechanisms much less important to spherically symmetric motion. As a consequence of the Reynolds number regime into which Pearson and Middleman's work can be classified, useful results can be extracted without regard for any nonspherical shape using only a pressure parameter. Thus, the presence of a physical apparatus, which introduces asymmetries into the bubble environment was not an impediment to that work, but would be when small nonsphericities are important.

One way to remove the apparatus from the immediate vicinity of the bubble has been to allow the cavity to move away from any bubble forming device through buoyancy driven motion. Hassager (1977, 1979), Coutenceau and Hajjam (1981) and others have studied both viscous and viscoelastic effects in this manner. However their bubbles are usually large, have constant volume, and the first order effects are not inertial. Once again, nonsphericities arise, but it is the steady shape of the bubble which is of primary interest.

Experimental events with dynamics more closely resembling cavitation bubbles can be generated by the rapid discharge of electrical potentials of the kilovolt range across electrodes in the working fluid. Gibson and Blake as well as Chahine and his co-workers have had considerable success with this technique in studying the inter-

action of the bubble with various controlled asymmetrical environments such as solid walls or free surfaces. Their configurations confer a planar symmetry on their experiments which appears to be unimportant for the study of the highly deformed shapes which arise due to the presence of a planar boundary. None of these experiments includes the velocity fields which are present in flow cavitation. The flow patterns might well be altered by the presence of velocities in the regions of high shear where cavities should be formed, if these devices were used with flow.

2. Apparatus

A technique which requires no apparatus in the fluid in the region where bubble forms, has been pioneered by Lauterborn (1981) and his co-workers. A laser can be used to focus electromagnetic energy sufficiently to generate cavities. The non-invasive character of this method makes it the most promising and flexible to study the variety of conditions necessary for the testing of the model system analysis.

The apparatus used for the present experiments is represented schematically in Figure 11 and with a photo, Figure 12. The major component, a ruby/glass laser, generates maximum output of 1.5 J in 15-30 nsec. The effective width of this beam as detected by spot burning tests was about 1 cm, which sized the focussing lens system. The final design for the cavitation chamber without flow was a parallelepiped constructed from PMMA with a useful interior which approximates a cube 11.5 cm per side. The wall through which the

APPARATUS

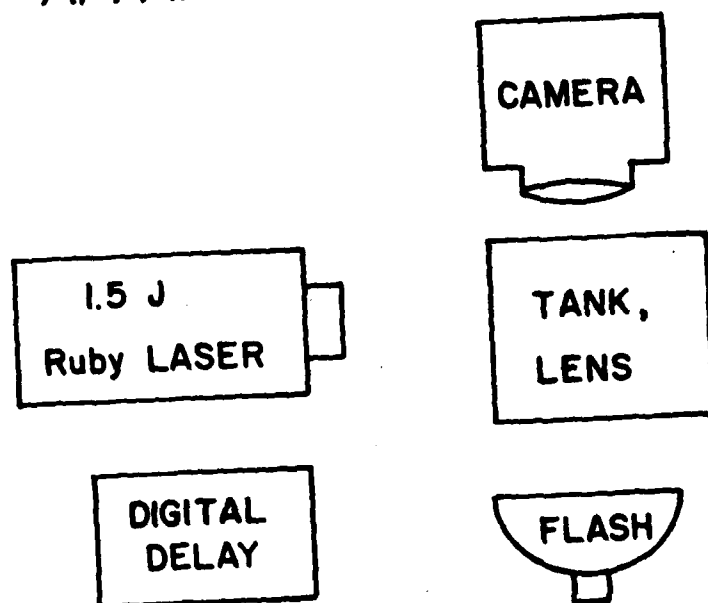


Figure 11. Major Components of Optical Cavitation Apparatus

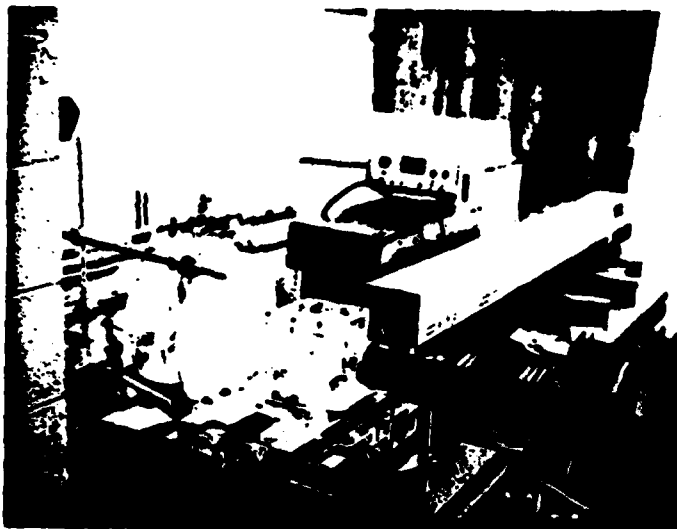
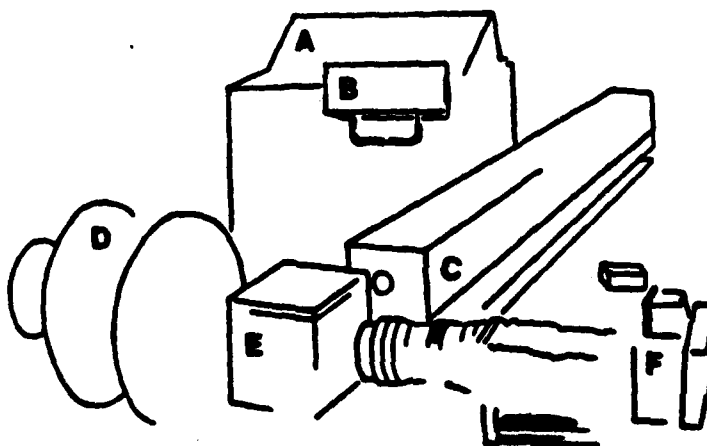


Figure 12.

Arrangement of Apparatus Showing:

- (A) control unit, (B) digital time delay,
- (C) ruby laser, (D) flash lamp and diffuser,
- (E) test cell, and (F) Hasselblad camera



laser beam enters the tank contained a plano-aspheric lens, mounted flush with the interior surface and properly sized to focus the beam to a critical volume.

By changing the single lens or employing a series of two lenses, the focal length of the optics could be altered. This was useful to evaluate the effect of the proximity of the lens surface which acts as a solid planar wall and also allowed the geometry of the beam focus to be changed. This becomes particularly important since it allows generation of nonspherical bubbles without far-field asymmetries.

The bubbles are recorded photographically with a single frame camera. Since the time scale of the phenomena is tens of microseconds conventional mechanical shutters are not adequate for the resolution necessary. Instead, photo exposure was accomplished with a digital time delay of rated accuracy $\pm 0.1 \mu\text{sec}$ triggering a flash to backlight the image which is transferred through an open camera shutter. High speed instant Polaroid black and white film captured images magnified four times (4X) by the lens and bellows system.

The apparatus listed in Table 4 allows three major adjustments in operating conditions.

1) Laser power infringing upon lens system. Gross adjustment is made by attenuating the beam using the schot glass filters. Finer adjustments are made by adjusting the charging voltage across the capacitor bank. To insure lasing of the rod a charge at least 70% of the maximum voltage was necessary. This translates to $(.7)^2 (1.5 \text{ J}) = .755 \text{ J}$. since energy is proportional to the square of the voltage.

2) Focal length L_f . and

3) Beam convergence angle θ_f .

TABLE 4. Equipment Specifications**Alignment Laser**

Hughes Model 4020
120 ma He-Ne

Power Laser

Apollo Laser, Inc. Model 5H
Ruby/Glass Q-switch
Power 1.5 J/S
Pulse Width 15-30 nsec

Digital Delay Generator

BNC Model 7010
used in range 0-99999 \pm 1 μ sec

Camera

Hasselblad Model 500C
w/Zeiss Planar 1:2.8, f = 80 mm lens and 12¹¹ extension

Film

Polaroid 667 high speed (ASA 600)
black and white instant development film

Flash

EG&G Electro Optics Model 85302
with Fresnel diffuser

Laser Focussing Lens

	focal length (in air)	diameter	Melles Griot #
Small	12 mm	17 mm	01 LAG 002
Medium	18	24	01 LAG 005
Large	25	32.5	01 LAG 117
Diverging Lens	-40	21	01 LPK 013

***Neutral Density Filters (Schot Glass)**

	Thickness	Designation	Approximate Absorbance
Low	1 mm	NG5	5X
Medium	2 mm	NG4	10-20X
High	3 mm	NG4	50X

*Supplied by Mr. Edwin Tolness, Princeton University PFL

These are two geometric parameters defining the geometric characteristics of the focussed beam. As shown in Figure 13, the "focal length" is defined as the distance from the planar surface of the flush-mounted lens to the point of highest energy concentration which is also the location of cavity-inception. As a first approximation this is simply the focal length in air of the optical system divided by the index of refraction of the medium (1.33 for water). The convergence is defined as that angle at which the beam is funneled. For a simple single law system, these two parameters are not independent since the diameter of the incident beam is fixed (nominally considered $D_{\text{beam}} = 1 \text{ cm}$). Linear optics gives the simple relationship

$$L_f = (D_{\text{beam}}/2) \cos \theta_f \quad (1)$$

If a second, diverging, lens is placed in series with the plano-convex converging lens it will increase the beam diameter impinging upon the primary lens so that although equation (1) is still valid, D_{beam} can be varied independently. Of course, L_f is now a simple function of the focal length of both lenses, approximated by

$$\frac{1}{1.33 L_f} = \frac{1}{f_1} + \frac{1}{f_2} \quad (2)$$

L_f , as stated previously, can be varied to assess "wall effects". Adjustment in θ_f should affect bubble shape. Intuitively there should be some critical energy density which incites cavity formation, large values of θ_f will localize this density sufficiently to create spherical

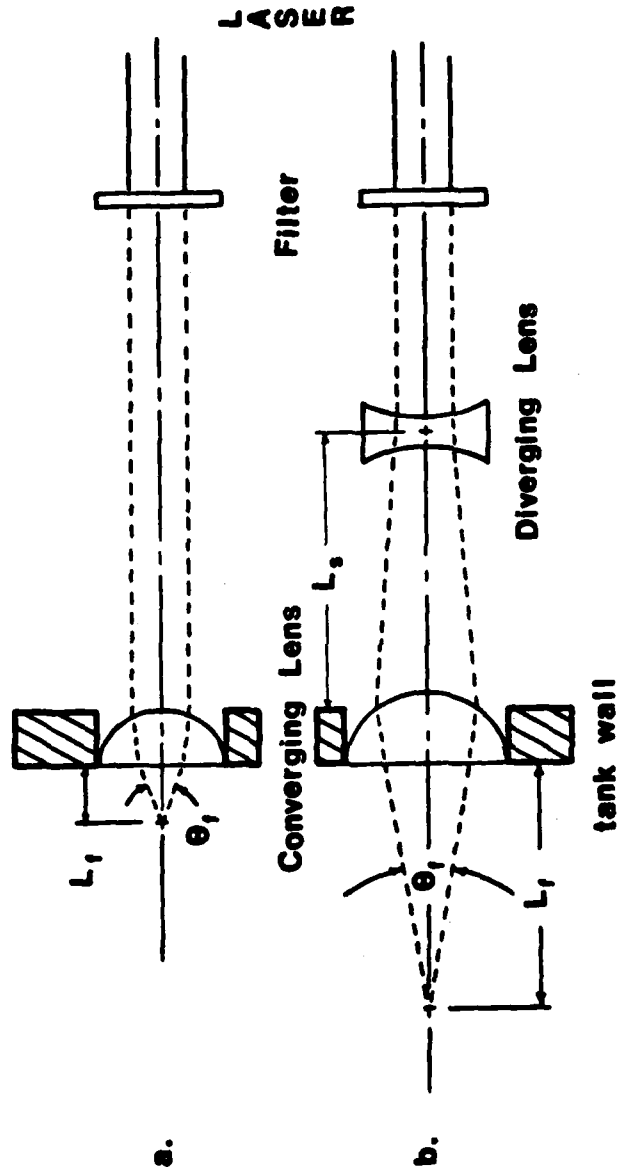


Figure 13. Laser Focusing Parameters

- a. single lens - small L_i , large θ_i
 - b. two lens system - large L_i , small θ_i
- These are adjusted through the separation distance L_s .

bubbles. Small values of θ_f should create a more extended volume with this critical concentration and thus elongated bubbles (see Figure 13(b))

3. Types of Trials

Four major types of experimental trials were performed:

1A) Spherical Bubbles in H₂O

These trials were performed to evaluate system reproducibility and determine the distances over which wall effects are present.

1B) Spherical Bubbles in Dilute Solutions

Although previous experiments using this optical cavitation technique have been performed in H₂O, similar trials in dilute aqueous polymer solution had not been reported. The first goal of these experiments was to guarantee the method's reliability in such solutions since scattering and differing inception characteristics might be expected. Once the technique was established the radial dynamics in polymer solutions could be compared to the results in pure water.

2) Initially Spherical Bubbles near Planar Surfaces in A) H₂O and B) polymer solutions.

The apparatus affords an excellent opportunity to investigate the effect of the proximity of a solid wall on the shape of a growing and collapsing bubble. Although presently, no theoretical analysis has been developed to treat the case for a viscoelastic fluid, qualitative comparison can be made in experiments very similar to those conducted by Chahine (1981) and others.

3) Nonspherical Bubbles in an "Infinite Medium"

A) H₂O and B) Polymer Solution

The mechanism by which nonsphericities arise is the lengthening of the "critical volume" described previously. Sequences of bubble photos allow a detailed comparison of the evolution of experimental shape as coupled with the growth and collapse of the cavity and theoretical predictions. This can be carried out both for the pure H₂O and various polymer solutions.

4) Initially Nonspherical Bubbles near Planar Surfaces

One possible cause for differences between experimentally produced bubbles near solid walls and real cavitation bubbles is a "competition" between jet formation and any other nonspherical modes which would reduce the energy available to the re-entering jets (see Discussion). A first attempt can be made to evaluate this possibility by producing nonspherical bubbles near solid walls with different orientations for that wall.

4. Fluids

Distilled water filtered through 3.0 μm Micropore^(R) filters was employed in most trials. The effect of boiling to degas the water was also tested. Preliminary trials showed that the distilled, filtered water was sufficiently clean to eliminate stray nucleation and allow reproducible trials.

The polymer solutions were prepared from polyacrylamide at M.W. $\sim 1.2 \times 10^6$ obtained from the American Cyanamid Corporation. The

polymer samples were approximately 20% hydrolyzed. Solutions by the slow addition of a weighed amount of polymer to a measured volume of distilled, deionized H₂O, then tumbled on rollers to insure homogeneity for at least twelve (12) hours. Initial trials were performed for solutions with concentrations of approximately 500 ppm since these definitely exhibit cavitation inhibition in water tunnel tests.

5. Photo Analysis

No sophisticated procedures were available for data analysis. Spherical bubble radius was measured directly from the photographs with an accuracy better than ± 0.05 cm/4. The sphericity was evaluated by overlaying circles and checking for visible deviation from that shape.

Nonspherical measurement was less straightforward and multiple techniques were evaluated. Each involved projection of the photograph onto a circular polar coordinate grid and the assumption of axial symmetry about the center line of the laser radiation. These analyses also require an assumption of the surface harmonics Legendre polynomials which contribute to the shape.

Appendix D contains sample data and more detail on procedures chosen. The final results showed differences in magnitude, but not in trends between the different numerical fits attempted so the simplest -- estimating R and a_L by measuring the major and minor axes of an image -- was employed.

VI. RESULTS

1. Theoretical Spherical Profiles

In order to generate nonspherical results, appropriate radius profiles to drive the asymmetries are necessary. Previous workers have concluded that dilute polymer solution rheology will not cause experimentally detectable changes in the overall size of a growing or collapsing bubble. Still, an $O(e^0)$ model similar to those of Fogler and Goddard (1970, 1971), Ting (1975), Yoo and Han (1982) and others, which incorporates viscoelasticity, but employs the parameter values of the present study (see Table 3), is useful to compare viscoelastic change in this geometry to changes in nonspherical behavior.

As presented in Section III, equation (4), an equation similar to Rayleigh's original result can be used to generate bubble profiles. The pressure initiated dynamics are completely specified by the dimensionless parameters of Table 5

TABLE 5. Dimensionless Parameters

$$Re = \frac{R_0^2 \rho}{\tau_0 \mu}$$

$$\pi = \frac{P^*}{P_V - P_a}$$

$$De = \frac{\lambda}{\tau}$$

$$El = \frac{G_0 \lambda}{\mu} = 1$$

$$V_0 = \frac{\dot{R}(0) \tau_0}{R_0}$$

where $R_0 = \frac{2\sigma}{P_v - P_a} \sim 10^{-3}$ cm. is the initial equilibrium bubble size for the present pressures and surface tension. Also, the Reynolds Number as defined here employs a ratio of the length and time scales to define the velocity scale since no other velocity scale emerges. The time scale, τ_0 , must still be defined. An $\theta(\epsilon^0)$ time scale might involve P^* since it determines the dynamics, however, from the bubble growth, collapse and constant radius cases, no single meaningful time scale emerges. A time scale independent of the particular dynamics is the surface tension time scale

$$\tau_0 = \sqrt{\frac{R_0^3 \rho}{\sigma}} \quad (1)$$

which relates to the period of an undamped oscillation in both the $\theta(\epsilon^0)$ spherical or $\theta(\epsilon^1)$ asymmetric modes.

Results for $R(t)$ vs. t for varying π are shown in Figures 14 and 15. For positive values of π , the bubble grows rapidly until the velocity $R(t)$ approaches a constant. Then is no change for any value of λ visible on the scale of the graph and numerical values show changes of less than 0.1%. As π decreases and becomes negative, collapse is described. Once again, in Figure 15, there is no visible change due to variation in λ , but $\dot{r}(t)$ does not approach a constant. The acceleration $\ddot{R}(t)$ appears to continually increase in magnitude, this is due to the surface tension term in the R equation.

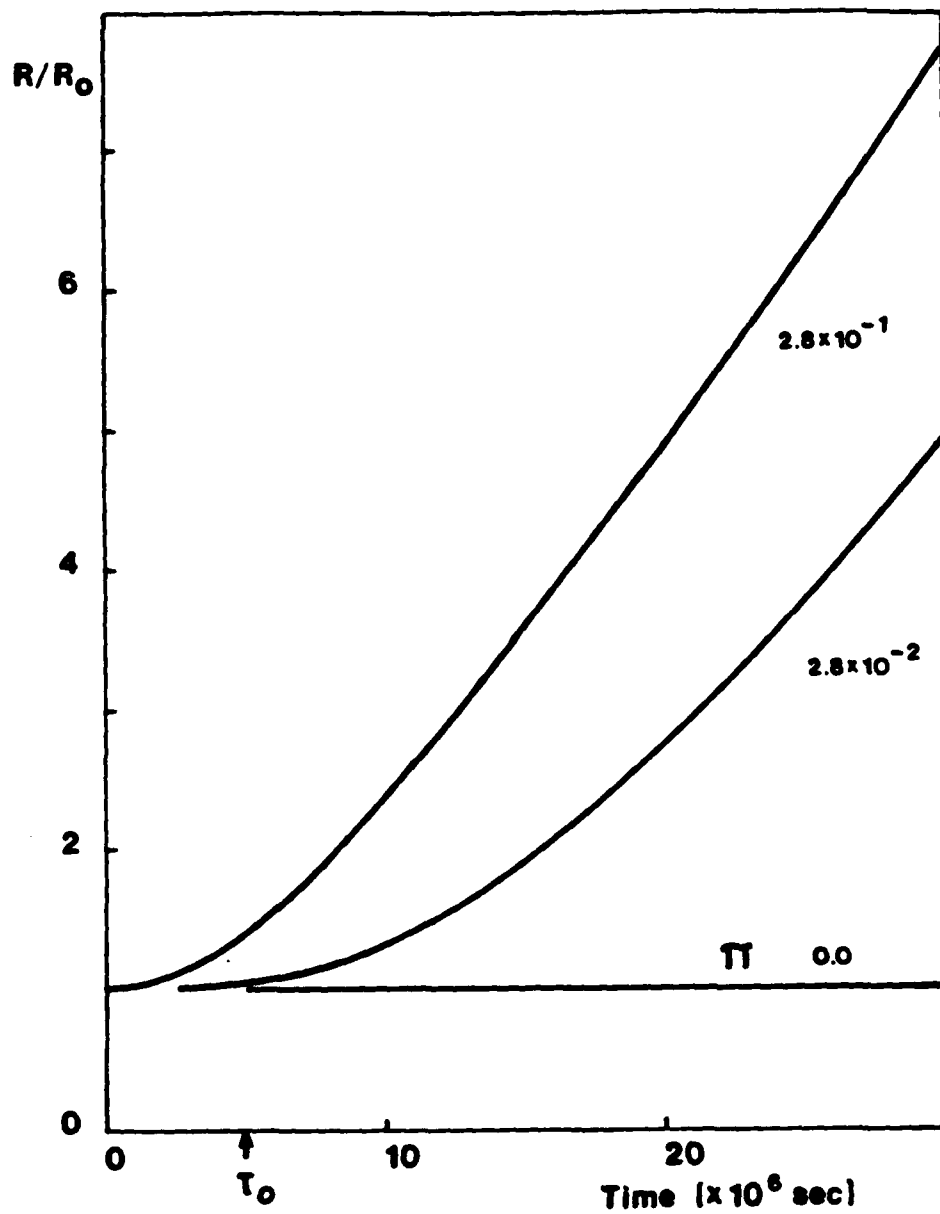


Figure 14. Spherical Radius vs. Time - Theoretical Growth

$$R = 1.03 \times 10^{-3} \text{ cm.}$$

(See Table 3)

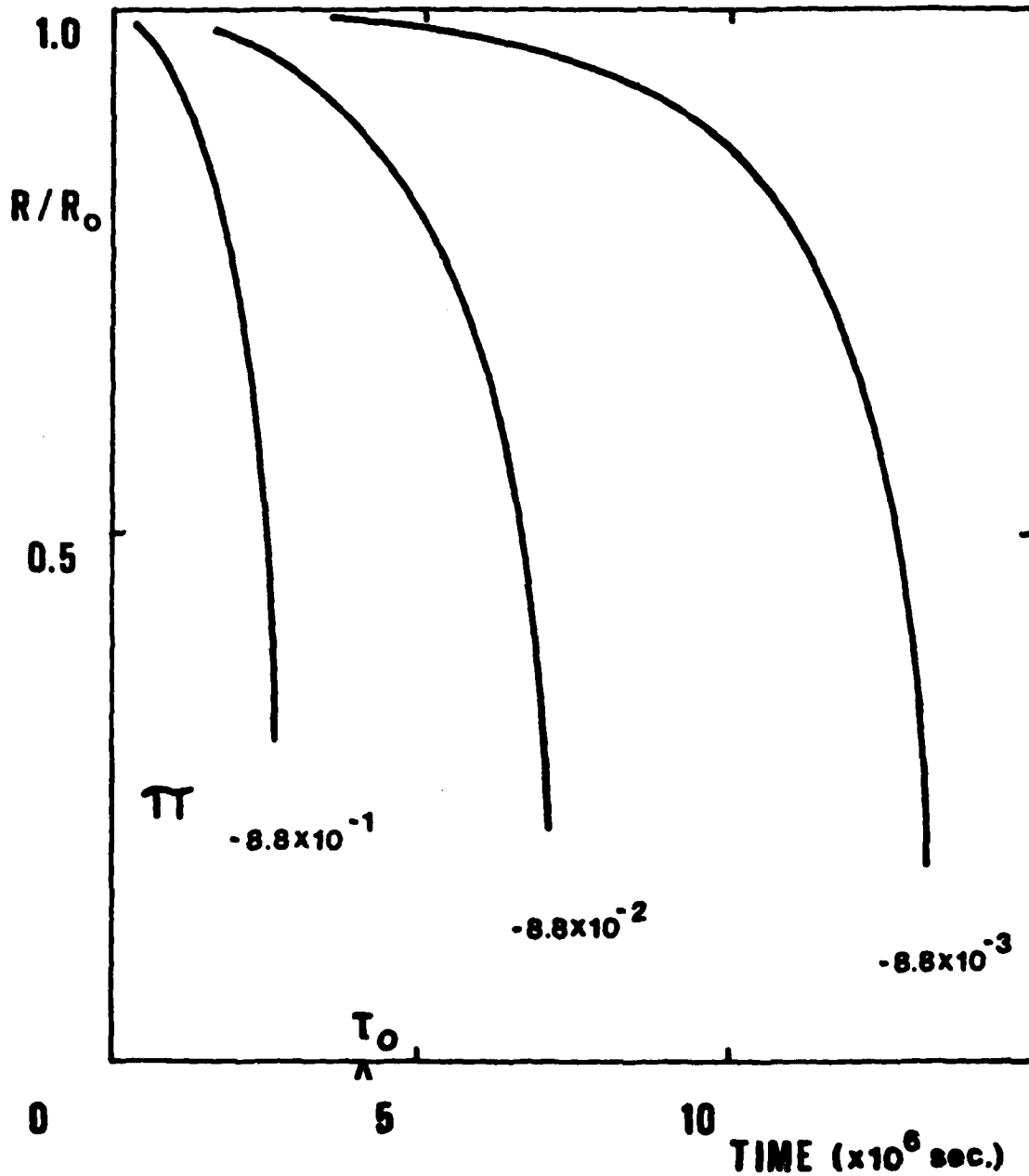


Figure 15. Spherical Radius vs. Time - Theoretical Collapse

$R_0 = 1.03 \times 10^{-3}$ cm.
(see Table 3)

2. Model Nonspherical Dynamics without External Flow

The initiation scheme of Section IV, with quiescent ambient conditions, requires only a choice of a particular harmonic, n , and $a_n(0)$ and $\dot{a}_n(0)$ beyond the parameters of spherical flow. The problem which allows the mathematically consistent use of an initial $T(r,0)$ function which is identically zero is $a_n(0) = a_0$ and $\dot{a}_n(0) = 0$ from equation (III.32).

For $\pi = 0$, a bubble of constant radius, R_0 , the nonlinear nature of the governing equations is removed and Laplace transform techniques have been used by other workers to generate $a_2(t)$ vs τ profiles. The integro-differential character of the system is also removed for a purely viscous fluid and physically, the viscosity is expected to damp any oscillations. This expectation is confirmed in Figure 16 where a 30-fold increase in viscosity is shown to damp the asymmetries greatly.

Since viscoelasticity restores the time-integration terms to the model, the possibility of somewhat different behavior exists even for $\pi = 0$. However, as discussed previously, the absence of bubble history to initiate these time-integrals at some non-zero value, in conjunction with the short times over which the non-sphericities persist (10^{-5} seconds), serves to allow little "elastic accumulation" and results in viscoelastic behavior which differ little from those which would occur with a slight change in viscosity. This is shown in Figure 17. However, the fine details of the difference cannot be reproduced by a simple change in viscosity. When an elastic element is introduced, the damping of the resulting amplitude wave decreases, which would occur if viscosity decreased, but the period of the oscillation increases

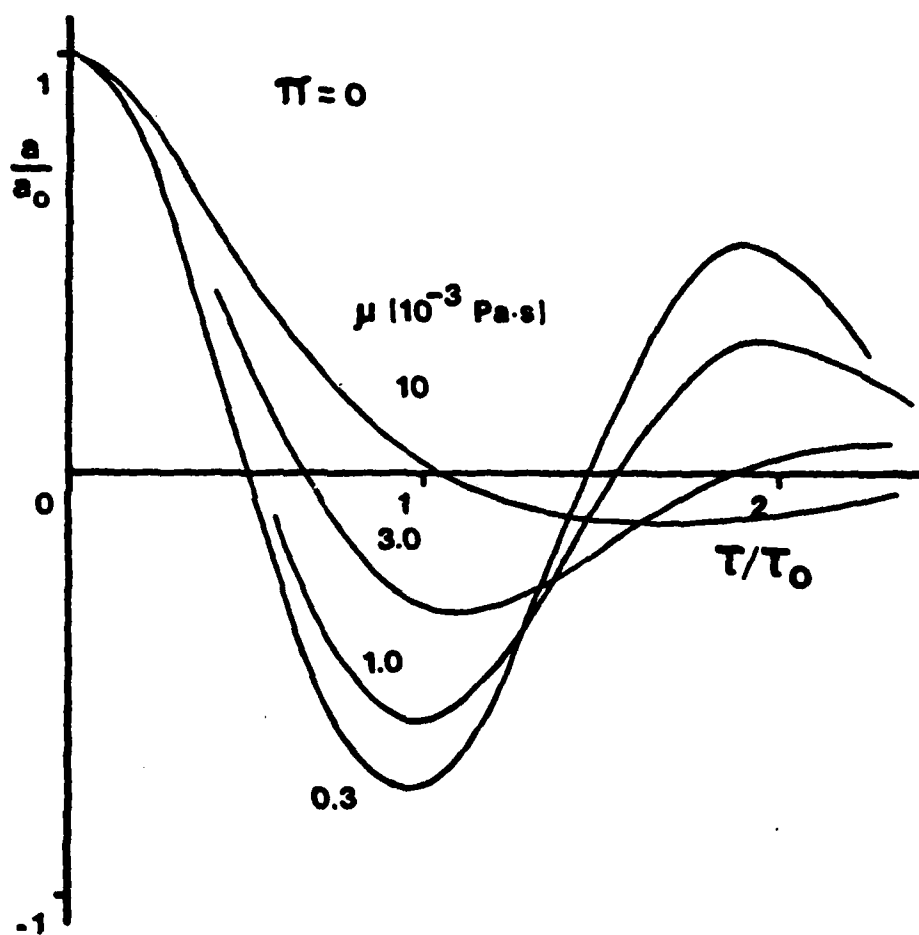


Figure 16. Nonspherical Amplitude vs. Time -
Viscosity

No external flow
 $a_0 = 0$
 (see Table 3)

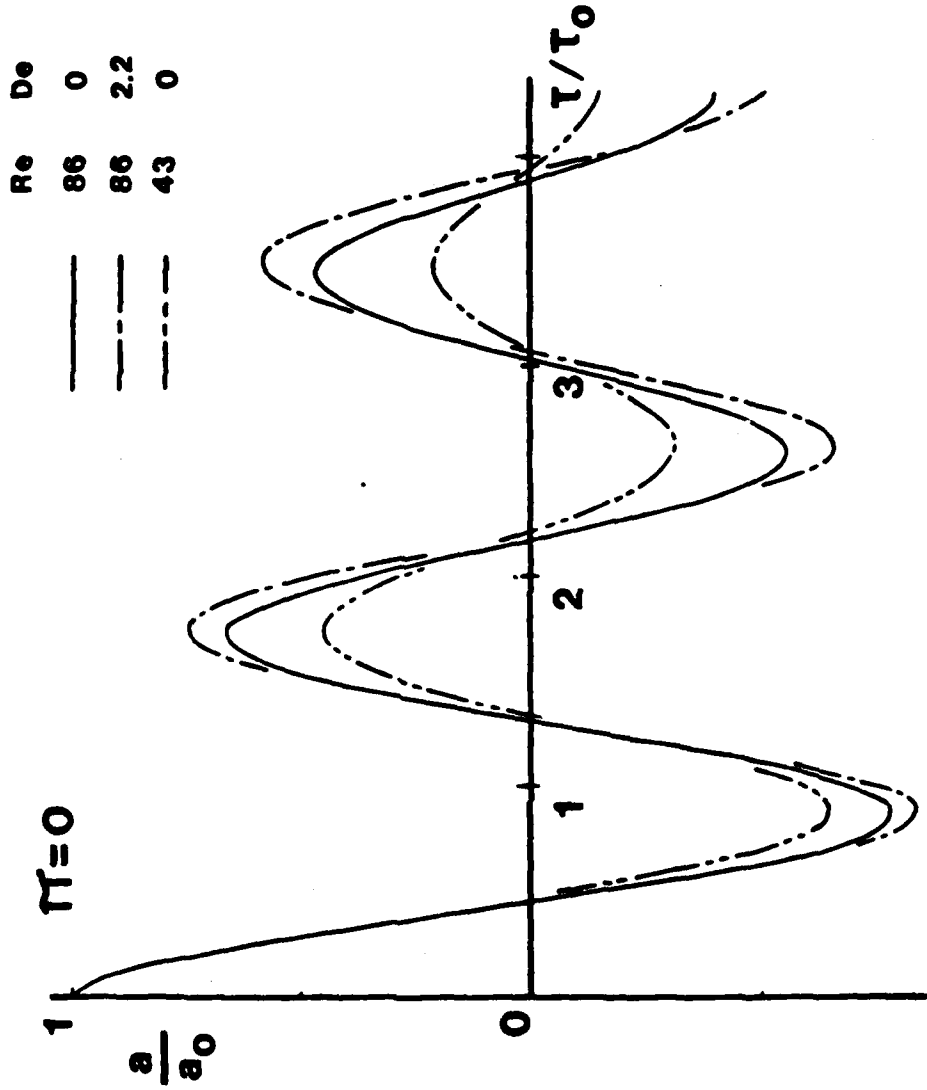


Figure 17. Nonspherical Amplitude vs. Time - Viscoelasticity

No external flow
 $\dot{a}_0 = 0$ (see Table 3)

which would result for a more viscous fluid. These results agree with those of Inge and Bark (1981) who generated results using techniques suitable only to $\dot{R}(t) = 0$.

Cases of more interest involve non-zero dimensionless pressure change, π , values. Stability analyses predict that bubble growth will restrict the viscous nonsphericities causing the bubble to remain nearly spherical. Typical results presented in Figure 18 show this to be true for the viscous fluid which has nonsphericities which become overdamped. However, the viscoelastic fluid in Figure 18 exhibits somewhat different behavior. here, as $\dot{R}(t)$ becomes almost constant, the shape of the bubble, as measured by $a_2(t)/R(t)$ also appears to approach a constant.

Earlier stability analyses suggest that conditions which include bubble collapse may result in nonsphericities which grow without bound. Figures 19 and 20 show typical profiles which confirm this prediction. Good numerical convergence was achieved even for such large amplitude values. If the linearized system remains valid such bubbles would exhibit breakup or toroidal ring formation and this mechanism for the dissipation of inertial and surface energy requires consideration. Experimental trials are necessary to determine if these predictions are even qualitatively correct.

3. Experiments with No External Flow

The initial trials with the experimental apparatus were to guarantee the ability of the system to generate bubbles, first in water and then in polymer solution, and of the photographic system to capture images of those cavities. The first successful trials resulted in photos, typical samples of which are shown in Figure 21. Note that these bubbles are quite large, with a radius greater than 0.50 cm at

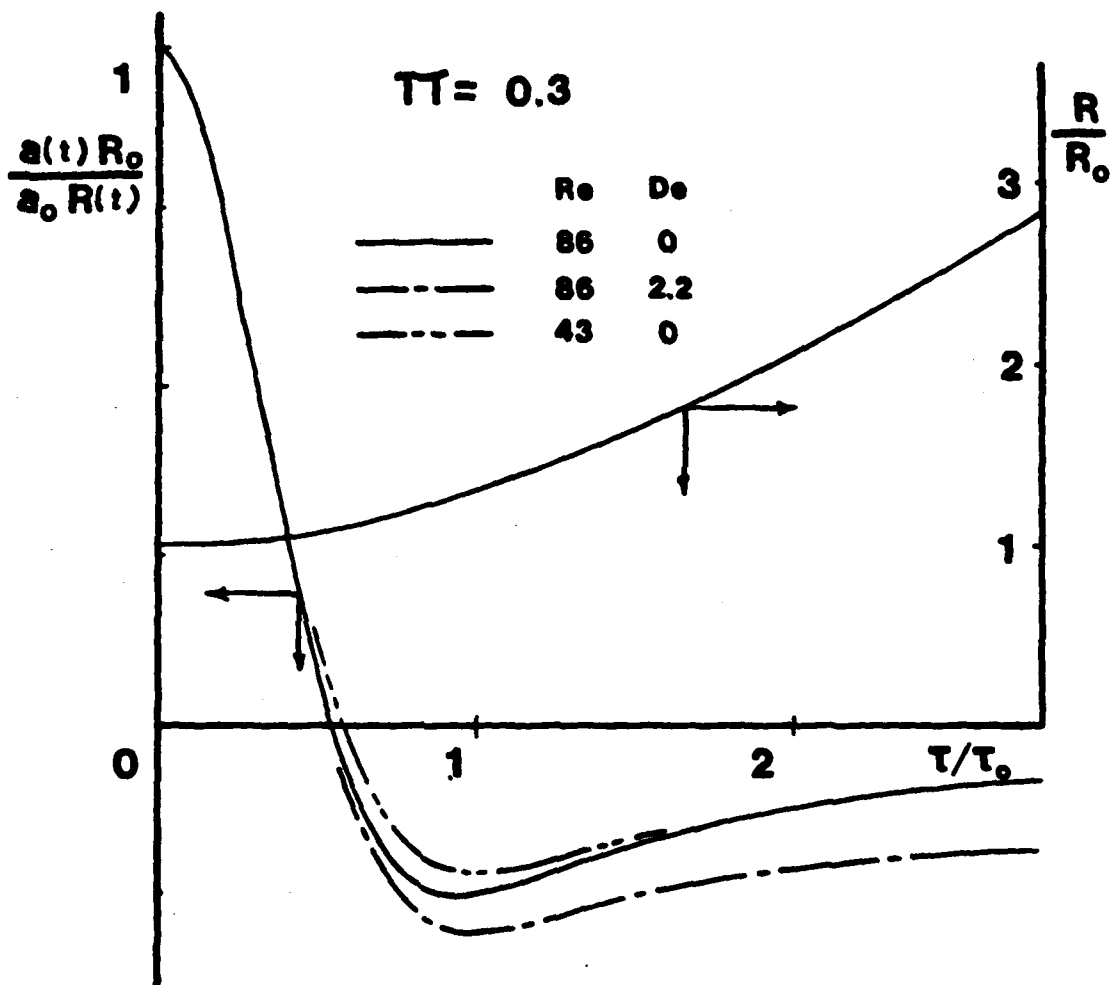


Figure 18. Normalized Amplitude vs. Time - Growth

No external flow
 $\dot{a}_0 = 0$
 Growth profile shown
 (see Table 3)

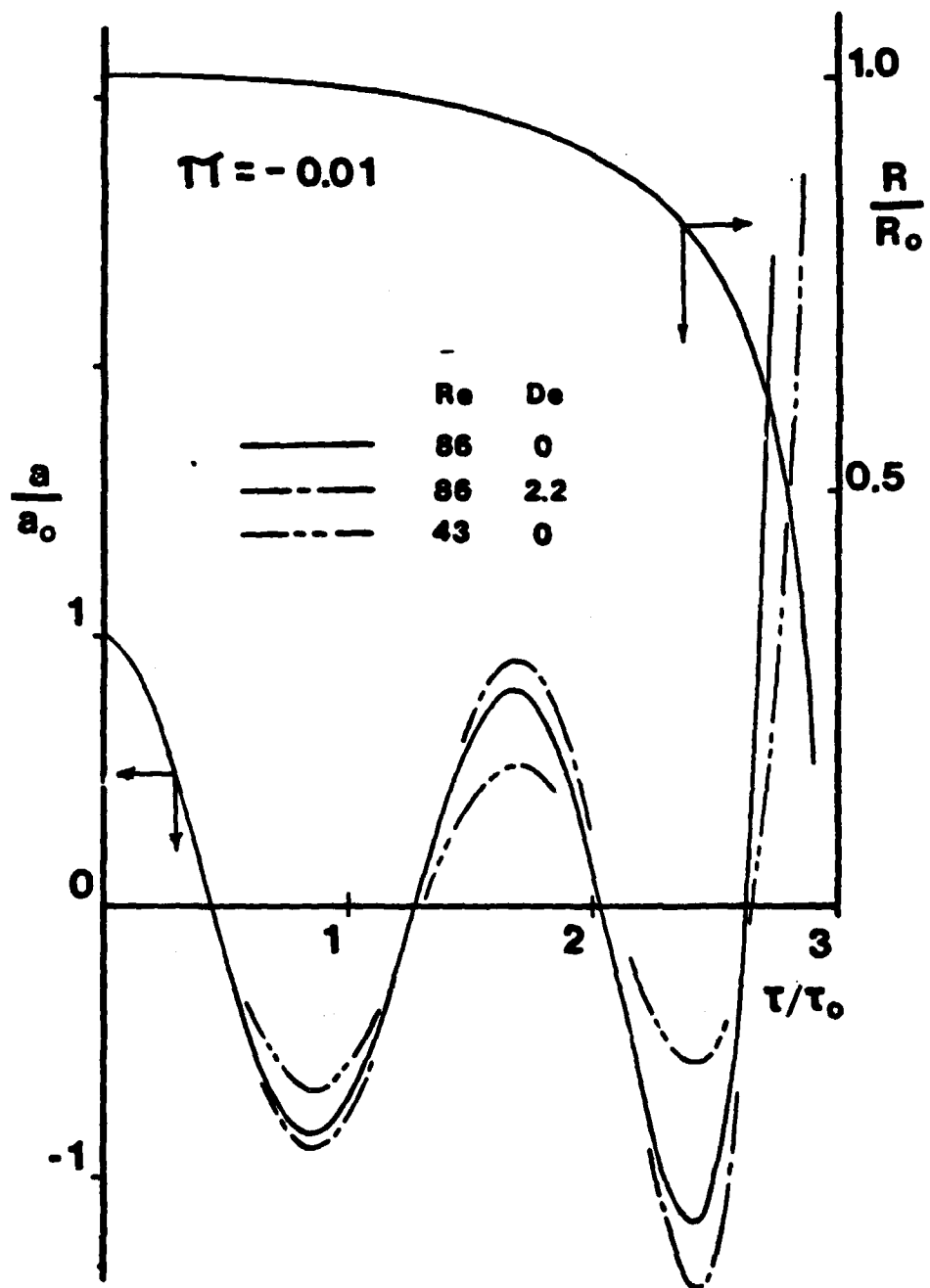


Figure 19. Nonspherical Amplitude vs. Time-Collapse I

No external flow

$a_0 = 0$

Collapse shown

(see Table 3)

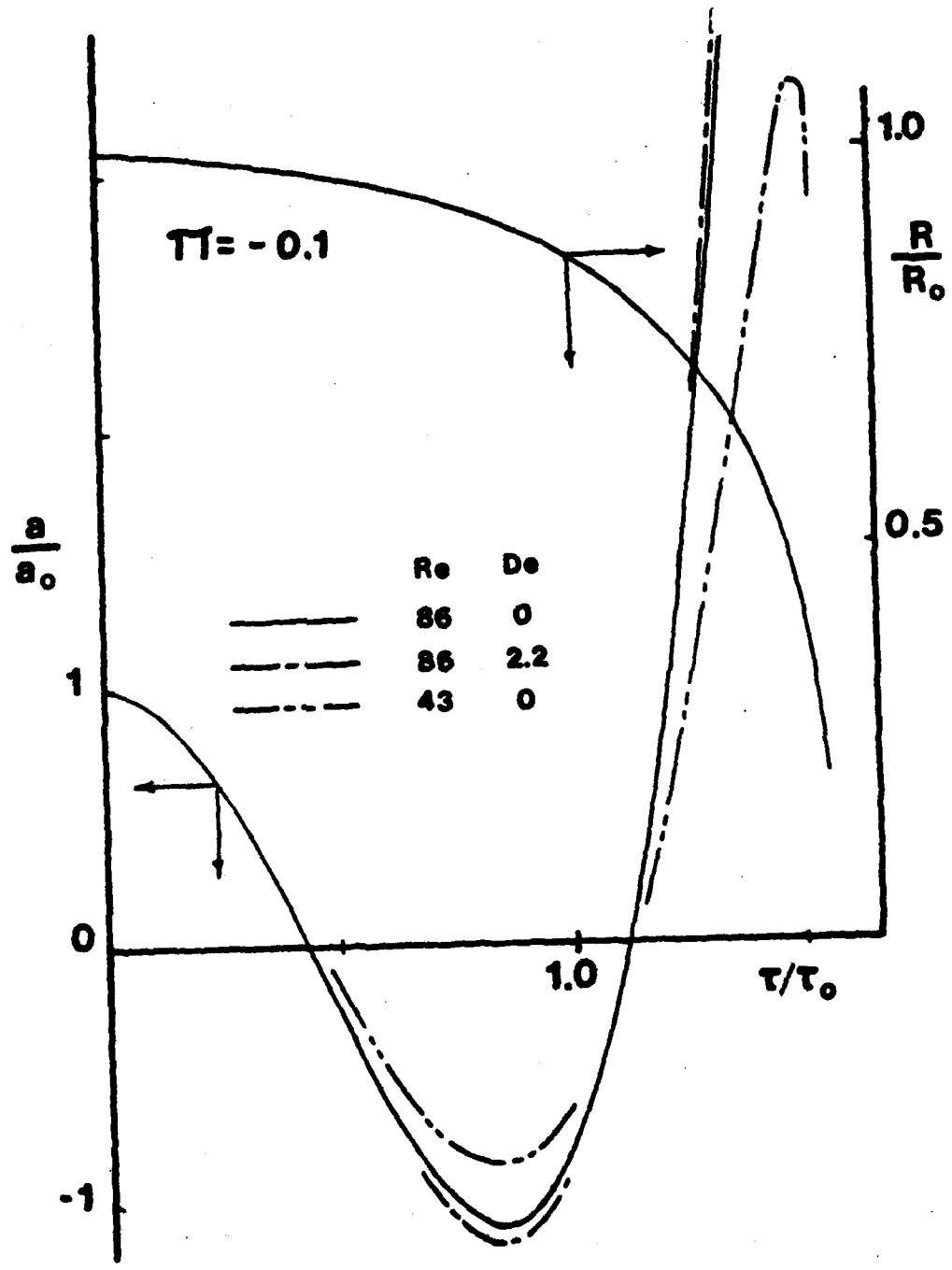


Figure 20. Nonspherical Amplitude vs. Time - Collapse II

No external flow
 $A_0 = 0$
Collapse profile shown
(see Table 3)

1,050 usec. They are created with center in approximately 1.50 cm from the closest asymmetry. The solid "wall" of the planar face of the plexiglas lens influences the bubble in all dynamic cycles other than initial growth. The reproducibility of these bubbles is excellent with a superimposition of the images usually possible even including some of the fine structure of the bubble. There are occasional "glices", bubbles which do not reproduce trials for identical conditions, these appear to have a number of possible causes:

A) Lack of laser reproducibility. A qualitative indicator of the laser pulse characteristics can be obtained by looking at the bright flash at the original bubble center which is the overexposure of the photo plate caused by the laser luminescence. Although these trials have been selected for their reproducibility, some of the variation possible is indicated by a comparison of the spot in the frame at 525 usec and that at 1570 usec. The latter event shows a secondary brightness separated from the main. Such differences usually correlated well with unexpected differences in the cavities.

B) Overly Rapid Repetition of Trials. Early in testing it became apparent that reproducibility suffered when an experiment was repeated as quickly as possible, limited only by the charging cycle of the laser capacitors which requires 5-10 seconds. The lack of reproducibility was particularly evident with conditions and at times which showed nonspherical bubbles. At such times waves were also sometimes noted on the free surface of the fluid indicating that the fluid motions induced by the first bubble were not completely damped. It was found that an interval of 60 seconds between trials was more than sufficient to eliminate this effect.

A puzzling feature of the photographic sequences is the recording of no bubble image for time delays of 500 μ sec or less. Initial hypotheses of a bubble induction time proved to be unfounded. The delay is caused by a lag between digital delay triggering and the laser firing signal in the circuitry of the laser power supply.

A. Spherical Bubbles

Spherical sequences were generated with a criterion for reproducibility based on the measured radius between two trials varying by 5% or less. The viability of the technique is demonstrated in Figure 22 which shows data for spherical radius vs. time in distilled H₂O and 476 ppm polyacrylamide solutions. Conditions used were

medium lens $\rightarrow f_H = 1.5$ cm.

medium neutral density filter

80% laser charge

Each of the polyacrylamide data bars represent the mean of at least three trials bounded by the resulting standard deviation. Reproducibility is excellent, especially considering the high growth and collapse values produced. The slightly higher collapse rate for water may result from difference in laser interactions with the two fluids. The order of magnitude analysis of Table 2 suggests that a small part of the difference may be rheological, since they occur in the region of low velocity where inertia is smallest. This would be eliminated in smaller bubbles where surface tension becomes even more important, however the size here is the minimum for the single shot technique where ± 10 μ sec emerges as a limit on reproducibility.

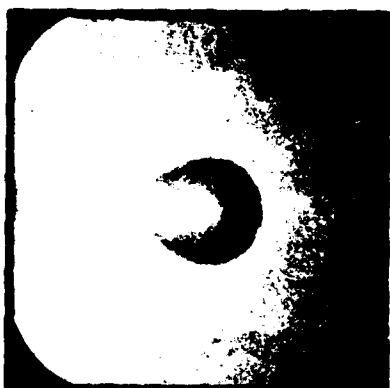
**a. 525****b. 1050****c. 1550****d. 1570****e. 2000****f. 2500**

Figure 21: Bubble Sequence in Water
(μ sec., 4x)

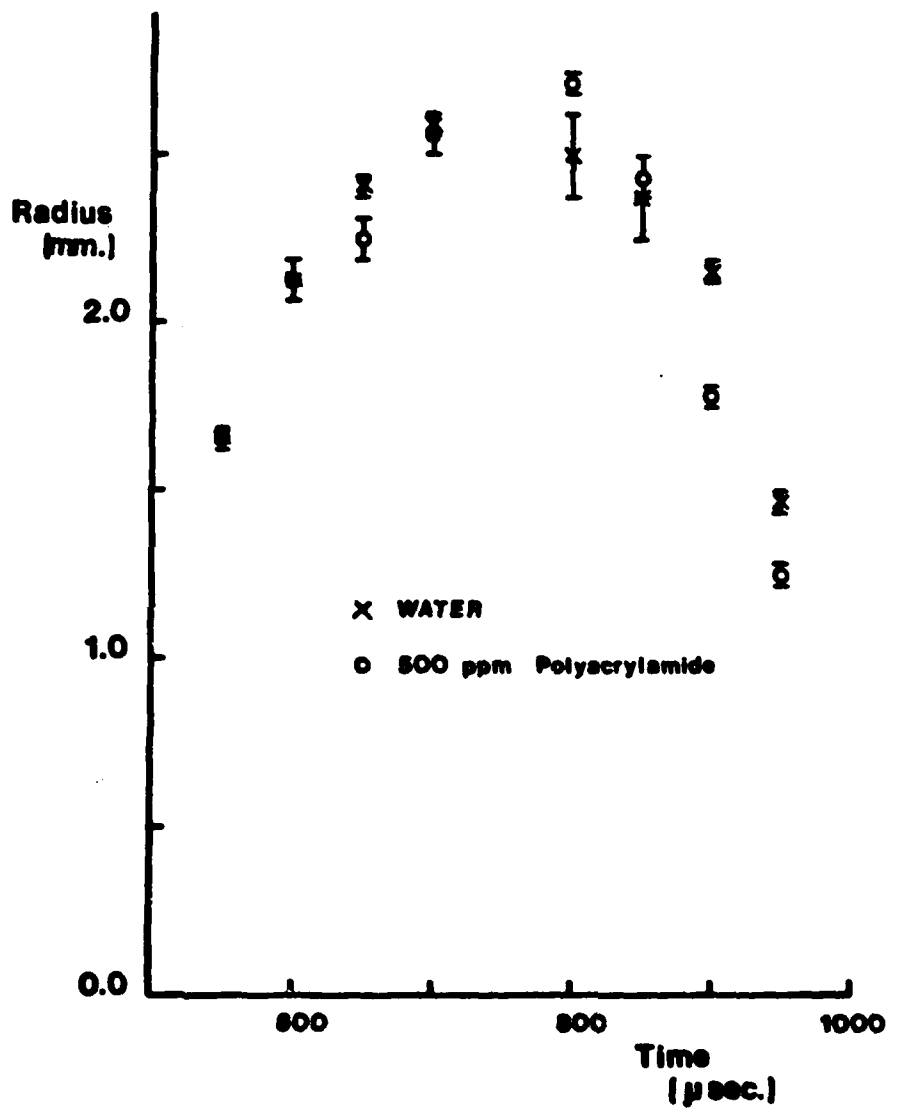


Figure 22. Experimental Spherical Radius vs. Time Data

Laser: 80.0%, medium filter
Single, medium lens

AD-A129 130

EFFECTS OF FLOW AND NON-NEWTONIAN FLUIDS' ON
NONSPHERICAL CAVITATION BUBBLES(U) PRINCETON UNIV NJ
DEPT OF CHEMICAL ENGINEERING W R SCHOWALTER ET AL.
10 APR 83 N00014-79-C-0385 F/G 20/4

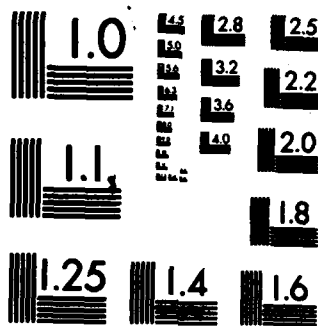
2/2

UNCLASSIFIED

NL

0000
0000

END
DATE
FILMED
DTIC



MICROCOPY RESOLUTION TEST CHART
NATIONAL BUREAU OF STANDARDS-1963-A

B. Spherical Bubbles near Solid Walls

Although no theory has been developed here to include the influence of solid walls or free surfaces on the evaluation of bubble shape, qualitative results were of interest to confirm the findings of previous workers and also to allow comparison with future trials which would include initially nonspherical bubbles near the planar surface. The present photos confirm earlier findings that a solid wall induces bulk motion of the bubble toward the wall and subsequent jet formation as collapse proceeds, no visible difference appeared in the jets in the different fluids (see Figure 23).

C. Nonspherical Bubbles

The scheme by which nonspherical bubbles can be produced in an otherwise quiescent fluid was described earlier. This possibility has been mentioned by Lauterborn and Ebeling (1977), but no quantitative results exist or any assurances of reproducibility. The problem of laser "spot" reproducibility mentioned earlier with regard to spherical bubbles is even more crucial here since the distribution of laser energy along a line segment is needed to create a disturbance of small bubbles which grow and merge into one nonspherical cavity.

Initial trials were encouraging since nonspherical bubbles were seen to be feasible but they suffered from an extreme degree of randomness in the particular distribution of initial nucleatic sites and their strength. The line of cylinder which bounded the nucleation region was well defined but the distribution of bubble formation within the region was sporadic which caused reproducibility to suffer. More power was necessary to create reproducible bubbles due to the increased

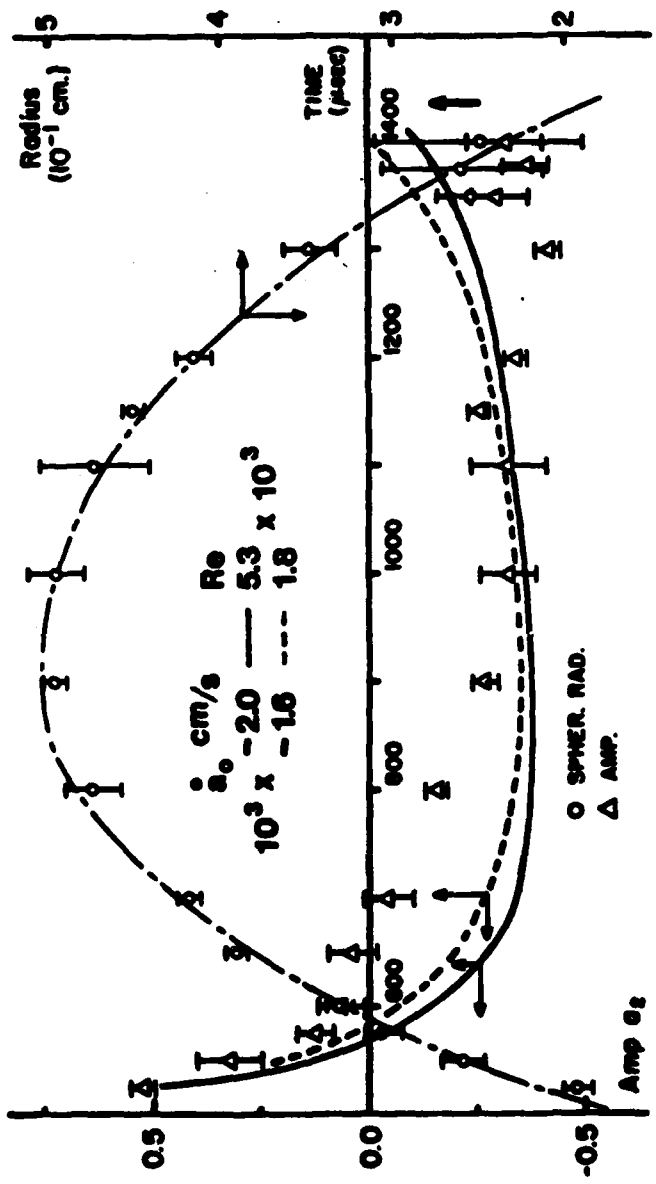


Figure 24. Comparison of Experimentally Determined Nonspherical Amplitudes to Theoretically Generated Curves I

Experiment - distilled water
 Laser: 97%, no filter
 Lens separation: 6 cm.
 Theory - $a_0 = 5.20 \times 10^{-1}$ cm.

length of the optical path in the fluid (4-6 cm) which served to absorb and scatter some light energy and to the intentionally lengthened region in which sufficient energy concentration was desired.

This power requirement resulted in narrow range of power in which nonspherical bubbles could be generated. The lower bound was determined by the factor just cited and corresponded to the low density filter and 85% charge. The energy of this pulse is nominally 1.0 J. The maximum is restricted by the laser, 1.5 J. This range is considerably narrower than the corresponding one for spherical bubbles which could be produced by .50 J and less. The resulting variability in nonspherical bubble size was small with maximum equivalent radius between .3 and .6 cm., but those which could be generated were clear and reproducible.

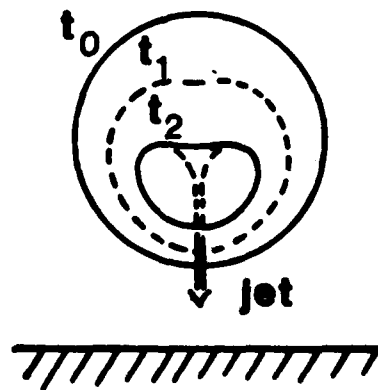
Complete sequences were generated and analyzed for distilled water at two power settings and two polyacrylamide solutions near 500 ppm. The bubble shape and size were analyzed (see Appendix D) and the results are shown in Figures 24-27. As discussed in Appendix D.1, no best fitting procedure could be established, all gave comparable results, so that the simplest, measuring major and minor axes and assuming a shape conforming to the second harmonic was used. Thus, the error bars in the experimental data result from three sources:

- 1) reproducibility of bubbles
- 2) photo image measurement
- 3) uncertainty in fit.

The relative importance of these factors varied from image to image



**Figure 23: Initially Spherical
Bubble Collapsing near a
Solid Wall - Impinging
Jet Formation**



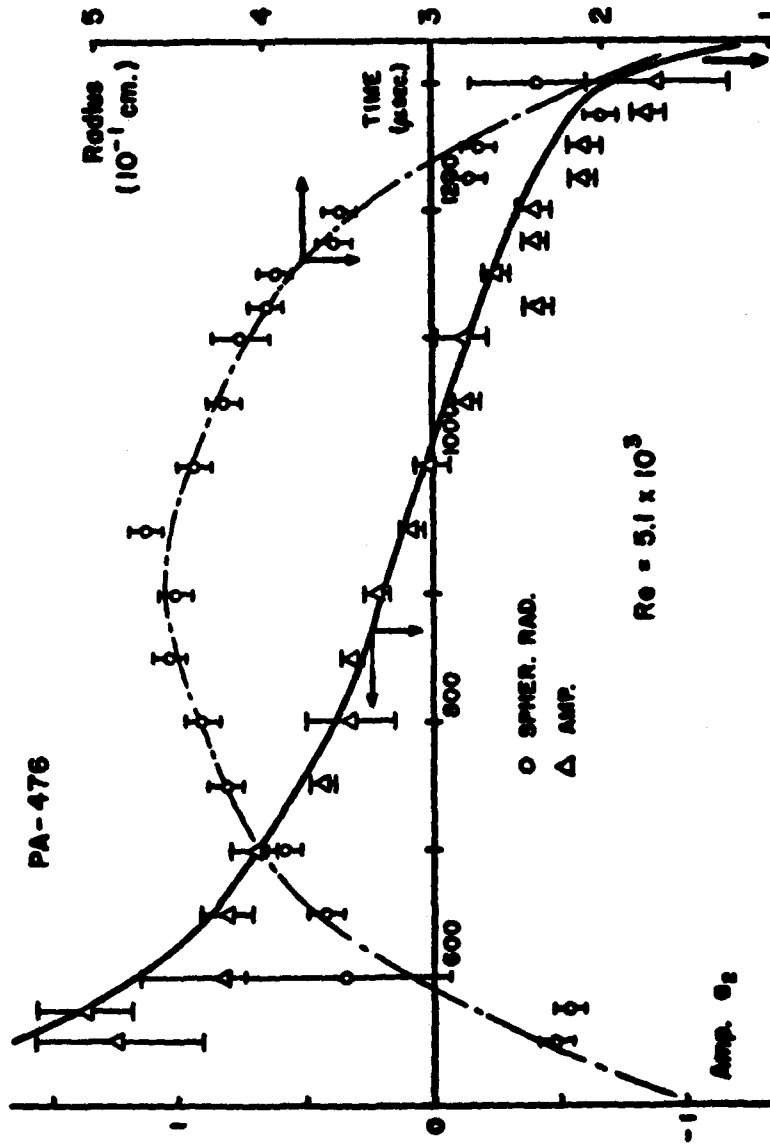


Figure 25. Comparison of Experimentally Determined Nonspherical Amplitudes to Theoretically Generated Values II

Experiment - Laser: 95%, no filter Theory - $\dot{a}_0 = 1.25 \times 10^{-1}$ cm.
 Lens separation: 3 cm. $\dot{a}_0 = -1.50 \times 10^3$ cm./sec.

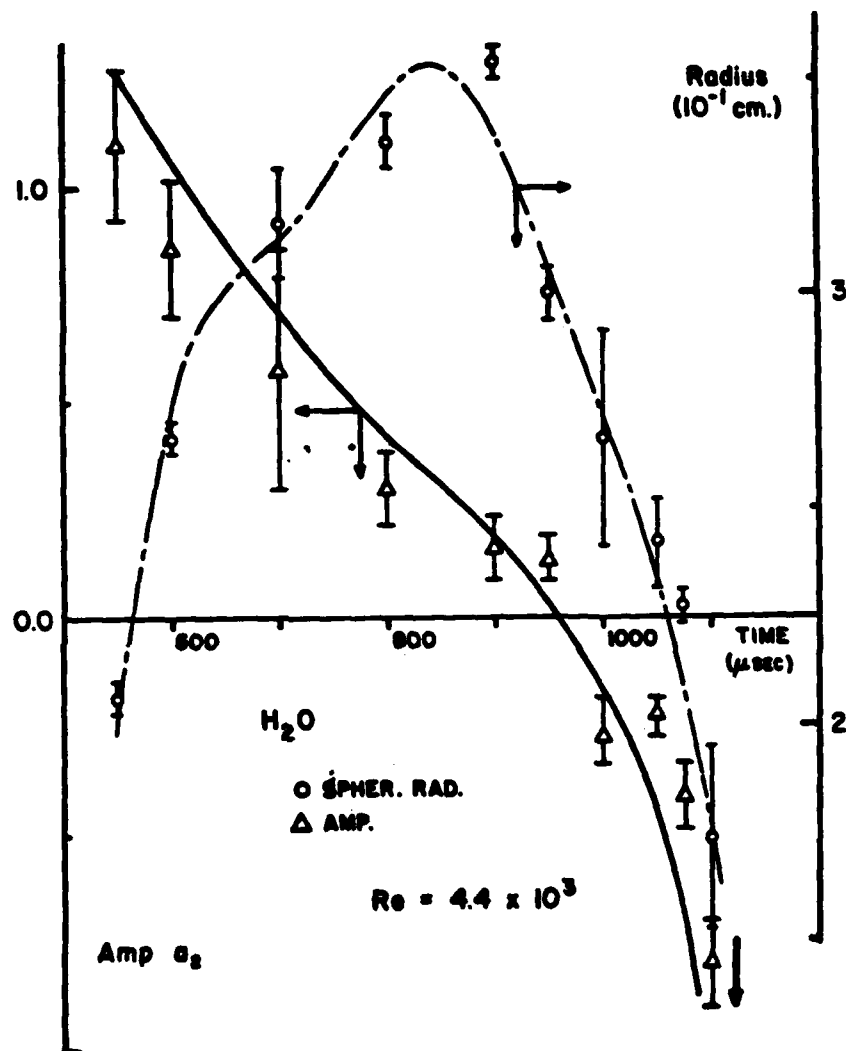


Figure 26. Comparison of Experimentally Determined Non-spherical Amplitudes to Theoretically Generated Values III

Experiment - Laser: 87.5%, low filter
Lens separation: 4.5 cm.

Theory - $a_0 = 1.27 \times 10^{-1}$ cm.
 $\dot{a}_0 = -4.0 \times 10$ cm./sec.

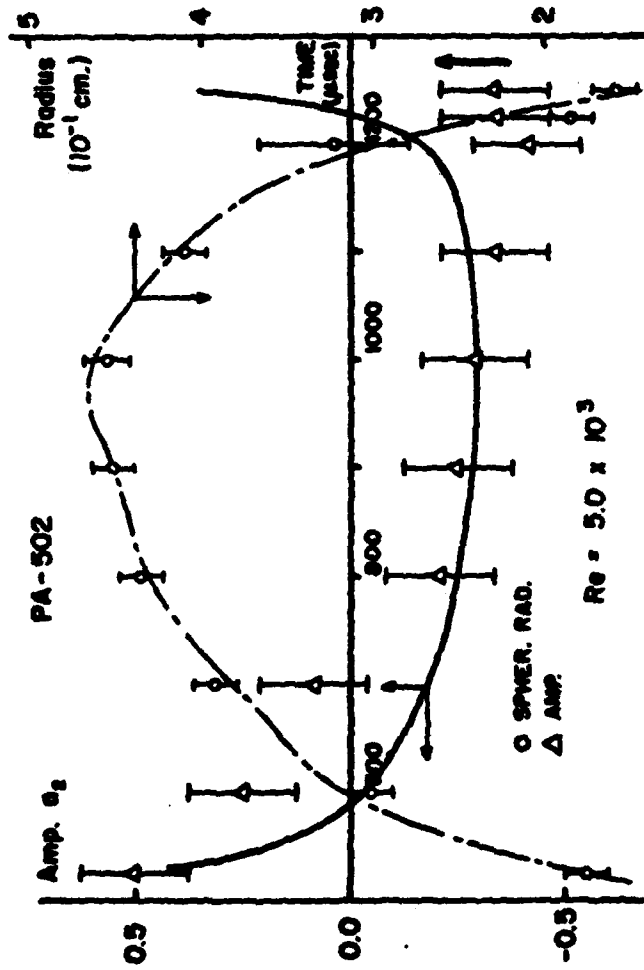


Figure 27. Comparison of Experimentally Determined Nonspherical Amplitudes to Theoretically Generated Values IV

Experiment - Laser: 97%, no filter Theory - $\alpha_0 = 5.0 \times 10^{-1}$ cm.
 Lens separation: 6 cm. $\beta_0 = -3.0 \times 10^3$ cm./sec.

within a sequence, although factor 2) was usually least important. Despite these uncertainties a smooth progression of shape was the result.

The $R(t)$ vs. t profile was smoothed by a best fit to a Fourier series when initial time, period and the contribution and eigenvalue of up to five eigenfunctions were varied. These fits are shown as the "center-line" dotted curve in Figures 24-27. This fit was then differentiated twice for use as the forcing function in the solution of the nonspherical amplitude equations. The changes in sign of the radial acceleration $\ddot{R}(t)$ in the fit profile, corresponding to inflections in the curves, occur because of the fitting procedure and the varying number of data points taken at different times. Despite the resulting physically unrealistic values, the nonspherical amplitude profiles driven by the fit are well-behaved. The curves are smooth because the inflections occur while the bubble is growing, a period during which nonsphericities are stable and relatively insensitive to the details of the radius profile.

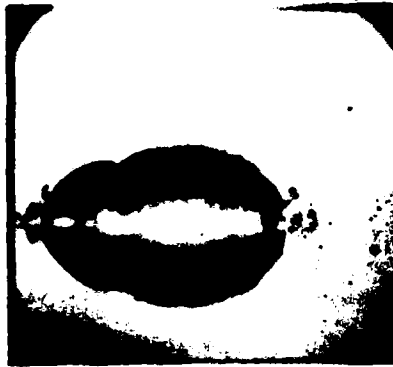
The initiation of the model required an initial time t_0 at which the amplitude $a(t_0)$ had been measured. This time, t_0 , was chosen, before any data-specific modelling was done, by taking it as the time of the first data point. The first data point corresponds to the first bubble photo in a time sequence which appears as one, relatively smooth, cavity and usually occurred by 550 μsec or 50 μsec after any bubble is visible. Since there was no external flow and motion was present for less than 50 μsec previous to t_0 , bubble-induced fluid history was ignored; the stress integrals begin with zero value. Variation of $\dot{a}(t_0)$ and fluid parameters was then performed to optimize the agreement with experimental data.

Setting $\dot{a}(t_0)$ to various values and varying fluid parameters showed that viscoelastic effects were small as would be expected from previous model runs for situations without external flow and with

zero stress integrals. Thus there are two important degrees of freedom, the initial velocity $\dot{a}(t_0)$ and the viscosity μ . The absence of viscoelastic effects also reduces the sensitivity of the agreement to the initial time t_0 . Changing t_0 will not alter the model predictions for a given μ and corresponding initial conditions, it can only change the number of data points to be fit and here that number is already maximized.

The viscosity (or Reynolds Number) values which gave the good agreement shown by the solid lines were lower (or higher) than expected for water. They were between 0.1 and 0.3 cp. Setting the viscosity to 1.0 cp without altering the initial velocity resulted in predictions of overdamped oscillations during bubble growth; the amplitude $a_2(t)$ did not cross the $a_2 = 0$ axis while radial velocities were positive. Increasing the magnitude of the initial velocity $\dot{a}(t_0)$ and the viscosity did serve to drive the amplitude past spherical equilibrium, but the shape was altered, see Figure 24, and fit was less good.

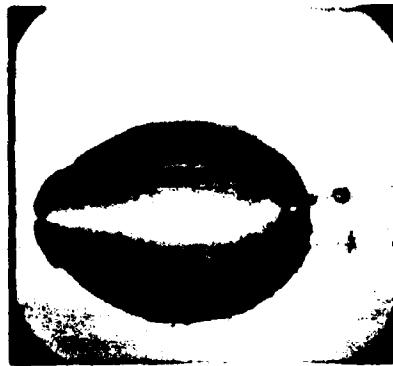
The most encouraging aspect of the model results may be the accurate predictions of trends even when deformations become large so that the linearized analysis should break down. In both water and solution, the final frames of a sequence, as the bubble volume became very small, could show one of two distinctly different "asymptotic" behaviors. One type is suggested by the upper left-hand illustration in Figure 9; the nonspherical amplitude is positive and becomes large as R decreases so that the cavity is extended in a line along the axis of symmetry. The other extreme occurs for negative amplitudes and gives the forms shown in the lower right of Figure 9. In experimental photos this appears as an image like Figure 28(a) and becomes a vertical line as $R \rightarrow 0$. Such shapes are too distorted from the sphere to be represented by an equivalent radius R and amplitude a_2 , and predicted by this theory. Still, the model successfully predicts these final trends which is

Figure 28: Nonspherical Sequence in Water

a.
600



e.
1000



b.
700



f.
1100



c.
800



g.
1200



d.
900



h.
1300

(no - $\mu\text{sec.}$, 4x)

extremely useful for the study of bubble breakup.

D. Nonspherical Bubbles Near Solid Walls

The premise upon which this work is based is that the role of velocity fields in cavitation dynamics extends beyond the creation of the dynamic pressure difference necessary for nucleation, that it alters the shape and the size, i.e. the total behavior, of the subsequent cavity. Another factor of practical importance in this behavior has been shown, both here and elsewhere, to be the proximity of a solid wall, but this effect has only been investigated for initially spherical bubbles. Trials were conducted to investigate any interplay between nonspherical bubbles and solid walls. They are complicated considerably by the introduction of a direction vector for the bubble, which can simply be chosen as along the initial axis of symmetry for these bubbles, and it can vary in orientation with respect to the solid wall which can be represented by a normal vector. Quantitative comparison to results for spherical bubbles without detailed theory is ambiguous. The distance of the initial center of the bubble from the solid wall scaled on a maximum bubble radius gives a good variable with which to correlate results (Chahine, 1981) for a spherical bubble. However for asymmetrical bubbles, the amplitude of any initial nonsphericity along with the orientation of the direction vectors will introduce much more variability into the system even for identical fluids.

As a result of these complications, only qualitative results were sought in these exploratory experiments. Comparisons between H₂O and polymer solutions were also made.

Photographic evidence from these trials lead to two tentative conclusions:

1) A strong competition does exist between the jet-forming effect of a solid wall and nonsphericities which are separate from that effect and it varies with orientation.

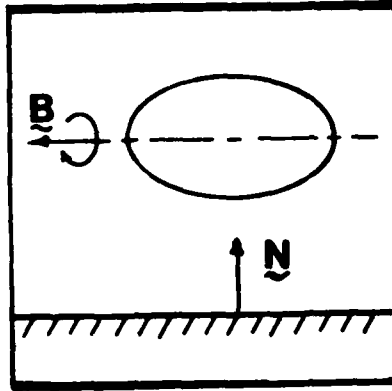
2) No large differences between fluids occur.

This first conclusion is supported by the photo sequences of Figures 30 and 31 which show no images of a well-formed jet like the one in Figure 23. Figure 23 differs from Figure 30 and 31 in that the initial optical cavity in the former was spherical while intentionally nonspherical bubbles were initiated in the latter. Figures 30 and 31 are representative of images taken over a range of bubble sizes and wall proximities. All showed bubble migration toward the wall upon collapse, but none showed an impinging jet. Figure 30 shows the results when \underline{B} and \underline{N} are perpendicular (see Figure 28(a)).

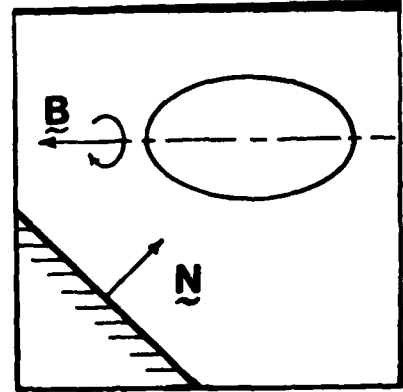
When \underline{B} and \underline{N} form a 45° angle more experimental problems develop since a bubble which is too highly nonspherical initially, and close to the wall will contact it. Thus the location of bubble center is more limited than for the previous cases. Here, again the solid wall causes bubble migration toward it with distortion but no jet is apparent (see Figure 31).

Trials with other orientation angles, wall-bubble distances and 500 ppm polyacrylamide solutions yielded similar results. Of course, such trials are not comprehensive, especially since the nonspherical bubbles are very limited in their size and shape profiles. However the contrast in the case of jet formation for spherical bubbles and the absence thereof for asymmetrical bodies is striking.

Figure 29: Bubble - Wall Orientation

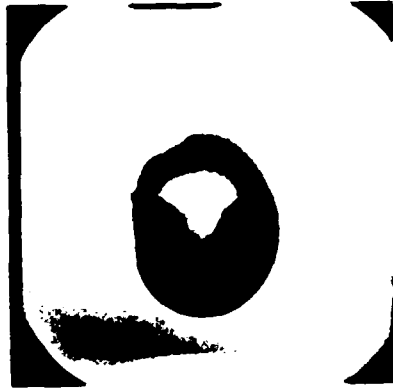


a. B \perp N

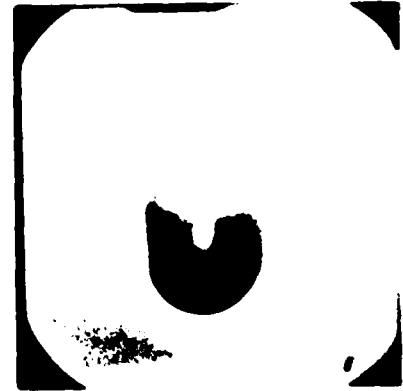


b. B 45° N

Figure 30: Sequence - B \perp N [μ sec., 4x]



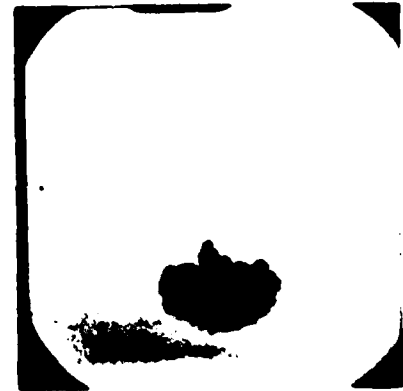
a. 1350



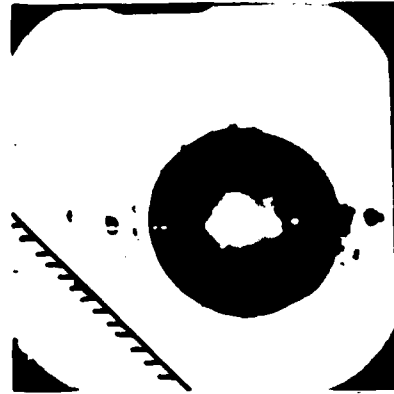
b. 1375



c. 1400



d. 1425



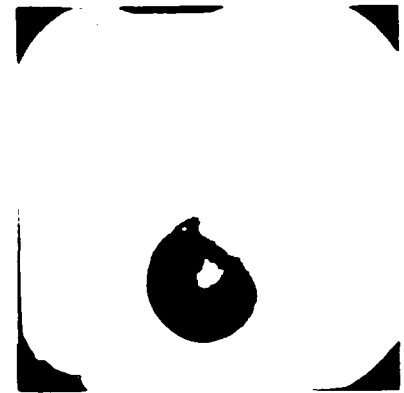
a. 600



b. 1000



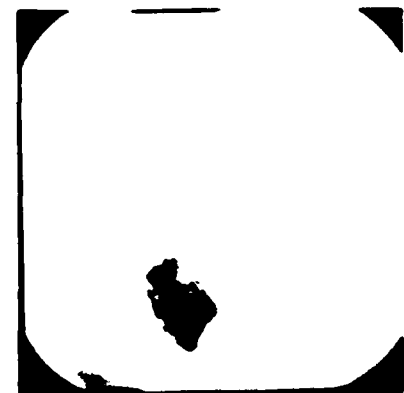
c. 1400



d. 1450



e. 1475



f. 1500

Figure 31: Sequence - B & N at 45°

(μ sec., 4x)

4. Model with External Flow

Recall the model which generates a completely self-consistent fluid history by postulating an external flow. The details are developed in Section IV and summarized here and in Figure 32. In the semi-infinite time domain with upper bound time $t = \tau = 0$, the equations governing asymmetric dynamics can be driven by a mathematical forcing function which corresponds to an externally imposed flow in the physical realm. Mathematically, any such forcing function can be linearly decomposed into terms with time dependencies of the form

$$\theta_{r,j}(t) = \theta_j(t) = \exp\left[\left(\frac{1}{\xi_j} \pm i\omega_j\right)t\right], \quad t \leq 0 \quad (\text{IV.18})$$

Since this forcing function is bounded throughout the interval $[-\infty, 0]$, the time constant ξ_j is positive (and real). When specific values of ξ_j and the frequency ω_j are chosen, they completely determine the forced response of the fluid for a given angular mode n and fluid model. The stresses in the fluid and shape of the bubble are also determined. The terms remaining in the resulting flow field as $r \rightarrow \infty$ are

$$\begin{aligned} \mathbf{y}_1^\infty &= \text{Re} \sum_n \sum_j A_{n,j} \theta_{n,j}(t) \nabla [r^n Y_n^m(\theta, \phi)] \\ &= \text{Re} \sum_n \sum_j A_{n,j}(t) \nabla [r^n Y_n^m(\theta, \phi)] \end{aligned} \quad (\text{IV.24})$$

where $A_{n,j} = A_n$ is a complex constant and $A_{n,j}(t) = A_n(t)$ is a complex function of time. For $n = 2$, as shown in Equation (IV.25) and Figures 6, 8 and 10, this spatial variation corresponds to two and three-dimensional extensional flows with time-dependent elongation rates

$t = \tau < 0$	TIME $t = \tau = 0$	$t = \tau > 0$
NO EXTERNAL FLOW		
$\underline{v} = 0$ Quiescent Fluid $R = R_0$ $\dot{R} = 0$	Specify: $a(0) = a_0$ $\dot{a}(0) = \dot{a}_0$ [all other quantities] = 0	$\underline{v} \rightarrow 0$ as $r \rightarrow \infty$ $R = R(\tau)$
WITH EXTERNAL FLOW		
$R = R_0$ $\dot{R} = 0$ As $r \rightarrow \infty$ $\underline{v} \rightarrow$ $\{A_2 \exp(t/\zeta) \sin(\omega t)\}$ $\underline{v}[r^2 Y_2^m(\theta, \phi)]$	i) Flow has generated all asymmetries. ii) Flow continues with same frequency for all times. iii) Changes in R initiated at $t = \tau = 0$.	$R = R(\tau)$ As $r \rightarrow \infty$ $\underline{v} \rightarrow$ $\{A_2 \exp(-\tau/T_{decay}) \sin(\omega \tau)\}$ $\underline{v}[r^2 Y_2^m(\theta, \phi)]$

Figure 32. Comparison of Flow and No Flow Condition.

Expressions shown for $n = 2$, but corresponding conditions exist for all $n \geq 2$.

directly proportional to $A_n(t)$.

At time zero the external flow has generated nonsphericities in the bubble of radius R_0 and the added complication of a time dependent equivalent radius, $R(t)$, can be introduced. (See Figure 32.) The particular solution obtained by the separation technique of Section IV no longer applies when R changes so that the full, numerical, procedure of Appendix C must be utilized. Within this procedure the external flow is no longer constrained to the time dependence of expression (IV.18). To investigate the influence of a further alteration of the flow, the amplitude of the oscillation is allowed to decrease with time, but the frequency ω was retained. This amplitude variation is characterized by a time constant, T_{decay} . Various mathematical forms of the decay function were tried, e.g. a ramp or a sigmoid, but the results were insensitive to the particular choice so the most common form of decay was chosen, an exponential, s.t.

$$A_n(\tau) = A_n \exp\left(-\frac{\tau}{T_{\text{decay}}}\right) \sin(\omega_j \tau) \quad (7)$$

for $\tau > 0$

Physically, this damping was introduced to simulate a change in flow environment for the cavity and surrounding fluid, e.g. migration of the bubble from a region of high extension to one experiencing lower rates.

The time dependence of the external flow is characterized by four parameters: the complex amplitude constant A_n , the frequency ω and two time scales ξ and T_{decay} which apply in the intervals $[-\infty, 0]$ and $[0, \infty]$, respectively. Dimensionless groups which incorporate these values are shown in Table 6. The scaling of the amplitude a_2 on the magnitude

$|A_2|$ results from equations (IV.28) and (IV. 30) which show that these two quantities are directly proportional at time $t = \tau = 0$.

TABLE 6. Dimensionless Groups for External Flow

$$\frac{a_2}{|A_2| \tau_0 R_0} \quad (n = 2)$$

$$\tau_{\text{flow}} = \frac{1}{\omega \tau_0}$$

$$\tau_{\text{flow transient}} = \tau_{\text{f.t.}} = \frac{E}{\tau_0}$$

$$\tau_{\text{decay}} = \frac{T_{\text{decay}}}{\tau_0}$$

Sensitivity of the final results to $\tau_{\text{flow transient}}$ was easily anticipated. As the value of $\tau_{\text{f.t.}}$ decreased, viscoelastic changes were also reduced. This is consistent with the importance assigned to fluid history in distinguishing viscous and viscoelastic dynamics. Since this work is concerned with viscoelastic changes, this effect was minimized by allowing

$$\tau_{\text{f.t.}} \rightarrow \infty \quad (8)$$

Sensitivities to τ_{flow} and τ_{decay} are discussed in conjunction with the upcoming results.

The simplest flow case obtains for $\pi = 0$, a bubble of constant volume, just as it does for the quiescent fluid analysis. Results for

two different flow frequencies or τ_{flow} values are shown in Figure 33. The only difference between (a) and (b) is τ_{flow} . Figure 33(a) shows that $\tau_{flow} = 2.5 \times 10^5$ represents low frequency or slow flow since small instantaneous strain rates whose effects can be multiplied by viscoelastic stress integration result. Thus, a rather large difference is seen between the viscous and viscoelastic fluid responses and it increases with increasing Deborah number. However, as τ_{flow} decreases, the effect of viscoelastic properties decreases (see Figure 33(b)). The curves do not oscillate about the $a = 0$ axis because for these flow frequencies and phase, the flow is unidirectional over this time span, constantly "pulling" the bubble in one direction.

Conditions which combine flow and growth show no qualitatively new flow effects. The growth damps the oscillations and does not allow any initial viscoelastic differences to be magnified.

In Figures 34 and 35 results are presented for different collapse profiles with $\tau_{decay} = 0.25$. The damping of the external flow served to magnify differences between fluid, which were present at $t = 0$. This is entirely consistent with the notion that the viscoelastic fluid will "remember" the past occurrence of the external flow while the viscous fluid responds only to its instantaneous presence.

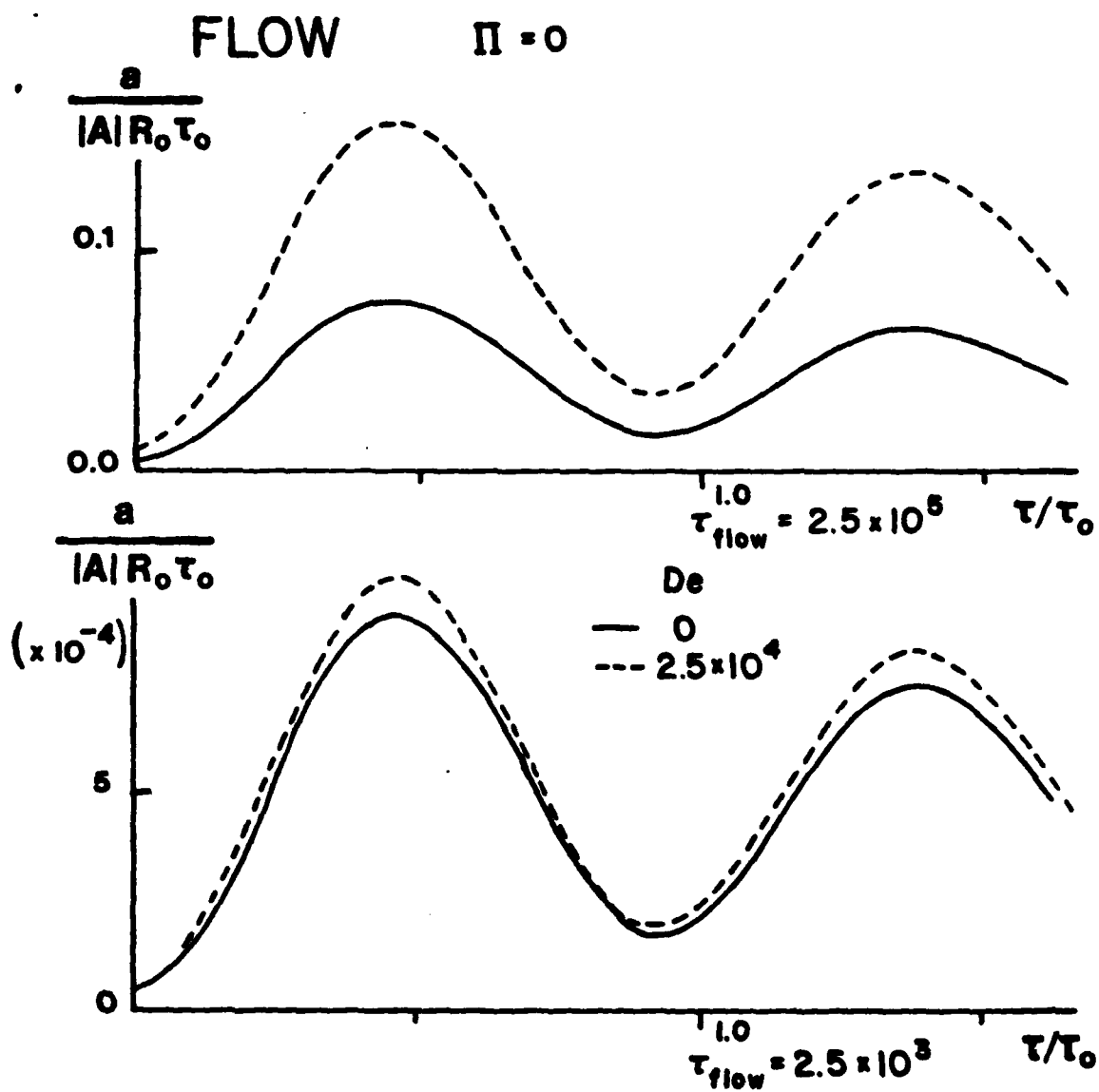


Figure 33. Effect of External Flow Frequency

(see Table 3)

$\zeta \rightarrow \infty$

$\tau_d \rightarrow \infty$

FLOW

$\Pi = -0.1$ Collapse

$\tau_{\text{flow}} = 2.5 \times 10^5$

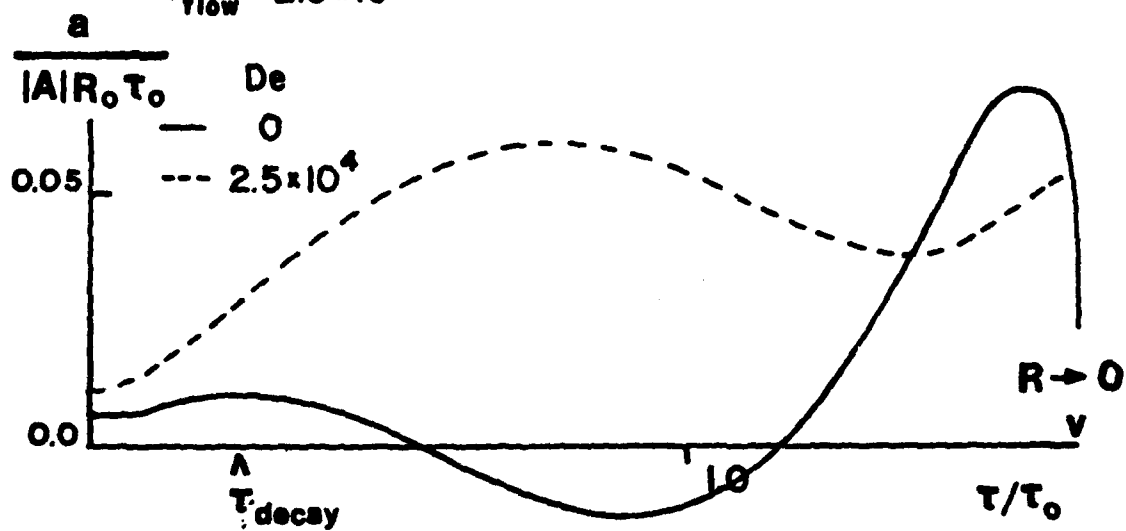


Figure 34. External Flow, Flow Decay and Bubble Collapse I

(see Table 3)

FLOW

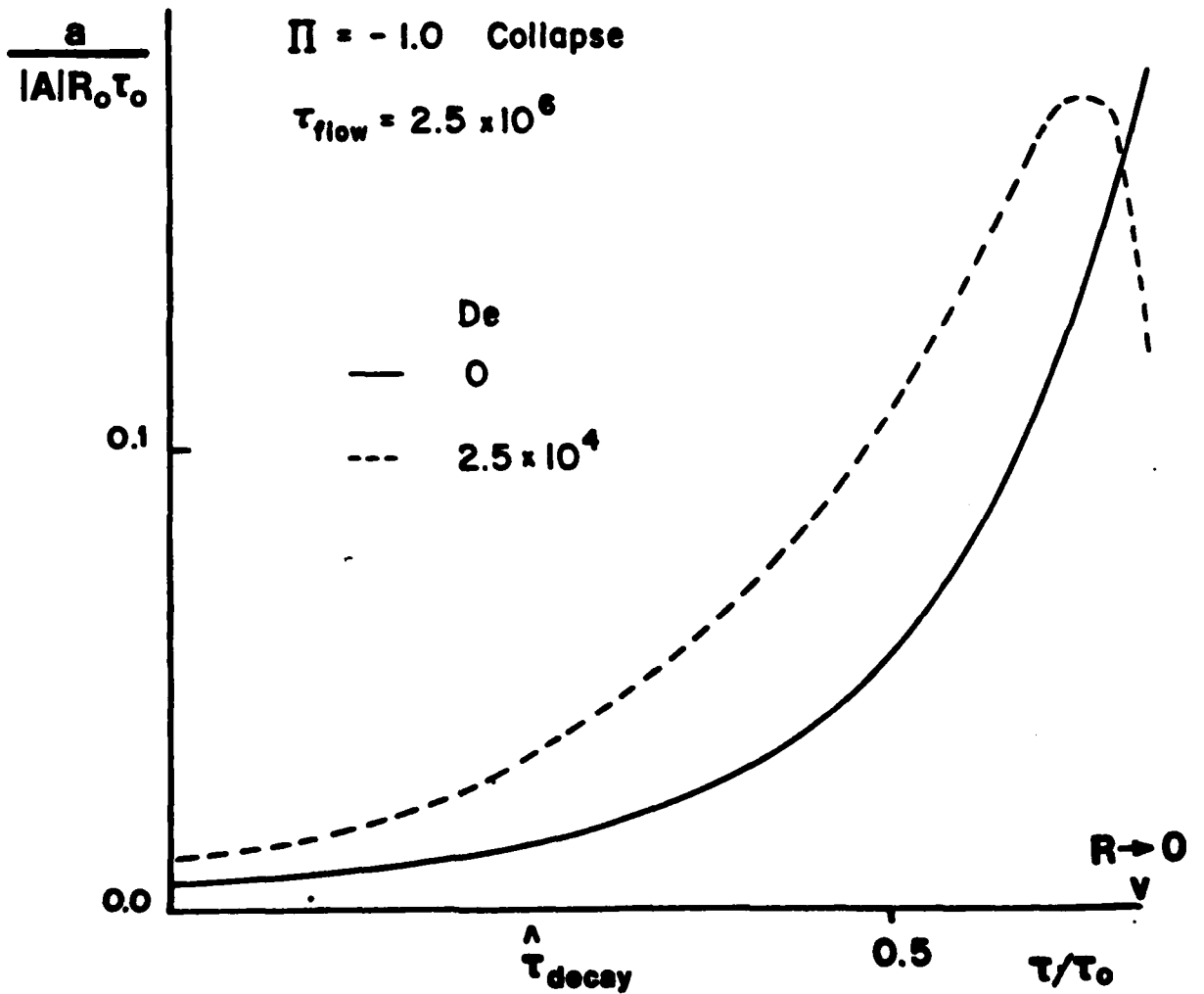


Figure 35. External Flow, Flow Decay and Bubble Collapse II (see Table 3)

VII. CONCLUSIONS AND DISCUSSION

The results of the previous section were presented individually, but it is only when they are taken collectively that more exciting conclusions can be drawn about real flow cavitation and their contribution to the understanding of cavitation inhibition can be assessed. In Table 1, the scope of the present work was resolved into three categories. The results obtained here suggest that:

1) Without any external flow, fluid rheology, and slight viscoelasticity in particular do not strongly influence cavitation bubble dynamics for A) spherical or B) nonspherical bubbles. The latter cavities do display non-negligible effects.

2) An external flow which is the sole source of system asymmetries will influence bubble dynamics and do so through fluid rheology.

3) The characteristics of bubble collapse near a solid wall are altered by nonsphericities which are present due to influences other than the "solid wall effect", e.g. external flow.

Of course, these conclusions all hold only for the particular theoretical and experimental systems tested. The fluid have viscosities on the order of 1. cp. and the elastic number, El , has a value near unity. These values may underestimate the influence of viscoelasticity on real dilute solution since oscillatory viscometric measurements for similar solutions give zero shear viscosities approaching 1 poise (Chang, 1975) but the values employed do model the experimental results very well which may be due to the shear-thinning behavior of the fluid.

There is a fundamental rheological difference between the non-sphericities in conclusion 1) and conclusion 2). In the former case, rheology is involved only in the evolution of the asymmetries, not their genesis or initiation. The fluid properties actually serve to generate the shape and stress field in the latter case, through the external flow. Since rheology is important in both generation and evolution, (pre-zero and post-zero dynamics), it is more important for this case.

Combined with conclusion 2), 3) can be seen as an example of a situation where viscoelasticity can be very important in cavitation near solid walls. Any flow past the wall will serve to create a stress field surrounding the cavity which will vary according to fluid rheology. This will create a nonspherical bubble, and these flow induced asymmetries will effect the jet induced by the solid wall upon bubble collapse.

This work also makes it clear why many previous model systems, which were constructed in an attempt to display large viscoelastic effects comparable to the cavitation inhibition of Figure 1, failed. These were designed to simulate cavitation in a quiescent fluid, and thus ignore the importance of stress history and flow.

VIII. THE NEXT STEPS

1. Theory

Experiments have shown the expansion technique employed here to be valid for surprisingly large departures from spherical shape. However this first order procedure is probably as far as a linearized model can be extended. The next step along similar lines in theory would incorporate a fully nonlinear constitutive model. Some of the relative simplicity of the present work might appear retainable through the introduction of a second expansion parameter, this one characterizing the flow field and not the bubble shape. Then, a second order expansion in this new parameter would be formulated so that nonlinear rheological effects, especially normal stresses are generated. Unfortunately, there are at least two definite problems with this approach. The second order terms will eliminate the use of the linear independence of the spherical harmonics. The angular dependencies will no longer be separate from the (r-t) formulation (see Appendix B). Even if this were resolved, the size of the bubble, governed by the zeroth order equations, is not coupled with the asymmetries and there is an interaction for the large deformations that the second order expansion would attempt to predict.

The next useful step in any modelling effort is treatment of the full problem. This is an extremely difficult undertaking since it is highly nonlinear, transient, contains an undetermined free surface and requires an infinite domain. Since the development would aim toward incorporating a general flow field and a solid wall, no symmetry simplifications emerge and the full three-dimensional problem appears

necessary. Marker and cell techniques which have been used to model bubbles near solid walls without external flow might be applicable for the Newtonian liquid or even a shear thinning, but inelastic, fluid. However, incorporation of non-Newtonian, elastic, effects probably requires a finite element treatment, techniques for which are still under development.

2. Experiments

Many of the experiments proposed here are in various stages of development at Princeton University.

The early successes of techniques to generate nonspherical bubbles with or without solid walls present suggests that similar experiments be attempted on other liquids and on the same fluids described here, but under different conditions. The aim of such changes in experimental conditions would be to broaden the range of bubble sizes and profiles for which reproducible trials can be conducted. Alternative fluids include a glycerine/H₂O solvent system which allows variation in viscosity through the composition ratio, and could be investigated with and without polyacrylamide solutes. More flexibility in useful trials for the aqueous system might be achieved by locally or non-locally dyeing or tinting the fluid to change energy absorption by the fluid. Such a procedure would need careful testing for such complications as asymmetric thermal effects which would alter reproducibility.

All trials should be viewed with particular regard as to how and when jets form. These variations might be measured using a pressure transducer on the solid wall to record the impact of any jet which forms.

More sophisticated photographic techniques may also allow measurement of jet velocities.

Flow experiments also need to be performed. The best flows would be the two-dimensional extension approximated by a four-roll or four-roller apparatus or two impinging sheet-shaped jets. However any well-characterized flow which imparts stress history to the fluid would give useful results.

IX. BIBLIOGRAPHY

- Acosta, A. J. and B. R. Parkin, *J. Ship Res.* 19, 193-203 (1975)
Cavitation - A Selective Review.
- Avanesov, A. M., I. A. Avetisyan and A. T. Listrov, *Soviet Phys. Acoust.*
22(6), 461-464 (1976)
Influence of Polymer Additives on Bubble Motion and Cavitation
Noise Intensity.
- Batchelor, G. K., Cambridge, 1970, 615 pp.
Fluid Dynamics.
- Bird, R. B., R. C. Armstrong and O. Hassager, Wiley, 1977, 470 pp
Dynamics of Polymeric Liquids, Volume I: Fluid Mechanics
- Chahine, G. L., "Experimental and asymptotic study of nonspherical bubble
collapse" in *Mechanics and Physics of Bubbles in Liquids*, ed. by L.
van Wijngaarden Martinus Nijhoff, 1982.
- Chahine, G. L. and D. H. Fruman, *Phys. Fluids* 22, 1406-1407 (1977).
Dilute Polymer Solution Effects on Bubble Growth and Collapse.
- Chahine, G. L. and A. K. Morine, *Ecole Nationale Superieure de Technique*
Advances Rapport de Recherche 133 (June 1980).
The Influence of Polymer Additives on the Collapse of a Bubble
Between Two Solid Walls.
- Chandrasekhar, S., *Hydrodynamic and Hydromagnetic Stability*, Oxford,
1961, 654 pp.
- Chang, C-F., Princeton, Oct. 1975, Thesis: Secondary Flow Induced by
a Cylinder Oscillating in a Viscoelastic Liquid.
- Chapman, R. B. and M. S. Plesset, *J. Basic Eng.* D94, 142-146,
Nonlinear Effects in the Collapse of a Nearly Spherical Cavity in
a Liquid.
- Coutanceau, M. and M. Haijam, "Viscoelastic effect on the behaviour of
an air bubble rising axially in a tube" in *Mechanics and Physics of*
Bubbles in Liquids, ed. by L. van Wijngaarden, Martinus Nijhoff, 1982.
- Cox, R. G., *JFM*, 37, 601-623 (1969).
The Deformation of a Drop in a General Time-Dependent Fluid Flow.
- Dergarabedian, P., *J. Appl. Mech.* 20, 537-545 (1953).
The Rate of Growth of Vapor Bubbles in Superheated Water.
- Ellis, A. T. and J. W. Hoyt, *ASME 1968 Cavitation Forum* p 2-3,
Some Effects of Macromolecules on Cavitation Inception.

- Ellis, A. T. and R. Y. Ting, Non-Newtonian Effects on Flow Generated Cavitation in a Pressure Field, in "Fluid Mechanics, Acoustics and Design of Turbomachinery", NASA-SP-304, pt 1, 403-421 (1974).
- Ellis, A. T., J. G. Waugh and R. Y. Ting, J. Basic Eng. 3D, 459 (1970), Cavitation Suppression and Stress Effects in High-Speed Flows of Water with Dilute Macromolecular Additives.
- Eskin, Yu. A., V. P. Il'in and Yu. L. Levkoski, Sov. Phys. Acoust. 21(2), 187-188, Experimental Study of the Effect of Polymer Additives on the Energy Characteristics of Bubble Cavitation Noise.
- Flynn, H. G., Cavitation Dynamics, J. Acoust. Soc. Am. 57(6), 1379-1396 (1975), I. A Mathematical Formulation; J. Acoust. Soc. Am. 58(6), 1160-1170 (1976), II. Free Pulsations and Models for Cavitation Bubbles.
- Fogler, H. S. and J. D. Goddard, Phys. Fluids, 13, 1135-1141 (1970). Collapse of Spherical Cavities in Viscoelastic Fluids.
 _____ J. Appl. Phys., 42, 259-263 (1971).
 Oscillations of a Gas Bubble in Viscoelastic Liquids Subject to Acoustic and Impulsive Pressure Variations.
- Gibson, D. C. and J. R. Blake, "The Growth and collapse of bubbles near deformable surfaces", in Mechanics and Physics of Bubbles in Liquid, ed. by L. van Wijngaarden Martinus Nijhoff, 1982.
- Hammitt, F. G., Cavitation and Multiphase Flow Phenomena, McGraw-Hill, 1980, 423 pp.
- Happel, J. and H. Brenner, Prentice-Hall, 1965, Noordhoff International, 1973, Low Reynolds Number Hydrodynamics with Special Application to Particulate Media.
- Hassager, O., Bubble Motion in Structurally Complex Fluids, in Chemical Engineering with Per. Søltøff, ed. by K. Østergaard and Aa. Fredenslund Teknisk Forlag., Copenhagen, 1977.
 _____ Nature, 279, 5712, 402-3 (1979). Negative Wake behind Bubbles in non-Newtonian Liquids.
- Hobson, E. W., Chelsea, 1955, 500 pp.
 The Theory of Spherical and Ellipsoidal Harmonics.
- Hoyt, J. W., J. Fluid Eng., 98, 106-112 (1976).
 Effect of Polymer Additives on Jet Cavitation
- Hsieh, D. Y., J. Basic Eng., 87, 991-1005 (1965).
 Some Analytical Aspects of Bubble Dynamics.
 _____ J. Basic Eng., 94, 655-665 (1974).
 On the Dynamics of Nonspherical Bubbles.

- Inge, C. and F. H. Bark, Surface Tension Driven Oscillations of a Bubble in a Viscoelastic Fluid, in *Mechanics and Physics of Bubbles in Liquid*, ed. by L. van Wijngaarden Martinus Mijhoff, 1982.
- Knapp, R. T., J. W. Daly and F. G. Hammit, *Cavitation*, McGraw-Hill, 1970.
- Lamb, Sir Horace, Dover 1945, 738 pp., *Hydrodynamics*.
- Lauterborn, W., *Appl. Phys. Letters*, 21, 27-29 (1972). High-speed Photography of Laser-induced Breakdown in Liquids.
- Lauterborn, W. and H. Bolle, *JFM*, 72, 391-399 (1975), Experimental Investigations of Cavitation Bubble Collapse in the Neighborhood of a Solid Boundary.
- Lauterborn, W. and K. J. Ebeling, *App. Phys. Letters*, 31(10), 663-664 (1977), High-speed Holography of Laser-induced Breakdown of Liquids.
- MacRobert, T. M., Dover, 1948, 372 pp., *Spherical Harmonics*.
- Mitchell, T. M. and F. G. Hammit, *J. Fl. Eng'g (Trans. ASME)*, 95(1), 29-37 (1973), Asymmetric Cavitation Bubble Collapse.
- Oba, R., Y. Ito and K. Uranishi, *J. Fl. Eng'g (Trans. ASME)*, 100, 493-499 (1978), Effect of Polymer Additives on Cavitation Development and Noise in Water Flow Through an Orifice.
- Pearson, G. H. and S. Middleman, *CES*, 29, 1051-1053 (1974), Comments on a New Method for Determination of Surface Tension of Viscous Fluids.
- _____ *AICHEJ*, 23 (1977), Elongational Flow Behavior of Viscoelastic Liquids: Part I, 714-721; Part II, 721-725.
- _____ *Rheo Acta*, 17, 500-510 (1978), Elongational Flow Behavior of Viscoelastic Liquids: Modelling Bubble Dynamics with Viscoelastic Constitutive Relations.
- Plesset, M. S., *J. Appl. Phys.*, 25, 96-98 (1954), On the Stability of Fluid Flows with Spherical Symmetry.
- _____ *Bubble Dynamics*, in "Cavitation in Real Fluids", ed. by R. Davies, Elsevier, 1964.
- Plesset, M. S. and R. B. Chapman, *JFM*, 47, 283-290 (1971), Collapse of an Initially Spherical Vapor Cavity in the Neighborhood of a Solid Boundary.
- Plesset, M. S. and T. P. Mitchell, *Q. App. Math.*, 13, 419-430 (1956), On the Stability of the Spherical Shape of a Vapor Cavity.
- Plesset, M. S. and A. Prosperetti, *Bubble Dynamics and Cavitation in "Annual Review of Fluid Mechanics"*, Vol. 9, 1977, pp. 145-186.

Plesset, M. S. and S. A. Zwick, *J. Appl. Phys.*, 23, 95-98 (1952),
A Non-steady Heat Diffusion Problem with Spherical Symmetry.

_____ *J. App. Phys.*, 25, 493-500 (1954). The Growth of Vapor Bubbles
in Superheated Liquids.

Prosperetti, A., *Q. App. Math.*, 34, 339-352 (1977). Viscous Effects on
Perturbed Spherical Flows.

_____ "Bubble Dynamics: A Review and Some Recent Results" in
Mechanics and Physics of Bubbles in Liquids, ed. by L. Van Wijngaarden
Martinus Nijhoff, 1982.

_____ *JFM*, 100(2), 333-348 (1980), Free Oscillations of Drops and
Bubbles: the Initial Value Problem.

Prosperetti, A. and M. S. Plesset, *JFM*, 85, 349-368 (1978), Vapour Bubble
Growth in a Superheated Liquid.

Prosperetti, A. and G. Seminara, *Phys. Fluids*, 21, 1465 (1978), Linear
Stability of a Growing or Collapsing Bubble in a Slightly Viscous
Liquid.

Rayleigh, *Philos Mag.*, 34, 94-98 (1917), On the Pressure developed in
a Liquid during the Collapse of a Spherical Cavity.

Schowalter, W. R., Pergamon, 1978, 300 pp., *Mechanics of Non-Newtonian
Fluids*.

Scriven, L. E., *CES*, 12, 98-108 (1960), Dynamics of a Fluid Interface.

Shima, A. and K. Nakajima, *JFM*, 80(2), 369-391 (1977), The Collapse of
a Non-hemispherical Bubble Attached to a Solid Wall.

Tanasawa, I. and W-J. Yang, *J. App. Phys.* 41(11), 4526-4531 (1970),
J. App. Phys. 41(11), 4526-4531 (1970), Dynamic Behavior of a Gas
Bubble in Viscoelastic Liquids.

Ting, R. Y., *AIChE J.*, 21, 810-813 (1975), Viscoelastic Effects of
Polymers on Single Bubble Dynamics.

_____ *Phys. Fluids*, 20, 1427-1431 (1977), Effect of Polymer Vis-
coelasticity on the Initial Growth of a Vapor Bubble from Gas Nuclei.

_____ *Phys. Fluids*, 21, 898-901 (1978), Characteristics of Flow
Cavitation in Dilute Solutions of Polyethylene Oxide and Polyacrylamide.

Ting, R. Y. and A. T. Ellis, *Phys. Fluids*, 17, 1461 (1974), Bubble Growth
in Dilute Polymer Solutions.

Voinov, O. V. and V. V. Voinov, Sov. Phys. Dokl., 20, 179-180 (1975),
Numerical Method of Calculating Non-stationary Motions of an Ideal
Incompressible Fluid with Free Surfaces.

_____, Sov. Phys. Dokl., 21, 133-135 (1976), On the Process of
Collapse of a Cavitation Bubble near a Wall and the Formation of a
Cumulative Jet.

Yang, W-J. and H-C Yeh, Phys. Fluids, 8, 758-760 (1965), Approximate
Method for the Determining of Bubble Dynamics in non-Newtonian Fluid.

You, H-J and C-D Hsu, AIChE J., 28(6), 1002-1009 (1982), Oscillatory
Behavior of a Gas Bubble Growing (or Collapsing) in Viscoelastic
Liquids.

Zana, E. and L. G. Leal, Ind. Eng. Chem. Fund., 14, 175-182 (1975),
Dissolution of a Stationary Gas Bubble in a Quiescent, Viscoelastic
Fluid.

Zwick, S. A. and M. S. Plesset, J. Math & Phys., 33, 308-330 (1955),
On the Dynamics of Small Vapor Bubbles in Liquids.

APPENDIX A: $O(\epsilon)$ EquationsA.1. Toroidal Field Equation

The full velocity field, to $O(\epsilon)$, is given by

$$\underline{v} = \underline{v}_0 + \epsilon \underline{v}_p + \epsilon \underline{v}_v \quad (\text{III.16})$$

where the (ϵ^0) field, in spherical coordinates, is

$$(\underline{v}_0)_\theta = (\underline{v}_0)_\phi = 0 \quad (\text{III.1})$$

$$(\underline{v}_0)_r = \frac{\dot{R}R^2}{r^2}$$

The potential contribution derived by Plesset is

$$\underline{v}_p = \sum_n \underline{v} \phi_{p,n} \quad (\text{III.19})$$

$$\phi_{p,n} = -\frac{1}{n+1} \frac{R^{n+2}}{r^{n+1}} \left[\dot{a}_n + 2a_n \frac{\dot{R}}{R} \right] Y_n^m(\theta, \phi)$$

Rheological contributions are contained in \underline{v}_v term which obtains from Equation (III.28) as

$$\begin{aligned} (\underline{v}_v)_r &= \sum_n \left(T_n - \frac{\partial B_n}{\partial r} \right) Y_n^m \\ (\underline{v}_v)_\theta &= \sum_n \left(-\frac{B_n}{r} \right) \frac{\partial Y_n^m}{\partial \theta} \\ (\underline{v}_v)_\phi &= \sum_n \left(-\frac{B_n}{r \sin \theta} \right) \frac{\partial Y_n^m}{\partial \phi} \end{aligned} \quad (\text{A.1})$$

where $B_n(r,t)$ is defined as the function containing the radial and temporal dependence of the integral ϕ_n defined by equation (III.29) with the external flow contribution of equation

$$\phi_n(r, \theta, \phi, t) = B_n(r, t) Y_n^m(\theta, \phi) \quad (\text{A.2})$$

$$\begin{aligned} B_n(r, t) = & [\alpha_n(t) - A_n(t)] \\ & + \frac{n+1}{2n+1} \int_R^r S^{-n} T_n(s, t) dS] r^n \\ & + \left\{ \frac{n}{n+1} R^{2n+1} [\alpha_n(t) - A_n(t)] \right. \\ & \left. + \frac{n}{2n+1} \int_R^r S^{n+1} T_n(s, t) dS \right\} r^{-(n+1)} \\ & = X_n(r, t) r^n + Z_n(r, t) r^{-(n+1)} \end{aligned} \quad (\text{A.3})$$

This equation also serves to define X_n and Z_n , with $\alpha_n(t)$ given by equation (III.30).

The goal of this first derivation is an analogue to the vorticity equation

$$\frac{\partial \omega}{\partial t} + \underline{v} \cdot \nabla \omega - \omega \cdot \nabla \underline{v} = \nabla \times (\text{stress}) \quad (\text{III.22})$$

since the simultaneous evaluation of the pressure field and toroidal function T_n is not necessary nor is the potential flow field. This

must be accomplished with special attention to the Lagrangian and non-instantaneous nature of the stress expression. The left-hand side (LHS) of the equation, containing the terms which represent inertial effects is not altered by the particular constitutive relation employed, but does need to be expressed in the proper coordinate system.

The components of the vorticity vector in Eulerian coordinates are first order in ϵ .

$$\underline{\omega} = \nabla \times (\underline{v}_p + \underline{v}_v) = \nabla \times \underline{v}_v \quad (\text{III.21})$$

$$(\underline{\omega})_r = 0$$

$$(\underline{\omega})_\theta = \sum_n \frac{T_n}{r \sin \theta} \frac{\partial Y}{\partial \phi} \quad (\text{A.4})$$

$$(\underline{\omega})_\phi = - \sum_n \left(- \frac{T_n}{r} \right) \frac{\partial Y}{\partial \theta}$$

The $(\text{LHS})_r$, the radial-component equation of the left-hand side of the vorticity equation, has terms which are all identically zero. At first order in ϵ , the θ and ϕ equations vary only in their angular dependencies

$$\begin{aligned} \frac{(\text{LHS})_\theta}{\frac{1}{\sin \theta} \frac{\partial Y}{\partial \phi}} &= - \frac{(\text{LHS})_\phi}{\frac{\partial Y}{\partial \theta}} \\ &= \frac{1}{r} \left\{ \frac{\partial T_n}{\partial t} + \frac{\partial}{\partial r} \left[\dot{R} \left(\frac{R}{r} \right)^2 T_n \right] \right\} \end{aligned} \quad (\text{A.5})$$

This term can be expressed in Lagrangian (H, τ) coordinates, defined by

equation (III.38) as

$$\frac{1}{L} \left\{ \frac{\partial T}{\partial \tau} - 2 R^2 \dot{R} \frac{T}{L^3} \right\} \quad (\text{A.6})$$

where

$$L = (R^3 + 3H)^{1/3} \quad (\text{A.7})$$

The right-hand side (RHS) of the vorticity equation consists of stress-generated expressions, so it must be analyzed more carefully than the left, with particular attention paid to the order and reference frame in which time integrations and spatial differentiations are performed. This is crucial for proper derivation of terms of the form

$$\begin{aligned} \nabla_{\mathbf{r}} \times \nabla_{\mathbf{r}} \cdot \underline{\underline{\tau}}(\mathbf{r}, \tau) / \rho \\ = \nabla_{\mathbf{r}} \times \nabla_{\mathbf{r}} \cdot \int_{-\infty}^{\tau} N(\tau - \tau') \dot{\underline{\underline{\gamma}}}(\mathbf{H}, \tau') d\tau' \\ \neq \int_{-\infty}^{\tau} \nabla_{\mathbf{H}} \times \nabla_{\mathbf{H}} \cdot [N(\tau - \tau') \dot{\underline{\underline{\gamma}}}(\mathbf{H}, \tau')] d\tau' \end{aligned} \quad (\text{A.8})$$

where $\underline{\underline{\tau}}$ and $\dot{\underline{\underline{\gamma}}}$ are stress tensor and strain rate tensor, respectively, and the subscripts \mathbf{r} and \mathbf{H} are convenient shorthands to specify the particular reference frame in which the del-operator (∇) is defined. Begin with expressions for the rate-of-strain tensor $\dot{\underline{\underline{\gamma}}}^{(\mathbf{r})}(\mathbf{r}, t)$

$$\dot{\gamma}_{rr}^{(v)} = 2 \left(\frac{\partial T_n}{\partial r} - \frac{\partial^2 B_n}{\partial r^2} \right) Y_n^m \quad (\text{A.9})$$

$$\dot{\gamma}_{\theta\theta}^{(v)} = 2 \left[-\frac{B_n}{r^2} \frac{\partial^2 Y_n^m}{\partial \theta^2} + \frac{1}{r} \left(T_n - \frac{\partial B_n}{\partial r} \right) Y_n^m \right]$$

$$\dot{\gamma}_{\phi\phi}^{(v)} = 2 \left[-\frac{B_n}{r^2 \sin^2 \theta} \frac{\partial^2 Y_n^m}{\partial \phi^2} + \frac{1}{r} \left(T_n - \frac{\partial B_n}{\partial r} \right) Y_n^m \right]$$

$$- \frac{B_n \cos \theta}{r^2 \sin \theta} \frac{\partial Y_n^m}{\partial \theta}]$$

$$\dot{\gamma}_{r\theta}^{(v)} = \dot{\gamma}_{\theta r}^{(v)} = \left[-r \frac{\partial}{\partial r} \left(\frac{B_n}{r^2} \right) + \frac{1}{r} \left(T_n - \frac{\partial B_n}{\partial r} \right) \right] \frac{\partial Y_n^m}{\partial \theta}$$

$$\dot{\gamma}_{\theta\phi}^{(v)} = \dot{\gamma}_{\phi\theta}^{(v)} = -\frac{B_n \sin \theta}{r^2} \frac{\partial}{\partial \theta} \left(\frac{1}{\sin^2 \theta} \frac{\partial Y_n^m}{\partial \phi} \right)$$

$$- \frac{B_n}{r^2 \sin \theta} \frac{\partial^2 Y_n^m}{\partial \theta \partial \phi}$$

$$\dot{\gamma}_{r\phi}^{(v)} = \dot{\gamma}_{\phi r}^{(v)} = \frac{1}{\sin \theta} \left[\frac{1}{r} \left(T_n - \frac{\partial B_n}{\partial r} \right) - r \frac{\partial}{\partial r} \left(\frac{B_n}{r^2} \right) \right] \frac{\partial Y_n^m}{\partial \phi}$$

The stress tensor can be written in terms of integrals of the strain rate components as

$$\tau_{rr}^{(v)} = 2 f_1 Y_n^m \quad (\text{A.10})$$

$$\tau_{\theta\theta}^{(v)} = 2 [f_2 \frac{\partial^2 Y_n^m}{\partial \theta^2} + f_3 Y_n^m]$$

$$\tau_{\phi\phi}^{(v)} = 2 \left[\frac{f_2}{\sin^2\theta} \frac{\partial^2 Y}{\partial \phi^2} + f_3 Y_n + f_2 \cot\theta \frac{\partial}{\partial \theta} \right]$$

$$\tau_{r\theta}^{(v)} = \tau_{\theta r}^{(v)} = (f_3 + f_4) \frac{\partial Y}{\partial \theta}$$

$$\tau_{\theta\phi}^{(v)} = \tau_{\phi\theta}^{(v)} = f_2 \left[\sin\theta \frac{\partial}{\partial \theta} \left(\frac{1}{\sin^2\theta} \frac{\partial Y}{\partial \phi} \right) + \frac{1}{\sin\theta} \frac{\partial^2 Y}{\partial \theta \partial \phi} \right]$$

$$\tau_{r\phi}^{(v)} = \tau_{\phi r}^{(v)} = (f_3 + f_4) \frac{1}{\sin\phi} \frac{\partial r}{\partial \phi}$$

where

$$f_{1,n}(H,\tau) = \int_{-\infty}^{\tau} N(\tau-\tau') \left[\frac{\partial T}{\partial r} - \frac{\partial^2 B}{\partial r^2} \right]_H d\tau' \quad (A.11)$$

$$f_{2,n}(H,\tau) = \int_{-\infty}^{\tau} N(\tau-\tau') \left[-\frac{B}{r^2} \right]_H d\tau'$$

$$f_{3,n}(H,\tau) = \int_{-\infty}^{\tau} N(\tau-\tau') \left[\frac{1}{r} \left(T - \frac{\partial B}{\partial r} \right) \right]_H d\tau'$$

$$f_{4,n}(H,\tau) = \int_{-\infty}^{\tau} N(\tau-\tau') \left[r \frac{\partial}{\partial r} \left(-\frac{B}{r^2} \right) \right]_H d\tau'$$

despite some cumbersome symbolism, these time-integrals are evaluated for constant H , while with in the stress expressions they are operated

upon in the (r,t) system. Algebraic manipulations result in the components of the right-hand side of the vorticity equation

$$\underline{v} \times (\underline{v} \cdot \underline{r}) \quad (\text{A.12})$$

$$[\underline{v} \times (\underline{v} \cdot \underline{r})]_r = 0$$

$$\frac{[\underline{v}_r \times (\underline{v}_r \cdot \underline{r})]_\theta}{\frac{\rho}{\sin\theta} \frac{\partial Y}{\partial \phi}} = - \frac{[\underline{v}_r \times (\underline{v}_r \cdot \underline{r})]_\phi}{\rho \frac{\partial}{\partial \theta}}$$

$$= \frac{4}{L^2} (f_1 - f_3) + \frac{n(n+1)}{L^2} (2f_2 - f_3 - f_4)$$

$$+ \frac{2n(n+1)}{L} \frac{\partial f_2}{\partial r} + \frac{2}{L} \frac{\partial}{\partial r} (f_1 - f_2 - 3f_3 - 2f_4)$$

$$- \frac{\partial^2}{\partial r^2} (f_3 + f_4)$$

$$= \frac{4}{L^2} \int_{-\infty}^r N' \left(-\frac{T}{L} + \frac{\partial T}{\partial L} + \frac{1}{L} \frac{\partial B}{\partial L} - \frac{\partial^2 B}{\partial L^2} \right) \Big|_H d\tau'$$

$$+ \frac{n(n+1)}{L^2} \int_{-\infty}^r N' \left(-\frac{T}{L} - \frac{4B}{L^2} + \frac{2}{L} \frac{\partial B}{\partial L} \right) \Big|_H d\tau'$$

$$+ \frac{2n(n+1)}{L} \frac{\partial}{\partial L} \int_{-\infty}^r N' \left(-\frac{B}{L^2 r} \right) d\tau'$$

$$+ \frac{2}{L} \frac{\partial}{\partial L} \int_{-\infty}^{\tau} N' \left(-\frac{4T}{L'} + \frac{\partial T}{\partial L} - \frac{5B}{L'^2} + \frac{7}{L'} \frac{\partial B}{\partial L} - \frac{\partial^2 B}{\partial L'^2} \right) \Big|_H d\tau'$$

$$- \frac{\partial^2}{\partial L^2} \int_{-\infty}^{\tau} N' \left(\frac{T}{L'} + \frac{2B}{L'^2} - 2 \frac{\partial B}{\partial L} \right) \Big|_H d\tau'$$

where the final expression comes simply from direct substitution of the definitions of f_1 , f_2 , f_3 and f_4 . From the definitions of B_n , X_n and Z_n , it is possible to simplify these expressions, using

$$\frac{\partial B_n}{\partial r} = nr^{n-1} X_n - (n+1)r^{-(n+2)} Z_n + T_n \quad (\text{A.13})$$

$$\frac{\partial^2 B_n}{\partial r^2} = n(n-1)r^{n-2} X_n + (n+1)(n+2)r^{-(n+3)} Z_n + \frac{\partial T_n}{\partial r} \quad (\text{A.14})$$

and combining like terms and integrals, the stress-related expression becomes (A.15)

$$\begin{aligned} & \frac{1}{L^2} \int_{-\infty}^{\tau} N' \{ [2n(n-2)(n-1)] X_n L'^{(n-2)} \\ & - 2(n+1)(n+2)(n+3) Z_n L'^{-(n+3)} \\ & + n(n+1) \frac{T_n}{L'} \} d\tau' \end{aligned}$$

$$\begin{aligned}
& + 2L \frac{\partial}{\partial H} \int_{-\infty}^{\tau} N' \{[-(2n-5)(n-1)]X_n L'^{(n-2)} \\
& \quad - (2n+7)(n+2)Z_n L'^{-(n+3)} \\
& \quad + 3 \frac{T_n}{L'} \} d\tau' \\
& + L^4 \frac{\partial^2}{\partial H^2} \int_{-\infty}^{\tau} N' \{+ 2(n-1)X_n L'^{(n-2)} \\
& \quad - 2(n+2)Z_n L'^{-(n+3)} + \frac{T_n}{L'} \} d\tau' .
\end{aligned}$$

The differentiation in H can be performed inside the time integrals and the operations applied in deriving (A.13) and (A.14) can be re-applied until the RHS is derived in the form which was employed in the final T-equation (A.16)

$$\begin{aligned}
& \frac{1}{L^2} \int_{-\infty}^{\tau} N(\tau-\tau') \{2n(n-2)(n-1)X_n(H, \tau') L'^{(n-2)} \\
& \quad - 2(n+1)(n+2)(n+3)Z_n(H, \tau') L'^{-(n+3)} \\
& \quad + n(n+1) \frac{T_n(H, \tau')}{L'} \} d\tau' \\
& + 2L \int_{-\infty}^{\tau} N(\tau-\tau') \{-(2n-5)(n-1)(n-2)X_n(H, \tau') L'^{(n-5)} \\
& \quad + (n+2)(n+3)(2n+7)Z_n(H, \tau') L'^{-(n+6)}
\end{aligned}$$

$$\begin{aligned}
& - 2(n^2+n+4) \frac{T_n(H, \tau')}{L^{n+4}} \\
& + \frac{3}{L} \frac{\partial T_n}{\partial H} d\tau' \\
& + L^4 \int_{-\infty}^{\tau} N(\tau-\tau') \{2(n-1)(n-2)(n-5) X_n(H, \tau') L^{-(n-8)} \\
& - 2(n+2)(n+3)(n+6) Z_n(H, \tau') L^{-(n+9)} \\
& + 2(n^2+n+8) \frac{T_n(H, \tau')}{L^{n+7}} - \frac{4}{L^{n+6}} \frac{\partial T_n}{\partial H} + \frac{1}{L} \frac{\partial^2 T_n}{\partial H^2}\} d\tau'
\end{aligned}$$

Thus, the dimensional vorticity equation, expressed in terms of the toroidal field function $T_n(H, \tau)$ can be written as

$$\begin{aligned}
\frac{\partial T_n}{\partial \tau} - 2R^2 \dot{R} \frac{T_n}{L^3} &= \nu L \left[2 \frac{\partial T_n}{\partial H} + L^3 \frac{\partial^2 T_n}{\partial H^2} - n(n+1) \frac{T_n}{L^3 \right] \\
& + \frac{G}{\rho} \left\{ \frac{1}{L} \int_{-\infty}^{\tau} \exp\left(\frac{\tau'-\tau}{\lambda}\right) I_1(H, \tau') d\tau' \right. \\
& + L^2 \int_{-\infty}^{\tau} \exp\left(\frac{\tau'-\tau}{\lambda}\right) I_2(H, \tau') d\tau' \\
& \left. + L^5 \int_{-\infty}^{\tau} \exp\left(\frac{\tau'-\tau}{\lambda}\right) I_3(H, \tau') d\tau' \right\}
\end{aligned}$$

where the integrands I_j were given previously in (III.41).

A.2 Amplitude Equations

In order to derive the boundary conditions at the bubble surface, the asymmetric pressure field must be evaluated at $r = R$, ($H=0$) as must the normal and tangential extra stresses.

The contribution to the pressure from the v -velocity is evaluated by integrating the equation of motion. In Lagrangian coordinates, for the θ -component

$$\begin{aligned} \rho \left\{ \frac{\partial v_\theta}{\partial \tau} + \frac{\dot{R}R^2}{L} \frac{\partial}{\partial H} (Lv_\theta) + \dot{R}R^2 \frac{\partial}{\partial H} (v_\theta) \right\} \\ = - \frac{1}{L} \frac{\partial p_v}{\partial \theta} + (\underline{\nabla} \cdot \underline{\tau})_\theta \end{aligned} \quad (\text{A.17})$$

where $v_\theta = (v_v)_\theta$. Calculations performed in the development of the T -equation give:

$$\begin{aligned} (\underline{\nabla} \cdot \underline{\tau})_\theta = \rho \left\{ \frac{2f_2}{L} [-n(n+1) + 1] \right. \\ \left. + \frac{1}{L^3} \frac{\partial}{\partial L} (L^3 f_3) + \frac{1}{L^3} \frac{\partial}{\partial L} (L^3 f_4) \right\} \frac{\partial Y}{\partial \theta} \end{aligned} \quad (\text{A.18})$$

The angular dependence of each term in this θ -equation except the pressure term has been determined to be $\partial Y_n^m / \partial \theta$. Thus the pressure term also has this dependence and can be written to define P_v as

$$P_v(H, \theta, \phi, \tau) = P_v(H, \tau) Y_n^m(\theta, \phi)$$

Thus, angular dependencies can be factored from equation (A.17) and an expression for $P_v(H, \tau)$ results. Fortunately, only the value at the bubble surface, $H=0$, needs to be explicitly considered. If, in the development of this expression, the shorthand notation

$$\bar{v}_\theta = \frac{(\underline{v}_v)_\theta}{\frac{\partial Y}{\partial \theta}} = - \frac{B_n(H, \tau)}{L} \quad (\text{A.1})$$

is adapted, then

$$\frac{\partial}{\partial H} (L \bar{v}_\theta) = - X_n n L^{(n-3)} + Z_n (n+1) L^{-(n+4)} - \frac{T_n}{L^2} \quad (\text{A.19})$$

$$\begin{aligned} \frac{\partial \bar{v}_\theta}{\partial H} &= \frac{1}{L} \frac{\partial}{\partial H} (L \bar{v}_\theta) - \frac{\bar{v}_\theta}{L} \frac{\partial L}{\partial H} \\ &= - X_n (n-1) L^{(n-1)} + (n+2) Z_n L^{-(n+5)} - \frac{T_n}{L^3} \end{aligned} \quad (\text{A.20})$$

and

$$\begin{aligned} \left. \frac{\partial \bar{v}_\theta}{\partial} \right|_{H=0} &= R^{(n-1)} \int_R^\infty S^{-n} \frac{\partial T_n}{\partial \tau} dS \\ &- \frac{\dot{R}}{R} T_n(H=0, \tau) + \frac{2n+1}{n+1} R^{(n-1)} \frac{\partial A}{\partial \tau} \\ &- \frac{(2n+1)(n-1)}{(n+1)} R^{(n-2)} \dot{R} [\alpha_n(\tau) - A_n(\tau)] \end{aligned} \quad (\text{A.21})$$

The stress terms are also considerably simpler when evaluated at the

surface (A.22)

$$[1-n(n+1)] \frac{2f_2}{R} + \frac{5f_3}{R} + \frac{3f_4}{R}$$

$$= \frac{1}{R} \int_{-\infty}^{\tau} N' \left\{ -3 \left[\frac{T_n(H=0, \tau')}{R} \right] \right.$$

$$\left. + 2[(n-1)(n-2) + (n+2)(n+3) \left(\frac{n}{n+1}\right) R^{(n-2)} [\alpha_n(\tau') - A(\tau')]] \right\} d\tau'$$

and

$$\frac{\partial}{\partial L} (f_3 + f_4) = R^2 \frac{\partial}{\partial H} (f_3 + f_4)$$

$$= R^2 \int_{-\infty}^{\tau} N' \left\{ -\frac{1}{R} \frac{\partial T_n(0, \tau')}{\partial H} \right.$$

$$\left. + 3 \frac{T_n(0, \tau')}{R^4} \right.$$

$$\left. - 2[(n-1)(n-2) + (n+2)(n+5) \left(\frac{n}{n+1}\right) R^{(n-5)} [\alpha_n(\tau') - A(\tau')]] \right\} d\tau'$$

Combining these results (III.44)

$$P_v(H=0, \tau) / \rho$$

$$= R^2 \int_{-\infty}^{\tau} N(\tau - \tau') \left\{ -\frac{1}{R} \frac{\partial T_n}{\partial H} + 3 \frac{T_n}{R^4} \right.$$

$$\left. - 2[(n-1)(n-2) + (n+2)(n+3) \left(\frac{n}{n+1}\right) R^{(n-5)} [\alpha_n(\tau') - A(\tau')]] \right\} d\tau'$$

$$\begin{aligned}
& + \int_{-\infty}^{\tau} N(\tau-\tau') \left\{ -3 \frac{T_n}{R^3} \right. \\
& + 2[(n-1)(n-2) + (n+2)(n+3) \left(\frac{n}{n+1} \right)] R'^{(n-2)} [\alpha_n(\tau') - A_n(\tau')] \Big\} d\tau' \\
& + \frac{n(2n+1)}{n+1} R^n \left(\frac{\dot{R}}{R} \right) (\alpha_n - A_n) \\
& + \dot{R} T_n(H=0, \tau) \\
& - R^n \int_R^{\infty} s^{-n} \left(\frac{\partial T}{\partial \tau} \right) ds \\
& - R^n \left(\frac{2n+1}{n+1} \right) \frac{\partial A}{\partial \tau}
\end{aligned}$$

The potential flow contributes to the total pressure field through p_p which was derived by Plesset to be

$$p_p(r = R, \theta, \phi, t) = \frac{\rho}{n+1} (R \ddot{a} + 3 \dot{R} \dot{a} + 2 \ddot{R} a) Y_n^m \quad (\text{A.24})$$

at $H = 0$.

Since this has the same angular dependence as p_v , an analogue to P_v is found to be

$$\frac{P_p(H=0, \tau)}{\rho} = \frac{1}{n+1} (R \ddot{a}_n + 3 \dot{R} \dot{a}_n + 2 \ddot{R} a_n) \quad (\text{A.24})$$

The unit normal to the surface, \underline{n} , also enters into the $O(\epsilon)$ boundary conditions

$$\underline{n} = \frac{R}{r} \underline{e}_r - \epsilon \frac{a_n}{r} \frac{\partial Y}{\partial \theta} \underline{e}_\theta - \epsilon \frac{a_n}{r \sin \theta} \frac{\partial Y}{\partial \phi} \underline{e}_\phi \quad (\text{A.25})$$

where \underline{e}_r , \underline{e}_θ and \underline{e}_ϕ are the unit vectors. The dynamic boundary conditions are

$$\underline{n} \times [\underline{g} \cdot \underline{n}] = 0 \quad (\text{A.26})$$

$$\underline{n} \cdot (\underline{g} \cdot \underline{n}) = \sigma \underline{\nabla} \cdot \underline{n} \quad (\text{A.27})$$

where the former condition is for zero tangential stress and the latter expresses the balance which must hold between any discontinuity in normal stress and surface tension forces. The total stress tensor \underline{g} , includes the isotropic pressure just calculated in p_p and p_v and the extra stress $\underline{\tau}$. The three components of the tangential stress condition are

$$r : 0 = 0$$

$$\theta : n_r \sigma_{\phi r} n_r + n_r \sigma_{\phi\phi} n_\phi - n_\phi \sigma_{rr} n_v = 0$$

$$\phi : n_r \sigma_{\theta r} n_r + n_r \sigma_{\theta\theta} n_\theta - n_\theta \sigma_{rr} n_r = 0$$

The potential flow contributes to the extra stress in the fluid through the rate-of-strain tensor for that flow field $\dot{\underline{\gamma}}^{(p)}$. (A.28)

$$\dot{\gamma}_{rr}^{(p)}(r,t) = -2 \left(\frac{n+2}{r}\right) \left(\frac{R}{r}\right)^{n+2} C_n(t) Y_n^m$$

$$\dot{\gamma}_{\theta\theta}^{(p)}(r,t) = 2 \left(\frac{1}{r}\right) \left(\frac{R}{r}\right)^{n+2} C_n(t) \left[-\left(\frac{1}{n+1}\right) \frac{\partial^2 Y}{\partial \epsilon^2} + Y\right]$$

$$\dot{\gamma}_{\phi\phi}^{(p)}(r,t) = 2 \left(\frac{1}{r}\right) \left(\frac{R}{r}\right)^{n+2} C_n(t)$$

$$\left\{ -\left(\frac{1}{n+1}\right) \frac{1}{\sin^2\theta} \frac{\partial^2 Y}{\partial \phi^2} + Y - \frac{\cot\theta}{n+1} \frac{\partial Y}{\partial \theta} \right\}$$

$$\dot{\gamma}_{r\theta}^{(p)} = \dot{\gamma}_{\theta r}^{(p)} = \frac{1}{r} \left(\frac{R}{r}\right)^{n+2} C_n(t) \frac{2(n+2)}{(n+1)} \frac{\partial Y}{\partial \theta}$$

$$\dot{\gamma}_{r\phi}^{(p)} = \dot{\gamma}_{\phi r}^{(p)} = \frac{1}{r} \left(\frac{R}{r}\right)^{n+2} C_n(t) \frac{2(n+2)}{(n+1)} \frac{1}{\sin\theta} \frac{\partial Y}{\partial \phi}$$

$$\dot{\gamma}_{\theta\phi}^{(p)} = \dot{\gamma}_{\phi\theta}^{(p)} = -\left(\frac{1}{n+1}\right) \left(\frac{1}{r}\right) \left(\frac{R}{r}\right)^{n+2} C_n(t)$$

$$\left\{ \frac{2}{\sin\theta} \frac{\partial^2 Y}{\partial \phi \partial \theta} - \frac{2 \cot\theta}{\sin\theta} \frac{\partial Y}{\partial \phi} \right\}$$

where the time dependent function $C_n(t)$ is defined as

$$C_n(t) = \dot{a}_n(t) + 2 a_n(t) \frac{\dot{R}(t)}{R(t)} \quad (\text{A.29})$$

The angular terms in curly brackets { } can be simplified using the identity for spherical harmonics

$$\frac{1}{\sin\theta} \frac{\partial}{\partial \theta} (\sin\theta \frac{\partial}{\partial \theta} Y_l^m) + \frac{1}{\sin^2\theta} \frac{\partial^2}{\partial \phi^2} Y_l^m = - (l+1) Y_l^m \quad (\text{III.13})$$

$$\frac{n \sigma_{\phi\phi}^n - n \sigma_{rr}^n}{\frac{1}{\sin\theta} \frac{\partial Y}{\partial \phi}} \quad (\text{A.31})$$

$$= \frac{n \sigma_{\theta\theta}^n - n \sigma_{rr}^n}{\frac{\partial Y}{\partial \theta}}$$

$$= \rho \left[\int_{-\infty}^{\tau} N' \frac{2R^2 \dot{R}}{R^3} d\tau' + p_0(r,t) \right] \left(-\frac{a}{R} \right)$$

$$- \left(-\frac{a}{R} \right) \left[- \int_{-\infty}^{\tau} N' \frac{4R^2 \dot{R}}{R^3} d\tau' + p_0(r,t) \right]$$

$$= - \left(\frac{a_n(\tau)}{R(\tau)} \right) 6 \int_{-\infty}^{\tau} N' \frac{\dot{R}(\tau')}{R(\tau')} d\tau'$$

These combine via (A.26) to yield the tangential stress condition, Equation (III.46).

$$\int_{-\infty}^{\tau} N(\tau-\tau') \left\{ 2(n+2) \left[\frac{\dot{a}_n(\tau')}{R(\tau')} + \frac{2a_n(\tau') \dot{R}(\tau')}{R^2(\tau')} \right] \right.$$

$$\left. - (n+1) \frac{T_n(H=0, \tau')}{R(\tau')} \right.$$

$$\left. + 2(2n+1) R^{(n-2)}(\tau') [\alpha_n(\tau') - A_n(\tau')] \right\} d\tau'$$

$$- 6(n+1) \frac{a_n(\tau)}{R(\tau)} \int_{-\infty}^{\tau} N(\tau-\tau') \frac{\dot{R}(\tau')}{R(\tau')} d\tau' = 0$$

The normal force condition at first order in ϵ reduces to only one stress component balancing the $O(\epsilon)$ surface tension force, but each must be evaluated at the deformed surface

$$\begin{aligned}
 n_t \sigma_{rr} \Big|_{n_r} & & (A.32) \\
 r = R + \epsilon a Y & \\
 & = -\sigma \left\{ \frac{a}{r^2} \left[\frac{1}{\sin \theta} \frac{\partial}{\partial \theta} (\sin \theta \frac{\partial Y}{\partial \theta}) \right. \right. \\
 & \quad \left. \left. + \frac{1}{\sin^2 \theta} \frac{\partial^2 Y}{\partial \phi^2} \right] + \frac{2a}{r^2} Y_n^m \right\} \Big|_{r = R + \epsilon a Y} \\
 & = \sigma \frac{a}{r^2} \Big|_{r = R + \epsilon a Y} (n-1)(n+2) Y_n^m
 \end{aligned}$$

The stress component is given by

$$\sigma_{rr} \Big|_{L = R + \epsilon a Y} = \sigma_{rr} \Big|_{H = 0} + \epsilon a_n Y_n^m \frac{\partial}{\partial L} \sigma_{rr} \Big|_{H = 0} \quad (A.33)$$

The terms needed at the undeformed surface are those that are first order in ϵ . (A.34)

$$\sigma_{rr} \Big|_{H = 0} = \int_{-\infty}^{\tau} N' [\dot{\gamma}_{rr}^{(v)} + \dot{\gamma}_{rr}^{(p)}] d\tau' + p_v + p_p$$

$$\begin{aligned}
 &= \rho \int_{-\infty}^{\tau} 2N' \left(\frac{\partial T_n}{\partial L} - \frac{\partial^2 B_n}{\partial L^2} \right) \Big|_{H=0} \\
 &- \left(\frac{n+2}{L} \right) \left(\frac{R}{L} \right)^{n+2} \left(\dot{a}_n + 2a_n \frac{\dot{R}}{R} \right) \Big|_{H=0} \} Y_n^m d\tau' \\
 &+ \{ P_v(H=0, \tau) + \frac{1}{n+1} (R\ddot{a}_n + 3\dot{R}\dot{a}_n + 3\ddot{R}a_n) \} Y_n^m \\
 &= \rho \int_{-\infty}^{\tau} 2N' \{ -n(2n+1)R^{(n-2)} (\alpha_n - A_n) \\
 &- \left(\frac{n+2}{R} \right) (\dot{a}_n + 2a_n \frac{\dot{R}}{R}) \} Y_n^m d\tau' \\
 &+ \{ P_v(H=0, \tau) + \frac{1}{n+1} (R\ddot{a}_n + 3\dot{R}\dot{a}_n + 2\ddot{R}a_n) \} Y_n^m
 \end{aligned}$$

The first term can be replaced by an expression derived from the tangential condition (III.46).

The contribution to the stress resulting from the surface deformation is

$$a_n Y_n^m L^2 \frac{\partial}{\partial H} \left\{ \rho \int_{-\infty}^{\tau} N' \left(-\frac{4\dot{R}\dot{R}^2}{L^3} \right) d\tau' + p_0 \right\} \tag{A.35}$$

at $H = 0$, where p_0 is the pressure field from the spherical flow given by

$$\begin{aligned}
 p_0(H, \tau) &= P_0(\tau) + \\
 &\rho \left[(R^2\ddot{R} + 2R\dot{R}^2)/L - \frac{1}{2} \dot{R}^2 R^3/L^3 \right]
 \end{aligned} \tag{A.36}$$

Contribution (A.35) is expressed in terms of a_n , R and derivatives as

$$a_n(\tau) \left\{ 12 \rho L^2 \int_{-\infty}^{\tau} N' \left(\frac{\dot{R}(\tau')}{R^4(\tau')} \right) d\tau' \right. \\ \left. - \rho \ddot{R}(\tau) \right\} Y_n^m(\theta, \phi) \quad (\text{A.35}')$$

Combining (A.32), (A.34) and (A.35) the equation of motion for $a_n(\tau)$ results (III.45)

$$\frac{1}{n+1} R(\tau) \ddot{a}_n(\tau) + \frac{3}{n+1} \dot{R}(\tau) \dot{a}_n(\tau) \\ - 2(n-1)(n+2) \int_{-\infty}^{\tau} N' \left[\frac{\dot{a}_n(\tau')}{R(\tau')} \right] d\tau' \\ + \left(-\frac{n-1}{n+1} \right) \ddot{R}(\tau) a_n(\tau) - \\ - 4(n-1)(n+2) \int_{-\infty}^{\tau} N' \left[\frac{a_n(\tau') \dot{R}(\tau')}{R^2(\tau')} \right] d\tau' \\ + 6n(n+1) \frac{a_n(\tau)}{R(\tau)} \int_{-\infty}^{\tau} N' \frac{\dot{R}(\tau')}{R(\tau')} d\tau' \\ - 12 a_n(\tau) R^2(\tau) \int_{-\infty}^{\tau} N' \left[\frac{\dot{R}(\tau')}{R^4(\tau')} \right] d\tau' \\ + (n-1)(n+2) \frac{\sigma/\rho}{R^2(\tau)} a_n(\tau)$$

$$+ n(n+1) \int_{-\infty}^{\tau} N' \left[\frac{T_n(H=0, \tau')}{R(\tau')} \right] d\tau'$$

$$+ P_{v,n}(H=0, \tau) = 0$$

A.3 Viscous Limit

A necessary, though not sufficient, condition for the validity of these results, (III.41), (III.45) and (III.46) is their reduction to the expressions for a purely viscous fluid derived by Prosperetti (III.27), (III.32) and (III.34). This Newtonian limit should obtain for the special choice of memory function

$$N(t) = \mu \delta(t) \quad \text{Newtonian} \quad (\text{A.36})$$

where $\delta(t)$ is the Dirac delta function. This relaxation modulus will serve to reduce the time integrals to the value of the integrand at the time when the argument of the delta function is zero.

$$\int_{-\infty}^{\tau} \mu \delta(\tau - \tau') f(\tau') d\tau' = \mu f(\tau) \quad (\text{A.37})$$

Thus, the distinction between Eulerian and Lagrangian time integrals vanishes since the variation of geometric parameters such as $R(t)$ over past times is no longer relevant.

The simplifications that the Newtonian stress relation allow in the model system are substantial. For the T-equation in the form of (III.41), the elastic integrals, those multiplied by G_0 , are identically zero. The cancellation of terms in the integrands I_1 , I_2 , and I_3 which occurs to leave only the term multiplied by ν in (III.41) is best seen in expression (A.16). The distinction between terms like

$$\frac{1}{L^2} \int_{-\infty}^{\tau} N(\tau-\tau') X_n(H, \tau') L'^{(n-2)} d\tau'$$

and

$$L \int_{-\infty}^{\tau} N(\tau-\tau') X_n(H, \tau') L'^{(n-5)} d\tau'$$

disappears for the purely viscous case since both are now equal to

$$\mu X_n(H, \tau) L^{(n-4)}$$

Terms containing X_n and Z_n cancel completely, and only the terms involving T_n remain. It is then straightforward to transform the Lagrangian purely viscous T-equation to the Eulerian result (III.27).

$$\frac{\partial T}{\partial t} + \frac{\partial}{\partial r} \left[\dot{R} \left(\frac{R}{r} \right)^2 T \right] = \nu \left[\frac{\partial^2 T}{\partial r^2} - n(n+1) \frac{T}{r^2} \right]$$

The tangential stress condition (III.46) is even more easily reduced to the desired viscous limit. The distinction between terms such as

$$\frac{s}{R} \int_{-\infty}^{\tau} N' \frac{\dot{R}'}{R'} d\tau'$$

and

$$\int_{-\infty}^{\tau} N' \frac{s' \dot{R}'}{R'^2} d\tau'$$

vanishes in this case and (III.32) obtains directly.

The purely viscous normal stress balance is more difficult to produce from the non-Newtonian expression. First, P_v (III.44) must be obtained for the Newtonian modulus in Eulerian coordinates, then the result can be employed in the amplitude equation (III.45). In equation (III.44) most of the terms in the two time integrals will cancel in the viscous limit. When there is no externally imposed flow, the result is

$$P_v(H=0, \tau) / \rho = P_v(v=R, t) / \rho \quad \text{viscous} \quad (\text{A.38})$$

$$= -v \frac{\partial T}{\partial r} + \frac{n(2n+1)}{n+1} R^n \left(\frac{\dot{R}}{R}\right) \alpha_r$$

$$+ \dot{R} T_n(R, t) - R^n \int_R^\infty S^{-n} \left[\frac{\partial T}{\partial t} + \dot{R} \left(\frac{R}{S}\right)^2 \frac{\partial T}{\partial S} \right] dS$$

Using the viscous T-equation (III.27)

$$\frac{\partial T}{\partial t} = - \frac{\partial}{\partial r} \left[\dot{R} \left(\frac{R}{r}\right)^2 T \right] + v \left\{ \frac{\partial^2}{\partial r^2} - n(n+1) \frac{T}{r^2} \right\}$$

and spatially integrating by parts

$$P_v(r=R, t) / \rho$$

$$= n \left(\frac{\dot{R}}{R}\right) \int_0^\infty \left[\left(\frac{R}{S}\right)^2 - 1 \right] \left(\frac{R}{S}\right)^n T(s, t) dS$$

$$+ n v \frac{T(R, t)}{R}$$

which is equivalent to (III.35). With this result the viscous equation (III.34) emerges from (III.46).

APPENDIX B : $O(\epsilon^2)$ TermsB.1 Introduction

The validity of the present analysis, which is restricted to "small ϵ ", obviously depends upon that small parameter. One way to evaluate the radius of convergence of the analysis is through experimental trials and these seem to indicate good agreement for deformations which are substantial fractions of the overall bubble radius (see Figures 24-27). Previously published comparisons of the nonlinear analysis of Chapman and Plesset (1971) with linearized results, these for inviscid fluids, are encouraging since they show good agreement until the final stages of collapse. Analysis can also give some estimate of the range of validity of a linearization without the need for solution of the full, nonlinear, problem through the generation of the neglected terms and determining the conditions under which they are small compared to the terms which are retained.

The nonlinear terms which are dropped in the derivation of the T-equation (III.41) from the exact vorticity equation (22) are terms of second order in ϵ . Such second order terms are also quadratic in the spherical harmonics, which removes the separability of the equation into an (r,t) -dependent function and an angularly-dependent one. This, in turn, prevents the manipulation which totally removed the angular dependence from the final expression (see equations A.5 & A.13) and the resulting independence of this equation from those for any other value of the index n . Thus, the explicit evaluation of the next term in the expansions for velocity or pressure (equations III.16,

17) is considerably more complicated than that for the $O(\epsilon^1)$ term. Since both the full nonlinear problem and the $O(\epsilon^2)$ problem are so difficult, the error introduced by the nonlinear terms is estimated by evaluating them for the values obtained from the linear analysis.

B.2 Convection and Inertia

The nonlinear terms in the LHS of the vorticity equation which were neglected are

$$(\underline{v}_v + \underline{v}_p) \cdot \underline{\nabla} \omega - \omega \cdot \underline{\nabla} (\underline{v}_v + \underline{v}_p) \quad (\text{B.1})$$

and represent convected, inertial phenomena. They also bring the potential velocity field \underline{v}_p into the analysis for vorticity. The expressions for each component of the velocity and vorticity are given in Section III and again in Appendix A (III.19, III.28, A.1, III.21, A.4). A double summation over the lower index on the spherical harmonics is now necessary. A new symbolism is adopted to insure the explicit retention of both values. Let "k" be one subscript and "l" the second and let \underline{v} be the total $O(\epsilon)$ velocity.

$$\underline{v} = \underline{v}_v + \underline{v}_p \quad (\text{B.2})$$

Then, this means

$$(\underline{v}_k)_r = \left[\left(\frac{R}{r} \right)^{k+2} \left(\dot{a}_k + a_k \frac{\dot{R}}{R} \right) + \left(T_k - \frac{\partial R_k}{\partial r} \right) \right] Y_k^m(\theta, \phi) \quad (\text{B.3})$$

For convenience, the potential contribution is represented through

$$C_k(r,t) = \left(\frac{R}{r}\right)^{k+2} \left(\dot{a}_k + a_k \frac{\dot{R}}{R}\right) \quad (\text{B.4})$$

This symbolism can be used to express the $O(\epsilon^2)$ terms in the Eulerian frame as

$$[\underline{v}_k \cdot \nabla \omega_\ell]_r = \quad (\text{B.5})$$

$$\left[\frac{B_k}{r} + \left(\frac{1}{k+1}\right) C_k \right] \frac{T_\ell}{r^2 \sin \theta}$$

$$\left[\frac{\partial Y_k}{\partial \theta} \frac{\partial Y_\ell}{\partial \phi} - \frac{\partial Y_k}{\partial \phi} \frac{\partial Y_\ell}{\partial \theta} \right]$$

$$[\underline{\omega}_k \cdot \nabla v_\ell]_r = \quad (\text{B.6})$$

$$\left[\frac{T_k}{r^2 \sin \theta} \right] \left[\left(T_\ell - \frac{\partial B_\ell}{\partial r} \right) + \frac{B_\ell}{r} + C_\ell \right]$$

$$\left[\frac{\partial Y_k}{\partial \phi} \frac{\partial Y_\ell}{\partial \phi} - \frac{\partial Y_k}{\partial \phi} \frac{\partial Y_\ell}{\partial \theta} \right]$$

$$[v_k \cdot \nabla \omega_l]_\theta =$$

(B.7)

$$\begin{aligned} & [(T_k - \frac{\partial B_k}{\partial r}) + C_k] Y_k \left[\frac{1}{\sin \theta} \frac{\partial}{\partial r} \left(\frac{T_l}{r} \right) \frac{\partial Y_l}{\partial \phi} \right] \\ & - \left(\frac{B_k}{r} + \left(\frac{1}{k+1} \right) C_k \right) \left[\frac{T_l}{r^2} \right] \left[\frac{\partial Y_k}{\partial \theta} \frac{\partial}{\partial \theta} \left(\frac{1}{\sin \theta} \frac{\partial Y_l}{\partial \phi} \right) + \right. \\ & \left. \frac{1}{\sin \theta} \frac{\partial Y_k}{\partial \phi} \left(\frac{1}{\sin^2 \theta} \frac{\partial^2 Y_l}{\partial \phi^2} + \cot \theta \frac{\partial Y_l}{\partial \theta} \right) \right] \end{aligned}$$

$$[\omega_k \cdot \nabla v_l]_\theta =$$

(B.8)

$$\begin{aligned} & \left[\frac{T_k}{r^2 \sin \theta} \right] \frac{\partial Y_k}{\partial \phi} \\ & \{ [(T_l - \frac{\partial B_l}{\partial r}) + C_l] Y_l - \left[\frac{B_l}{r} + \left(\frac{1}{l+1} \right) C_l \right] \frac{\partial^2 Y_l}{\partial \theta^2} \} \\ & + \left[\frac{T_k}{r^2 \sin \theta} \right] \frac{\partial Y_k}{\partial \theta} \\ & \left\{ \left[\frac{B_l}{r} + \frac{C_l}{l+1} \right] \left(\cot \theta \frac{\partial Y_l}{\partial \phi} - \frac{\partial^2 Y_l}{\partial \theta \partial \phi} \right) \right\} \end{aligned}$$

$$[y_k \cdot \nabla \omega_l]_\phi = \quad (B.9)$$

$$\begin{aligned} & [(T_k - \frac{\partial B_k}{\partial r}) + C_k] Y_k [-\frac{\partial}{\partial r} (\frac{T_l}{r}) \frac{\partial Y_l}{\partial \theta}] \\ & + \{ \frac{B_k}{r} + (\frac{1}{k+1}) C_k \} (\frac{T_l}{r^2}) \\ & [\frac{\partial Y_k}{\partial \theta} \frac{\partial^2 Y_l}{\partial \theta^2} + \frac{1}{\sin^2 \theta} \frac{\partial Y_k}{\partial \phi} (\frac{\partial^2 Y_l}{\partial \theta \partial \phi} - \cot \theta \frac{\partial Y_l}{\partial \phi})] \end{aligned}$$

$$[\omega_k \cdot \nabla y_l]_\phi = \quad (B.10)$$

$$\begin{aligned} & [\frac{T_k}{r^2}] \{ -\frac{1}{\sin \theta} \frac{\partial Y_k}{\partial \phi} [(\frac{B_l}{r} + \frac{C_l}{l+1}) \frac{\partial}{\partial \theta} \frac{1}{\sin \theta} \frac{\partial Y_l}{\partial \phi}] \\ & + \frac{\partial Y_k}{\partial \theta} [(\frac{B_l}{r} + \frac{C_l}{l+1}) (\frac{\partial^2 Y_l}{\partial \phi^2} + \cot \theta \frac{\partial Y_l}{\partial \theta}) \\ & - (T_l - \frac{\partial B_l}{\partial r} + C_l) Y_l \} \end{aligned}$$

A tractable expression, and one which is still meaningful, results if axisymmetry is assumed and only one mode is present, e.g. $k = l = 2$. The r - and θ -components of the cross terms are identically zero and the ϕ -term is (B.9, 10)

$$\begin{aligned}
& [\underline{v}_k \cdot \nabla \omega_k]_\phi - [\omega_k \cdot \nabla \underline{v}_k]_\phi \\
&= (T_k - \frac{\partial B_k}{\partial r} + C_k) Y_k (-\frac{1}{r} \frac{\partial T_k}{\partial r} + \frac{T_k}{r^2}) \frac{\partial Y_k}{\partial \theta} \\
&+ (\frac{B_k}{r} + \frac{C_k}{k+1}) (\frac{T_k}{r^2}) \frac{\partial Y_k}{\partial \theta} \frac{\partial^2 Y_k}{\partial \theta^2} \\
&- (\frac{T_k}{r}) (\frac{B_k}{r} + \frac{C_k}{k+1}) \frac{\partial Y_k}{\partial \theta} \cot \theta \frac{\partial Y_k}{\partial \theta} \\
&+ (T_k - \frac{\partial B_k}{\partial r} + C_k) (\frac{T_k}{r^2}) Y_k \frac{\partial Y_k}{\partial \theta} \\
&= (T_k - \frac{\partial B_k}{\partial r} + C_k) (\frac{2T_k}{r^2} - \frac{1}{r} \frac{\partial T_k}{\partial r}) Y_k \frac{\partial Y_k}{\partial \theta} \\
&+ (\frac{B_k}{r} + \frac{C_k}{k+1}) (\frac{T_k}{r^2}) (\frac{\partial^2 Y_k}{\partial \theta^2} - \cot \theta \frac{\partial Y_k}{\partial \theta}) \frac{\partial Y_k}{\partial \theta}
\end{aligned}$$

From the sample calculation of Appendix C.2 values for each of these functions can be assigned and the relative magnitude of the convection terms evaluated, e.g. at $r = R$ (B.11)

Step #10: time = 2.50×10^{-5} sec

$$R = 2.42 \times 10^{-1} \text{ cm}$$

$$\dot{R} = 1.47 \times 10^3 \text{ cm/sec}$$

$$a = 9.5 \times 10^{-2} \text{ cm}$$

$$\dot{a} = -1.863 \times 10^3 \text{ cm/sec}$$

$$\alpha_2 = -8.70 \times 10^3$$

$$\frac{\partial T}{\partial r}(R) = -4 \times 10^7 \text{ sec}^{-1}$$

$$T(R) = -1.14 \times 10^3 \text{ cm/sec}$$

Step #11: time = 2.75×10^{-5} sec

$$R = 2.46 \times 10^{-1} \text{ cm}$$

$$\dot{R} = 1.41 \times 10^3 \text{ cm/sec}$$

$$\dot{a} = 9.1 \times 10^{-2} \text{ cm}$$

$$\dot{a} = -1.943 \times 10^2 \text{ cm/sec}$$

$$\alpha_2 = -8.805 \times 10^3$$

$$\frac{\partial T}{\partial t}(R) = -1 \times 10^8 \text{ sec}^{-1}$$

$$T(R) = -1.20 \times 10^3 \text{ cm/sec}$$

Also at $r = R$

$$T_2 - \frac{\partial B_2}{\partial r} = 0$$

$$C_2 = \dot{a} + 2a \frac{\dot{R}}{R} \sim 10^3 \text{ cm/sec}$$

$$\frac{B_2}{R} = \frac{2n+1}{n+1} R^{n-1} \alpha_2 \sim 4 \times 10^3$$

Thus the factors in the second order expression are

$$\left(T_2 - \frac{\partial B_2}{\partial r} + C_2 \right) \Big|_{r=R} \sim 10^3 \text{ cm/sec}$$

$$\left(2 \frac{T_2}{R} - \frac{1}{R} \frac{\partial T_2}{\partial r} \right) \Big|_{r=R} \sim 2 \times 10^6 \text{ cm}^{-1} \text{sec}^{-1}$$

(B.12)

$$\left(\frac{B_2}{R} + \frac{C_2}{3} \right) \Big|_{r=R} \sim 4 \times 10^3 \text{ cm/sec}$$

$$\left(\frac{T_2}{R^2} \right) \Big|_{r=R} \sim 2 \times 10^4 \text{ sec}^{-1} \text{cm}^{-1}$$

$$[Y_2 \cdot \nabla \omega_2]_\phi - (\omega_2 \cdot \nabla Y_2)_\phi$$

$$\sim \{ 2 \times 10^{11} (Y_2 \frac{\partial Y_2}{\partial r}) \}$$

(B.13)

$$+ 8 \times 10^7 \left(\frac{\partial^2 Y_2}{\partial \theta^2} - \cot \theta \frac{\partial Y_2}{\partial \theta} \right) \frac{\partial Y_2}{\partial \theta} \text{ sec}^{-2}$$

These second terms are to be compared with the inertial terms at first order in ϵ which are

$$\left\{ \frac{1}{r} \frac{\partial T}{\partial t} + \frac{1}{r} \frac{\partial}{\partial r} \left[\dot{R}^2 \left(\frac{R}{r} \right)^2 T_2 \right] \right\} \frac{\partial Y_2}{\partial \theta} \quad (\text{B.14})$$

$$= \left[\frac{1}{R} \frac{\partial T}{\partial t} (R) + \frac{1}{R} \left(\dot{R} \frac{\partial T}{\partial r} - 2\dot{R} \frac{T}{R} \right) \right] \frac{\partial Y_2}{\partial \theta}$$

Numerical data gives this expression (B.14) a value of about $|3 \times 10^{11}|$ $\partial Y_2 / \partial \theta$ at $r = R$. For these terms, at first order in ϵ , to dominate the nonlinear, second order terms of (B.13)

$$\epsilon ("B.14") > \epsilon^2 ("B.13") \quad (\text{B.15})$$

or numerically

$$\epsilon < \frac{|3 \times 10^{11}|}{|2 \times 10^{11}|} \quad (\text{B.16})$$

To arrive at this result, the common factor $\partial Y_2 / \partial \theta$ has been cancelled and the other angular terms in (B.13) neglected since they are $O(10^\circ)$ or less; they consist of combinations of sine and cosine functions. For large \dot{R} values, as in this case, these inertial terms are dominated by the contributions of C_2 and $\partial T / \partial r$. When this occurs the requirement on ϵ becomes

$$\epsilon^2 \left(\dot{a}_2 + 2a_2 \frac{\dot{R}}{R} \right) \frac{1}{R} \frac{\partial T}{\partial r} < \epsilon \left(\frac{2}{R} \dot{R} \frac{\partial T}{\partial r} \right)$$

or

$$\epsilon \left(\frac{\dot{a}_2}{2\dot{a}_2} + \frac{\dot{a}_2}{R} \right) < 1 \quad (\text{B.17})$$

B.3 Non-Newtonian Nonlinearities

A second instance for which the importance of second order terms must be evaluated does not arise from a straightforward expansion of existing terms in the vorticity equation, but from a particular choice of constitutive model for the stress. Cross terms can arise from the nonlinearities of convection, co-deformational or co-rotational terms.

One method by which to approximate these contributions while maintaining the form of the previous results is to employ quasi-linear expressions, in the sense of Bird, Armstrong and Hassager (Chapter 7). A Taylor series expansion in convected, co-rotational or co-deformational coordinates can be employed to approximate the difference in stress each formalism would predict. In the integral constitutive model the strain rate at time τ' , $\dot{\underline{\gamma}}(\tau')$, or its equivalent can be replaced by

$$\begin{aligned} \dot{\underline{\gamma}}_{\text{convected}}(\tau') &= \dot{\underline{\gamma}}(\tau) + (\tau - \tau') \frac{D\dot{\underline{\gamma}}}{Dt}(\tau) \\ &= \dot{\underline{\gamma}}(\tau) + (\tau - \tau') \left(\frac{\partial \dot{\underline{\gamma}}}{\partial \tau} + \epsilon \underline{v} \cdot \nabla \dot{\underline{\gamma}} \right) \Big|_{\tau=\tau} \end{aligned} \tag{B.18}$$

in the convected case. The present $O(\epsilon^1)$ model already incorporates an evaluation scheme which is better than the first two terms in the second expression of (B.18) since the actual value of strain rate at past times is evaluated and included in the analysis. If this evaluation is termed $\dot{\underline{\gamma}}_{\text{present}}(\tau')$ then another approximation to the convected strain rate at past times is

$$\begin{aligned} \dot{\underline{\underline{\gamma}}}_{\text{convected}}(\tau') &= \dot{\underline{\underline{\gamma}}}_{\text{present}}(\tau') \\ &+ \varepsilon(\tau - \tau') \underline{\underline{v}} \cdot \nabla \dot{\underline{\underline{\gamma}}} \end{aligned} \quad (\text{B.19})$$

Similar expressions arise when co-rotational contributions are included

$$\begin{aligned} \dot{\underline{\underline{\gamma}}}_{\text{co-rot}}(\tau') &= \dot{\underline{\underline{\gamma}}}(\tau) + \varepsilon(\tau - \tau') \frac{\Delta}{\Delta t} \dot{\underline{\underline{\gamma}}}(\tau) \\ &= \dot{\underline{\underline{\gamma}}}_{\text{convected}}(\tau') \\ &+ \varepsilon(\tau - \tau') \frac{1}{2} [(\underline{\underline{\omega}} \cdot \dot{\underline{\underline{\gamma}}}) - (\dot{\underline{\underline{\gamma}}} \cdot \underline{\underline{\omega}})] \end{aligned} \quad (\text{B.20})$$

for the vorticity tensor $\underline{\underline{\omega}}$. And also when co-deformational contributions are considered

$$\begin{aligned} \dot{\underline{\underline{\gamma}}}_{\text{co-def}}(\tau') \\ &= \dot{\underline{\underline{\gamma}}}_{\text{convected}}(\tau') \\ &+ \varepsilon(\tau - \tau') [(\nabla \underline{\underline{v}})^T \cdot \dot{\underline{\underline{\gamma}}} + \dot{\underline{\underline{\gamma}}} \cdot (\nabla \underline{\underline{v}})] \end{aligned} \quad (\text{B.21})$$

These expansions are linear in time and can only be accurate as long as the time derivatives do not change sign.

All of these instantaneous strain rates will be integrated over time in the same stress expression. Thus, if the instantaneous difference between the present strain expression and those including

convected, co-rotational and co-deformational contributions is small, the resulting stress differences will also be small. This contrasts sharply with any comparison between purely viscous and viscoelastic stresses because they cannot be validly approximated by taking only taneous strain rates into account.

By reverting to the Taylor series expansion for the strain rate as presently employed, three terms emerge which must be less than the present strain rate

$$\Delta \dot{\underline{\underline{Y}}}_{\text{convected}}, \Delta \dot{\underline{\underline{Y}}}_{\text{co-rotational}}$$

$$\text{and } \Delta \dot{\underline{\underline{Y}}}_{\text{co-deformational}} \quad (\text{B.22})$$

$$< \dot{\underline{\underline{Y}}}_{\text{present}} = \dot{\underline{\underline{Y}}}(\tau) + (\tau - \tau') \frac{\partial}{\partial \tau} \dot{\underline{\underline{Y}}}(\tau)$$

where

$$\Delta \dot{\underline{\underline{Y}}}_{\text{convected}} = \epsilon(\tau - \tau') \underline{\underline{v}} \cdot \nabla \dot{\underline{\underline{Y}}}$$

$$\Delta \dot{\underline{\underline{Y}}}_{\text{co-rot}} = \frac{1}{2} \epsilon(\tau - \tau') [(\underline{\underline{\omega}} \cdot \dot{\underline{\underline{Y}}}) - (\dot{\underline{\underline{Y}}} \cdot \underline{\underline{\omega}})]$$

$$\Delta \dot{\underline{\underline{Y}}}_{\text{co-def}} = \epsilon(\tau - \tau') [(\nabla \underline{\underline{v}})^T \cdot \dot{\underline{\underline{Y}}} + \dot{\underline{\underline{Y}}} \cdot (\nabla \underline{\underline{v}})]$$

The convected difference terms can be represented by the (rr) component

$$\begin{aligned}
(\mathbf{v} \cdot \nabla \dot{\mathbf{Y}})_{rr} &= v_r \frac{\partial}{\partial r} \dot{Y}_{rr} \\
&+ \frac{v_\theta}{r} \frac{\partial}{\partial \theta} \dot{Y}_{rr} + \frac{v_\phi}{r \sin \theta} \frac{\partial}{\partial \phi} \dot{Y}_{rr} \\
&- 2 \left(\frac{v_\theta}{r} \right) \dot{Y}_{r\theta} - 2 \left(\frac{v_\phi}{r} \right) \dot{Y}_{r\phi}
\end{aligned} \tag{B.23}$$

Combining this expression with those for the full velocity vector and rate of strain tensor of Appendix A, the derivatives are all on the order of the particular strain component divided by the local radius, e.g.

$$\begin{aligned}
\frac{\partial}{\partial r} (\dot{Y}_{rr}) &= 2 \left[\frac{\partial^2}{\partial r^2} (T - \frac{\partial B}{\partial r}) \right. \\
&\left. + \frac{2(k+2)(k+3)}{r^2} \left(\frac{R}{r} \right)^{k+2} C_k \right] Y_k
\end{aligned} \tag{B.24}$$

emerges from (A.9) and (A.28). It can also be shown from the definition of B_n (A.2) and (A.13) and (A.14) that

$$\begin{aligned}
\frac{\partial^2}{\partial r^2} (T - \frac{\partial B}{\partial r}) &= -k(k-1)(k-2) X_k r^{k-3} \\
&+ (k+1)(k+2)(k+3) Z_k r^{-(k+4)} \\
&+ \frac{T}{r^2} \frac{k(k^2+3k+1)}{2k+1}
\end{aligned} \tag{B.25}$$

which means that

$$\frac{\partial}{\partial r} (\dot{\gamma}_{rr}) \sim \frac{\dot{\gamma}_{rr}}{r} \quad (\text{B.26})$$

In the evaluation of the present strain rate the (rr) component is

$$\begin{aligned} \dot{\gamma}_{rr}^{(v)} &= 2 \left(\frac{\partial T}{\partial r} - \frac{\partial^2 B}{\partial r^2} \right) Y_n^m \quad (\text{A.9}) \\ &= -2[n(n-1)r^{n-2}X_n + (n+1)(n+2)r^{-(n+2)}Z_n] \end{aligned}$$

from (A.14). The sample calculation assigns numerical values to the terms in (B.22), (B.23), (B.26) and (A.9), at $r = R$ (see B.11)

$$|\dot{\gamma}| \doteq 1.75 \times 10^5 \text{ sec}^{-1}$$

$$\frac{\partial \dot{\gamma}}{\partial r} \doteq 8.4 \times 10^8 \text{ sec}^{-2}$$

(B.27)

$$R \doteq 2.4 \times 10^{-1} \text{ cm}$$

$$|\dot{\gamma}| \doteq 10^3 \text{ sec/sec}$$

For this case, the convected contribution to the strain rate is small when

$$\frac{\Delta \dot{\gamma}_{\text{convected}}}{\dot{\gamma}_{\text{present}}} = \frac{\varepsilon(\tau - \tau')(10^3) \frac{1.75 \times 10^5}{2.4 \times 10^{-1}}}{1.75 \times 10^5 + (\tau - \tau')(8.4 \times 10^3)} < 1 \quad (\text{B.28})$$

which is true for all $\tau' < \tau$ when

$$\varepsilon < 1.15 \quad (\text{B.28}^1)$$

A similar analysis can be carried out for the co-rotational terms.
For the axisymmetric case the necessary calculations show that

$$\underline{\underline{\omega}} = 2 \begin{bmatrix} 0 & \omega_{\phi} & 0 \\ -\omega_{\phi} & 0 & 0 \\ 0 & 0 & 0 \end{bmatrix}$$

(B.29)

$$\underline{\underline{\dot{\gamma}}} = \begin{bmatrix} \dot{\gamma}_{rr} & \dot{\gamma}_{r\theta} & 0 \\ \dot{\gamma}_{r\theta} & \dot{\gamma}_{\theta\theta} & 0 \\ 0 & 0 & \dot{\gamma}_{\phi\phi} \end{bmatrix}$$

$$\underline{\underline{E}} = \frac{1}{2} \{ (\underline{\underline{\omega}} \cdot \underline{\underline{\dot{\gamma}}}) - (\underline{\underline{\dot{\gamma}}} \cdot \underline{\underline{\omega}}) \} \quad (\text{B.30})$$

has only four non-zero terms, which are given by

$$E_{rr} = 2 \omega_{\phi} \dot{\gamma}_{r\phi} = -E_{\theta\theta} \quad (\text{B.31})$$

$$E_{r\theta} = E_{\theta r} = \omega_{\phi} (\dot{\gamma}_{\theta\theta} - \dot{\gamma}_{rr})$$

The expressions for the vorticity tensor (A.4) show that

$$\omega_{\phi} \sim \frac{T}{r} \quad (\text{B.28})$$

And thus the ϵ condition for co-rotation becomes

$$\frac{\epsilon(\tau - \tau') \left| \frac{T}{r} \right| \left| \frac{\dot{\gamma}}{r} \right|}{\dot{\gamma} + (\tau - \tau') \frac{\partial \dot{\gamma}}{\partial \tau}} < 1 \quad (\text{B.29})$$

which numerically implies, for this case

$$\epsilon < 0.96 \quad (\text{B.29}^1)$$

Finally, for the co-deformational formalism the only complication is the relevance of both the potential and v-velocity fields. The velocity gradient consists of components of the form

$$\nabla_{\underline{v}} \sim 0 \left(\frac{B}{r^2} + \frac{C}{r} \right) \quad (\text{B.30})$$

and the ϵ -condition emerges as

$$\frac{\epsilon(\tau-\tau')\left(\left|\frac{B}{R^2}\right| + \left|\frac{C}{R}\right|\right)|\dot{\gamma}|}{\dot{\gamma} + (\tau-\tau')\frac{\partial\dot{\gamma}}{\partial\tau}} < 1 \quad (\text{B.31})$$

or

$$\epsilon < 0.8 \quad (\text{B.31}^1)$$

B.4 Amplitude Equations

The inaccuracy of the linear approximation applies to the non-Newtonian expressions in the boundary conditions just as it did for the vorticity equation. The results are the same as for T, since the same stress expressions are used to evaluate these quantities at the surface. However there is one place where these $O(\epsilon^2)$ terms could become important for the boundary conditions in addition to those for the T-equation. The unit normal to the surface used to formulate these conditions is

$$\underline{n} = \frac{r}{R} \underline{e}_r + \epsilon \frac{\frac{a}{n}}{r} \frac{\partial Y}{\partial \theta} \underline{e}_\theta - \epsilon \frac{\frac{a}{n}}{\sin \theta} \frac{\partial}{\partial \phi} \underline{e}_\phi$$

The correction to this expression at second order in ϵ is

$$- \frac{\epsilon^2}{2} \left(\frac{\frac{a}{n}}{r} \right)^2 \left[\left(\frac{\partial Y}{\partial \theta} \right)^2 + \left(\frac{1}{\sin \theta} \frac{\partial Y}{\partial \phi} \right)^2 \right] \quad (\text{B.32})$$

Thus the correction will be small if

$$\epsilon < 2 \frac{R}{a_n} \quad (\text{B.33})$$

or

$$\epsilon < 5 \quad (\text{B.33}^1)$$

for these numerical values.

APPENDIX C

C.1 Method of Solution

The system of equations governing the toroidal field $T_n(H, \tau)$ and the nonspherical amplitude a_n can be solved through a series of relatively straightforward finite difference calculations combined with linear algebraic techniques. The basic procedure, which allows simultaneous solution without iteration begins with the calculation of a "particular" and a "homogeneous" solution to the vorticity equation for T_n . The correct linear combination of these solutions is determined using both the amplitude equations and finite difference approximations to the nonspherical velocity and acceleration. A linear system of three equations is solved which determine amplitude, velocity and the proper linear combination simultaneously. Internal consistency, i.e. convergence, of the solution was checked by systematic variation of numerical parameters and algorithms within each program segment.

The symbolism employed reflects the restrictions of computer output and also the discretization of continuous functions performed in applying finite difference approximations. Spatial variation is signified by the index "I" and temporal dependence by a second index "J". The spatial grid was generated by specifying the Lagrangian coordinate $H(I)$ as a geometric series. An initial H value was specified to be H_1 and a ratio ρ_H was also chosen s.t.

$$\frac{H(I+1) - H(I)}{H(I) - H(I-1)} = \rho_H \quad (C.1)$$

where $H(1) = H_1$

and $H_0 = 0$

The ratio ρ_H was less than two (2.0), since this was found to be necessary for good approximations of spatial derivatives, and greater than unity. This lower bound served to concentrate the spatial points in the vicinity of the bubble surface while still allowing relatively few steps to span a large spatial range. This large range is desirable for the approximation of the integral term α_n (see Equation III.30)

$$\alpha_n = \int_R^{\infty} S^{-n} T(S,t) dS \quad (C.2)$$

$$= \int_R^{r_{\max}} S^{-n} T(S,t) dS$$

Trial and error calculations demonstrated that, while the value of r_{\max} necessary for convergence is not large, it would require hundreds of equally spaced steps of H_1 to reach that value when H_1 is small enough to insure good approximation of derivatives near $H=0$. Thus, this geometric series was used. Convergence could usually be achieved for values such as

$$\begin{aligned} R &= 10^{-3} \text{ cm} \\ H_1 &= 10^{-11} \text{ cm}^3 \\ \rho_H &= 1.5 \\ N_H &= 25 \end{aligned} \quad (C.3)$$

where N_H is the total number of spatial steps. For these parameter

values $r_{\max} \doteq 10^{-2}$ cm.

The zero-order problem of determining the radius profile $R(t)$ was solved in a straightforward manner, employing standard predictor-corrector methods. The evaluation of the elastic contribution to stress was simplified by the recursive property of an exponential memory function explained below. A Simpson's rule approximation of the stress integral results in (C.4)

$$\int_{-\infty}^{t + \Delta t} \exp\left(\frac{t' - (t + \Delta t)}{\lambda}\right) \dot{\gamma}_{rr}(t') dt'$$

$$\doteq \Delta t \frac{\dot{\gamma}_{rr}(t + \Delta t) + \exp\left(-\frac{\Delta t}{\lambda}\right) \dot{\gamma}_{rr}(t)}{2}$$

$$+ \exp\left(-\frac{\Delta t}{\lambda}\right) \int_{-\infty}^t \dot{\gamma}_{rr}(t') \exp\left(\frac{t' - t}{\lambda}\right) dt'$$

The R profiles so-generated were then available, along with \dot{R} and \ddot{R} values, as inputs to the $O(\epsilon)$ solution. Alternatively, the profile generated by the data fit explained in Appendix D was also available.

As in the numerical solution of many P.D.E. when time is among the independent variables, the procedure was to evaluate or specify all quantities, e.g. $X_{T_n}(I, J) \doteq T_n(H, \tau)$, for $I = 1, 2, \dots, N_n$, at some time step "J", then use those values to generate the corresponding numbers for the next time, "J + 1". The finite difference approximation to the T-equation employs a central difference in the time derivative and a mixed implicit-explicit weighting of the remainder of the equation, f_T , at J and J + 1. The function f_T results when the

vorticity equation is expressed in the form (C.5)

$$\frac{\partial T}{\partial \tau} = \frac{XT(I, J+1) - XT(I, J)}{\Delta \tau} \quad (C.5)$$

$$= f_T(H; R, \dot{R}, T, \frac{\partial T}{\partial H}, \frac{\partial^2 T}{\partial H^2}, I1, I2, I3)$$

The weighting was characterized by a relaxation parameter β_T , $0 \leq \beta_T \leq 1$, where $\beta_T = 1$ corresponds to a completely explicit algorithm. This relaxation parameter was among the numerical parameters varied in early calculations to insure, and then optimize, convergence. Spatial derivatives were approximated by a two-point central first derivative and three-point second derivative. These were chosen, despite the resulting requirement of small spatial steps, because the resulting matrix form of the XT-equation allows a non-iterative solution by Thomas' method.

The algorithm generated from these choices was applied twice. A "particular" solution, TZ(I) at (J + 1), results when XT(I, J) is retained. A second "homogeneous" solution, DTF(I) at (J + 1), is produced when the previous XT values are neglected. The linearity of the equation, allows the general solution at (J + 1) to be expressed as

$$TT(I, XRAT) = TZ(I) + XRAT * DTF(I) \quad (C.6)$$

where the factor XRAT must be determined by boundary conditions. The "homogeneous" and "particular" functions are also sufficient to determine the integral α_n and pressure term P_v within this same unknown

factor XRAT. The nomenclature employed is defined by

$$\left(-\frac{2n+1}{n+1}\right) a_n \dot{a}_n = UII + XRAT * DII$$

and p

$$P_v(H=0, \tau) = PRZ + XRAT * DPR$$

where UII and PRZ obtain for the particular solution TZ and DII and DPR from DTF.

The tangential stress equation (III.46) can be recast as

$$y_n(J+1) = f_{A_n}(a_n, TZ, DTF, UII, DII; XRAT; R, \dot{R}; \text{past values, physical parameters}) \quad (C.7)$$

where all the independent variables preceding the first semi-colon are for time (J + 1) and

$$y_n(J+1) = \dot{a}_n(J+1) \quad (C.8)$$

The normal force condition is somewhat more complicated, yielding

$$\dot{y}_n(J+1) = \ddot{a}_n(J+1) \quad (C.9)$$

$$= f_y(y_n, a_n, TZ, DTF,$$

$$PRZ, DPR; XRAT; R, \dot{R}, \ddot{R};$$

past values, physical parameters)

Various closed integration algorithms are available to give finite difference approximations to these equations. Here, four different algorithms were employed -- explicit; simple two-point mixed implicit explicit (β_A, β_y); mixed two and three-point ($\beta_A, \beta_y, \beta_{MA}, \beta_{MY}$) and a modification of a Hamming predictor-corrector employing four points. These were all tried, and choices made, once again to insure and optimize convergence. All algorithms lead to linear equations in $y_n(J+1)$, $a_n(J+1)$ and XRAT

$$y_n * WA(L) + a_n * WB(L) + XRAT * WC(L) = WD(L) \quad (C.10)$$

for $L = 1, 2$ and 3 , and where the coefficients, WA, WB, WC and WD, depend only on past values, physical parameters and $R, \dot{R}, \ddot{R}, TZ, DTF, UI1Z, DI1, PRZ$ and DPR , i.e. they are effectively constants with respect to y_n, a_n and XRAT. This is a well-posed, determinate system which is then solved for $a_n(J+1), y_n(J+1)$ and XRAT.

With these values, all quantities can be updated and the process repeated for succeeding times.

C.2 Sample Calculation

This method of solution is best illustrated by a sample calculation. For a purely Newtonian fluid of viscosity 0.10 cp, and the values:

$$\text{time step} = 2.50 \times 10^{-6} \text{ sec}$$

$$H_1 = 10^{-6} \text{ cm}^3$$

$$\rho_H = 1.50$$

$$N_H = 30$$

$$\text{initial radius, } R_0 = 1.98 \times 10^{-1} \text{ cm}$$

$$\text{initial amplitude, } a_0 = 1.27 \times 10^{-1} \text{ cm}$$

$$\text{initial nonspherical velocity, } \dot{a}_0 = -4.0 \times 10^2 \text{ cm/sec.}$$

The values at time step #10 were found to be

$$\text{time} = 2.50 \times 10^{-5} \text{ sec}$$

$$R = 2.42 \times 10^{-1} \text{ cm}$$

$$\dot{R} = -1.47 \times 10^3 \text{ cm/sec}$$

$$\ddot{R} = -2.21 \times 10^7 \text{ cm/sec}^2$$

$$XT(H=0) = -1.140 \times 10^3$$

I =	1	2	3	4	5
	-1.140	-1.141	-1.142	-1.144	-1.147
$\frac{XT(I)}{10^3}$	10	15	20	25	
	-1.201	-1.712	-2.428	-2.105	

$$\alpha = -8.702 \times 10^3$$

$$a = 9.553 \times 10^{-2}$$

$$\dot{a} = -1.863 \times 10^3$$

To calculate these values at time step #11, first these values are generated.

$$t = 2.75 \times 10^{-5} \text{ sec}$$

$$R = 2.46 \times 10^{-1} \text{ cm}$$

$$\dot{R} = 1.41 \times 10^3 \text{ cm/sec}$$

$$\ddot{R} = -2.19 \times 10^7 \text{ cm/sec}^2$$

and

$$TRZ = -5.315$$

$$DTRF = 0.996$$

$$UI1Z = -8.804 \times 10^3$$

$$DI1 = 6.422 \times 10^{-4}$$

$$UI2Z = -2.933 \times 10^6$$

$$DI2 = 2.804 \times 10^2$$

so that

	WA	WB	WC	WD
L = 1	3.39×10^{-2}	-6.42×10^1	-1.27×10^{-2}	-5.71×10^1
2	1.016×10^0	8.35×10^1	1.62×10^2	—
3	9.37×10^{-7}	-1.00×10^0	—	-9.26×10^{-2}

which can be used to determine

$$\dot{a} = -1.948 \times 10^3$$

$$a = 9.073 \times 10^{-2}$$

$$XRAT = -1.17 \times 10^3$$

$$\text{and } XT(H=0) = -1.170 \times 10^3$$

I =	1	2	3	4	5
	-1.171	-1.172	-1.173	-1.175	-1.177
$\frac{XT(I)}{10^3}$					
	10	15	20	25	
	-1.234	-1.732	-2.499	-2.162	

Variation of time step, spatial step and number of spatial steps was performed with convergence to these amplitude values.

APPENDIX D

Data Analysis

D.1 Shape and Size Fit

As stated in Section V, from each photograph the equivalent radius R , and some measure of the nonsphericity of the bubble is desired. The shape of these axisymmetric bubbles is assumed to be well fit by a series containing up to three nonspherical modes

$$r(\theta, \phi, t) = R(t) + a_2(t) Y_2^0(\theta, \phi) \tag{D.1}$$

$$+ a_3(t) Y_3^0(\theta, \phi) + a_4(t) Y_4^0(\theta, \phi)$$

where

$$Y_2^0(\theta, \phi) = P_2(\cos \theta) = \frac{1}{2} (3 \cos^2 \theta - 1)$$

$$Y_3^0(\theta, \phi) = P_3(\cos \theta)$$

$$= \frac{1}{2} (5 \cos^3 \theta - 3 \cos \theta)$$

$$Y_4^0(\theta, \phi) = P_4(\cos \theta)$$

$$= \frac{1}{8} (35 \cos^4 \theta - 30 \cos^2 \theta + 3)$$

In order to fit this function to the actual bubble image it is also necessary to determine the best location for the origin, and center-

line axis from which r and θ can be measured.

The basic strategy by which a fit can be made does not vary with a particular procedure. This strategy involves digitally encoding the location of points on the surface of the bubble in the chosen coordinate system, then performing a least square analysis to optimize the parameter values.

1) The simplest procedure employs just two measurements of bubble image, the major axis, which is assumed to be the largest horizontal dimension and the minor axis, the vertical dimension. These occur at $\theta = 0$ and π and $\theta = \frac{\pi}{2}$ and $\frac{3}{2}$, respectively when the contribution of the third and fourth modes is assumed to be negligible. If the lengths of the two axes are labelled l_0 and $l_{\pi/2}$, then values can be determined for $R(t)$ and $a_2(t)$ through

$$\begin{aligned} l_0 &= 2R + 2a_2 P_2(1) \\ &= 2R + a_2 \end{aligned} \tag{D.2}$$

$$\begin{aligned} l_{\pi/2} &= 2R + 2a_2 P_2(0) \\ &= R - a_2/2 \end{aligned}$$

which means that

$$\begin{aligned} R &= \frac{l_0 + 2 l_{\pi/2}}{6} \\ a_2 &= \frac{l_0}{2} - R \end{aligned} \tag{D.2'}$$

where $a_3 = a_4 = 0$ has been assumed.

This first procedure can be accomplished directly from the photograph or more accurately by magnifying the image. Magnification was accomplished by opaque projection. The succeeding three procedures require the additional accuracy afforded by the projection technique.

2) By guessing the centerpoint of the image and the axis of symmetry a polar coordinate digitization becomes possible. The (r, θ) coordinate pairs obtained can then be fit by a linear least squares fit to the function (D.1).

Unfortunately, the lack of fore-aft symmetry (right-left) in photos such as Figure 28(b) and 28(f) makes the *a priori* estimation of the origin difficult. The location of that point also needs to be fit.

Figure 28 also contains frames which display another feature of the images which makes analysis difficult. The bubble appears to have flattened ends in frames (e), (f), (g) and (h). The ends are not really flat, but are the result of the indentations illustrated in Figure 9(d) and 9(e) which do not appear in the photos since the interior of the bubbles is not visible. Thus, editing of the digitized data may be necessary for some frames. Unlike most fitting procedures wherein greater confidence can be placed in results for larger numbers of points, here judgement of "flat spots" is required.

The two methods expected to be most accurate include a fit to the origin. They are:

3) The centerline corresponding to the axis of symmetry is fixed *a priori*, then digitized data is fit to generate the best value of R , a_2 and the centerpoint on the axis.

4) Same as method 3), with the addition of a fit to a_3 and a_4 .

Both procedures, 3) and 4), employed the same data. Careful estimation of the centerline was made on enlarged images, which was made possible by the excellent angular (up-down) symmetry of the outlines. A first guess of the centerpoint was also made. From this center lines were drawn radially at 15° to 20° intervals. At the intersection of these line segments with the surface image, rectangular coordinates were measured. Rectangular coordinates were employed because this geometry allows simple transformations when the centerpoint is translated along the axis to improve the data fit. The best values of the desired amplitudes were then determined by an iterative nonlinear least squares algorithm which minimized the sum of the square residues. Trials were run with all the data, and also with editing for "flat spots".

Results for methods 1), 3) and 4) are shown in Table D1. Here results are shown, not only for different fit procedures, but also for different times, different photos at the same time, and for data with and without editing. Looking first at R values, the variation which occurs between methods 3) and 4) is seen to be minimal for different analyses of the same photo. The reproducibility between different photos is not as good, with a total variation of about 10% for the five photographs analyzed at 750 μ sec for methods 3) and 4). Method 1) does not agree quite as well with the other two methods employed; the R values from method 1) are consistently 5-10% smaller than the others, but do show proper trends.

The a_2 values show more variation than the R values due to fitting procedure and to photograph to photograph reproducibility. There is no

TABLE D1. Comparison of Fitting Methods

TIME (μsec)	PHOTO	METHOD	# POINTS	R (10^{-3}cm)	a_2 (10^{-3}cm)	a_3 (10^{-3}cm)	a_4 (10^{-3}cm)		
650	a	1	2	3.00	0.87				
		3	18	3.16	1.08				
		4		3.17	0.98	0.63	-0.40		
		3	16	3.17	1.24				
		4		3.16	0.88	0.83	-0.26		
		4							
	700	a	1	2	3.25	1.10			
			3	18	3.36	1.21			
			4		3.36	0.95	-0.79	0.30	
			4						
			b	1	2	3.20	1.20		
				3	18	3.33	1.19		
4				3.32	1.07	0.04	0.29		
c		1	2	3.30	0.76				
		3	18	3.51	0.74				
		4		3.51	0.65	0.17	0.17		
750		a	1	2	3.36	0.33			
			3	18	3.58	0.38			
			4		3.58	0.36	-0.19	0.01	
			3	17	3.58	0.38			
			4		3.58	0.37	-0.22	0.04	
			3	18'	3.58	0.42			
			4		3.58	0.38	-0.22	0.06	
			b	1	2	3.36	0.86		
	3			18	3.55	0.99			
	4				3.54	0.86	0.52	0.20	
	c		1	2	3.47	0.33			
			3	18	3.67	0.54			
		4		3.68	0.52	-0.13	-0.14		
	d	1	2	3.47	0.76				
		3	18	3.70	0.84				
		4		3.70	0.85	-0.30	-0.07		
	e	1	2	3.15	0.54				
		3	18	3.42	0.63				
		4		3.41	0.59	-0.21	0.06		
	800	a	1	2	3.47	0.43			
			3	18	3.70	0.37			
			4		3.70	0.23	-0.28	0.23	
			4						
			b	1	2	3.53	0.87		
3				18	3.71	1.12			
4				3.71	0.95	-0.53	0.23		

pattern apparent in the differences between methods; compare 650 (a) where method 1) and method 4) agree well, to 750 (c) where 3) and 4) closely approach one another and 800 (a) where 1) and 3) almost coincide.

Thus, no criteria for the best fitting procedure emerges from the R and a_2 values. The additional amplitudes a_3 and a_4 are of little assistance, varying from -0.30 to $+0.52$ at $750 \mu\text{sec}$. As a result the fitting procedure was chosen on a strictly practical basis. Method 1) was the simplest to employ and was used in the remaining data analysis.

D.2 Radius Profile

In order to generate $\dot{R}(t)$ and $\ddot{R}(t)$ values, as well as interpolate the discrete $R(t)$ data measured by the procedures of the preceding section a smooth fit was made to all the experimental data simultaneously. The shape suggested by the radius data in Figures 22 and 24-27 is that of a sine wave, so a Fourier series was fit to the numbers. Parameters which were optimized through a nonlinear least squares analysis were:

- t_0 - the initial time at which $R(t) = 0$
 - t_p - the period of the primary wave
 - C_j - the amplitudes of the various waves
- for $J = 1, 2, \dots, 5.$

The functional form of the wave was

$$R_{fit}(t) = \sum_{j=1}^5 C_j \sin \left(\frac{t-t_0}{t_p} \pi K_j \right) \quad (D.3)$$

where K_j are integers. The K_j were also varied, and the best fit usually occurred for

$$\begin{aligned} K_1 &= 1 \\ K_2 &= 2 \\ K_3 &= 3 \\ K_4 &= 5 \\ K_5 &= 7 \end{aligned} \quad (D.4)$$

and the contribution of these last two waves was small. Here, best fit means those values for which the sum of the square residues, ρ^2 , is at a minimum

$$\rho^2 = \sum_{l=1}^n [R(t_l) - R_{fit}(t_l)]^2 \quad (D.5)$$

where n is the number of data points and t_l is the time at which these data exist.

APPENDIX E: Additional Data for Photo Sequences

The camera, tank and laser are oriented so that the laser enters the fluid from the right side in each photograph. The beam is focussed by the lens to a "spot", manifest as the bright streak in each photo. This streak is useful as a reference point since it appears at the center of the original bubble.

Figure 21.

Medium lens + 1.5 cm from center
Laser: 80.0%, no filter

Figure 22.

Medium lens:
Laser: 80.0%, medium filter

Figure 23.

Medium lens
Center to solid wall $\sim 0.7 \pm 0.05$ cm
Laser: 97.0%, medium filter

Figure 30.

Distilled water
Lens separation: 8 cm
Laser: 97.0%, no filter
Center to solid wall $\sim 0.7 \pm 0.05$ cm

Figure 31.

Distilled water
Lens separation: 5 cm
Laser: 97.0%, no filter
Center to solid wall $\sim 0.5 \pm 0.1$ cm

FILME

7-8